



The University of
Nottingham

UNITED KINGDOM • CHINA • MALAYSIA

Structural Optimisation of Discontinuous Carbon Fibre Composites

Connie Cheng Qian

BEng. (Hons.)

Thesis submitted to the University of Nottingham
for the degree of Doctor of Philosophy

November 2013

Abstract

There has been a growing interest in using discontinuous carbon fibre composites for semi-structural applications within the automotive industry. The main advantages of discontinuous fibres are low material costs, low wastage and low touch labour compared with processes using carbon fibre textiles. Directed Carbon Fibre Preforming (DCFP) is an automated process for producing complex 3D preforms for liquid moulding. DCFP offers the potential for producing highly optimised structures, with local control over tow size, fibre length and volume fraction within the component. The execution of this is challenging however, as confidence in the current library of material properties is low and existing structural optimisation packages only consider a very limited number of design variables, which are restricted to more conventional composite materials.

This thesis aims to establish a structural design tool to exploit the design freedom offered by the DCFP process. A large number of parameters associated with the fibre architecture can be controlled to meet a range of design criteria such as performance, weight and cost. The optimisation tool is capable of generating locally varied fibre areal mass and thickness maps that are suitable for manufacture by the robot controlled process.

The developed model adopts a multi-scaled finite element approach. Meso-scale simulations are performed to establish size effects in discontinuous fibre composites, to quantify the level of stochastic variability and to determine the representative volume element for a given fibre architecture. A DCFP material database is generated to facilitate macro-scale modelling at the component level. The macro-scale model iteratively redistributes material in order to minimise the total strain energy of the model under prescribed loading conditions. The optimised model is segmented into areas of uniform areal mass, where the zone geometries are tailored to achieve representative material

properties according to the meso-scale results, whilst ensuring the design is fit for manufacture.

An automotive spare wheel well has been chosen as a demonstrator component, enabling two DCFP architectures to be compared against a continuous glass/carbon fibre NCF design. The first case offers a high performance (high specific stiffness) solution and the second offers a low cost option using high filament count tows. Following optimisation, results suggest that a 3K 25mm fibre length DCFP option can achieve a specific stiffness 52% higher than the glass/carbon baseline design, but for 1.33 times higher material cost. Alternatively, the specific stiffness of a 24K 50mm fibre length DCFP is marginally lower than the first option, but still out-performs the baseline for just 67% of the material cost. The structural optimisation method demonstrates that discontinuous fibre composites can compete against continuous fibre counterparts for semi-structural applications.

Acknowledgement

The author wishes to acknowledge her academic supervisors Dr Lee Harper, Dr Thomas Turner and Prof Nicholas Warrior for their invaluable support.

Many thanks to Roger Smith and Geoffrey Tomlinson for their technical assistance in the experimental work.

The financial support from the University Research Scholarship (URS) is also acknowledged.

Finally and most importantly, I am eternally indebted to my parents for their love, support and encouragement.

Contents

Abstract	2
Acknowledgement	4
Contents	5
Chapter 1. Introduction	9
1.1 Discontinuous fibre composites in high performance applications	9
1.2 Directed fibre preforming process	12
1.3 Problems encountered testing the mechanical performance of discontinuous fibre composites	15
1.4 Structural design of discontinuous fibre composites	17
1.4.1 Structural design of composites: the state of art	17
1.4.2 DCFP design framework	19
1.5 Scope of thesis	20
Chapter 2. Representative volume elements for predicting elastic properties	23
2.1 Background	23
2.1.1 Random discontinuous fibre architecture modelling challenges	23
2.1.2 Size effects in meso-scale RVEs	27
2.2 Methodology	31
2.2.1 Generation of meso-scale RVEs	31
2.2.2 Finite element modelling	32
2.2.3 Boundary conditions	34
2.2.4 Determining the RVE Size: Stopping criterion	37
2.2.5 Measure of departure from isotropy	38
2.2.6 Measure of homogeneity	40

2.3	Results	41
2.3.1	Decay length of boundary conditions	41
2.3.2	Convergence of effective properties	43
2.3.3	Convergence of variation	48
2.4	Conclusions	52
Chapter 3.	Damage tolerance of discontinuous fibre composites	55
3.1	Background	55
3.1.1	Notch sensitivity of discontinuous materials	55
3.1.2	Stress Fracture Criteria	58
3.2	Results	60
3.2.1	Size effect of un-notched specimens	61
3.2.2	Constant width study for notched specimens	64
3.2.3	Constant hole-to-width ratio study for notched specimens	69
3.2.4	Fracture criteria	72
3.3	Conclusions	75
Chapter 4.	Development of a stiffness optimisation algorithm for discontinuous fibre composite components	77
4.1	Introduction	77
4.2	Stiffness optimality criterion	80
4.2.1	Problem formulation	80
4.2.2	Stiffness optimality criterion and the Lagrangian multiplier approach	82
4.2.3	Model validation results	86
4.2.4	Optimisation results	88
4.3	Determining the fibre architecture	90
4.3.1	Material assignment	90
4.3.2	Segmentation with multi-level thresholding	93

4.3.3	Length scale and size control	95
4.3.4	Results	98
4.4	Conclusions	104
Chapter 5.	Case Study: Stiffness optimisation of a structural automotive component	106
5.1	Introduction	106
5.2	Decision Making Criterion	107
5.3	Candidate materials	108
5.4	Results	113
5.4.1	Influence of fibre architecture parameters	113
5.4.2	Case 1: High stiffness and lightweight	117
5.4.3	Case 2: low cost	120
5.4.4	Discussion of Models	123
5.5	Conclusions	125
Chapter 6.	Thesis Conclusions	126
6.1	DCFP material properties	126
6.1.1	Representative volume elements for elastic properties prediction	126
6.1.2	Damage tolerance	127
6.2	Structural optimisation	128
6.2.1	Stiffness optimisation methodology	128
6.2.2	Structural optimisation case study	128
6.2.3	Structural optimisation in DCFP design	129
6.3	Future work	130
Appendices		132
Appendix A.	List of publications	132
Appendix B.	Additional studies for meso-scale RVE modelling	134

Chapter 1. Introduction

This chapter outlines the scope of the thesis by introducing the concept of using discontinuous fibre composites for structural applications within the automotive industry. The suitability of using an automated fibre deposition method is discussed to produce repeatable components, including the current barriers preventing wider commercial acceptance. The challenges associated with using heterogeneous materials for structural design are presented, leading to the justification of developing an optimisation algorithm for determining the fibre architecture for discontinuous fibre composites.

1.1 Discontinuous fibre composites in high performance applications

Both aerospace and automotive industries have the requirements of using lightweight materials to reduce fuel usage to meet current environmental legislations. While the aerospace sectors are willing to spend \sim £1200-£2500 to save 1kg of body weight, the automotive sectors are willing to spend only £1.50 per kg below the centre of gravity, and £5 per kg above [1]. Textile based continuous fibre composites are widely used in the aerospace industry as lightweight replacements for metallic materials. However, applications of continuous fibre composites in the automotive industry are exclusively reserved for sports cars and luxury vehicles of very small production volumes (<1000ppa). This is because of high material costs, labour intensive processes and long cycle times (several hours) compared with conventional metallic components. Discontinuous fibre composites provide a good compromise in terms of cycle time and component cost, compared with metallic and continuous fibre composites. The production of discontinuous fibre composites can be more readily automated, providing a reduction in touch labour, and materials require less intermediate processing (such as weaving or pre-impregnating), so material costs are much lower than using broad goods.

Consequently, discontinuous fibre composites are considered to be more suitable for the automotive industry [2].

Applications of discontinuous fibre composites within the automotive industry are typically in the form of short glass fibres in injection moulded materials for non-structural components, glass mat thermoplastics (GMT) or sheet moulding compounds (SMC) for semi-structural components [3]. However, in 2008, it was reported that ~8% of the UK's carbon fibre consumption was in the form of discontinuous fibre composites, where 50% of this was used in compound form within the automotive industry [4]. This trend has continued globally, with several niche vehicle manufacturers committing to using discontinuous carbon fibre composites for automotive applications. The 2003 Dodge Viper was mass produced (approx. 2000ppa) using compression moulded carbon fibre SMC, where a total of nine components were made (eight kilograms of carbon fibre used in total) of high modulus material [5, 6]. Menzolit produced carbon fibre SMC body parts for the 2004 Mercedes-Benz McLaren SLR, where 60% weight saving was achieved compare with lightweight aluminium alloy [7]. This was considered to be a successful application of carbon SMC and the material was further utilised when Mercedes launched a special edition of the SLR (Silver Arrow 722), which was also equipped with a rear scuttle panel made of Menzolit's material, contributing to a further weight reduction and improved performance over the standard model [8]. Carbon SMC was also successfully used for the bonnet of General Motor's Chevrolet Corvette Z06 Commemorative Edition, to replace glass fibre SMC [9]. The carbon fibre bonnet was almost 5kg lighter than the glass SMC version, with a total weight of just over 9kg. Lamborghini and Callaway Golf Company have recently partnered and developed 'forged composite' with Quantum composites, a rebranding of their Lytex 4149 material. The process is capable of making very complicated and accurate shapes, and has been utilised on the Lamborghini's Sesto Elemento concept car on both the monocoque chassis and the suspension arms, as well as Callaway Gold's Diablo Octane drivers [10].

Although applications are mostly found within the automotive industry, the aerospace industry has recently adopted discontinuous fibre composites for a structural application, using randomly chopped carbon fibre prepregs to produce window surrounds for a large passenger aircraft [11]. These advanced SMCs (ASMC) offer tensile modulus values in the range of 40-60GPa [12] and tensile strengths of up to 300MPa [13] (at 50-55% volume fraction), while the cycle times are short (5-20 minutes). However, ASMCs still require significant amounts of touch labour to place the near-net shape charge into the tool, because high fibre content and high viscosity matrices limit the amount of in-mould flow.

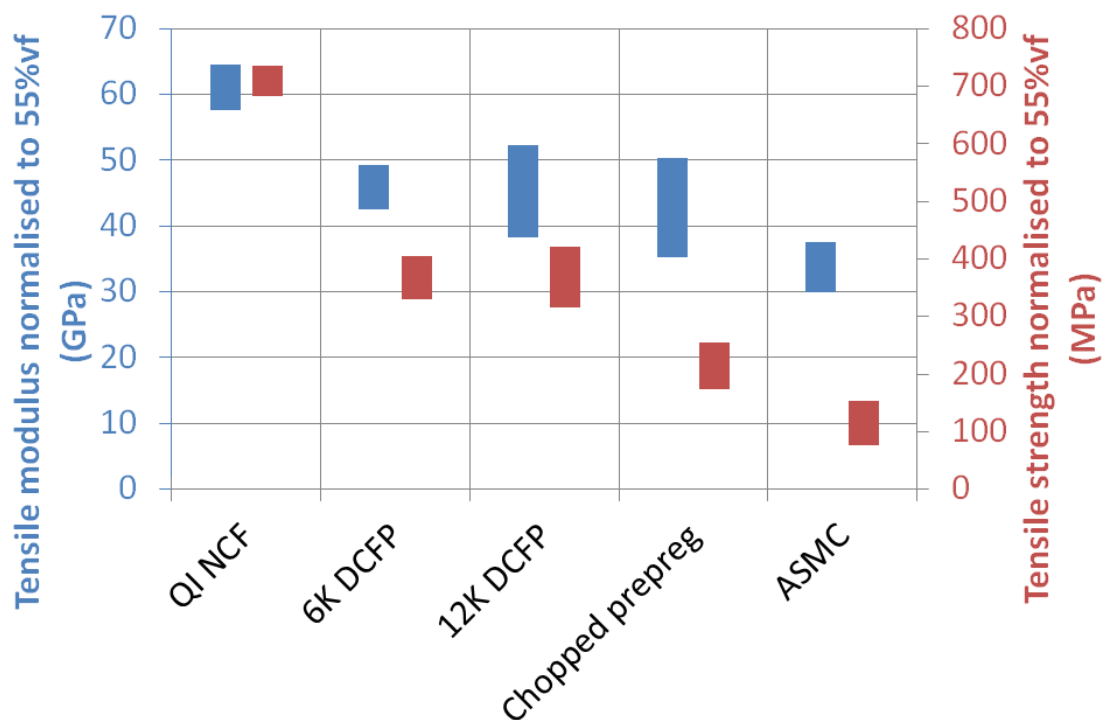


Figure 1-1: Normalised tensile modulus values wrt fibre volume fraction. Comparisons include quasi-isotropic non-crimp fabric (QI NCF), direct carbon fibre preforming (DCFP) consisting of 6K fibre and 12K fibre, chopped and randomly distributed prepreg and advanced sheet moulding compound (ASMC). QI NCF is a continuous fibre composite and the rest are discontinuous. The DCFPs contain a constant fibre length of 25mm. [2]

Figure 1-1 compares the tensile modulus and strength data for some common quasi-isotropic composites manufactured from carbon/epoxy.

Although there is a notable reduction in the strength between the continuous fibre NCF and the discontinuous fibre systems, the moduli (80% retention) are generally comparable. In [12], the stiffness of DCFP (Toray T700 12K 50C) was reported to be the same as QI NCF (quasi-isotropic non-crimp fabric) of the same fibre volume fraction. Therefore, there is a strong argument that discontinuous fibre composites are suitable for stiffness-driven structural applications, for example the automotive body in white. A recent study in [14] also suggests good impact and energy absorption properties for discontinuous fibre composites. Specific energy absorption values of 80kJ/kg for static loads and 50kJ/kg for dynamic loads can be achieved with optimum fibre architectures, compared with ~ 18 kJ/kg (static) 20kJ/kg (dynamic) for annealed steel [15], and 22kJ/kg for aluminium (both static and dynamic) [16]. Comparisons were made in [2] of the in-plane tensile, compressive and shear stiffnesses and strengths, flexural stiffness and dent resistance between continuous and discontinuous carbon fibre derivatives. Results proved that apart from the tensile strength, the other properties for discontinuous fibre composites were comparable to those of continuous fibre composites.

1.2 Directed fibre preforming process

Directed Fibre Preforming (DFP) is an automated process for producing complex 3D discontinuous fibre preforms for liquid moulding [17]. Unlike SMC techniques, the DFP process uses a robotically controlled fibre deposition route where fibre length, tow size and volume fraction can all be explicitly controlled to produce variable stiffness components. The DFP process enables near net-shape manufacturing of the preform, of which the wastage is typically less than 3% by weight [18]. Since fibre bundles are chopped in their roving form, the cost of the raw materials is less than 50% of the cost of chopped strand mats of the same volume fraction [18]. Due to the relatively high investment of the manufacturing facility, the process is particularly attractive for medium volume (1000-

20000ppa) production, such that the overall cost is very competitive compared with using conventional metallic materials [12]. DFP processes have been extensively developed for manufacturing automotive components [2, 12, 19].

The Programmable Powered Preforming Process (P4) [20] is an established process, where glass fibre and binder are applied to perforated preform tools via robot routines. Once the desired fibre thickness is achieved, a separate consolidation step is required to compact the preform whilst hot air is used to melt the binder. Cold air is subsequently used to freeze the binder before the preform is transferred to a closed mould for resin injection. The P4-SRIM process has been commercialised for making a glass fibre truck bed for the Chevrolet Silverado (Figure 1-2). A 40% reduction in raw material cost was reported compare with SMC, and a 25% mass reduction was achieved compared with a steel counterpart of equivalent flexural stiffness. Furthermore, the overall cycle time was just 4 minutes per part [21], which equates to a maximum volume of 100,000ppa. P4 research has continued, funded by the U.S. Air Force, to investigate its feasibility for aerospace parts with carbon fibre to replace glass fibre [22].



Figure 1-2 Composite truck bed installed in Chevrolet Silverado.

The Ford Programmable Preforming Process (F3P) was Ford's refinement of the original P4 process. The missing "P" denoted the powdered binder which was replaced with string binder [22], in order to overcome problems such as clogging of holes in the preform screens. The F3P-RTM process was utilised for manufacturing the upper cargo deck and the RH/LH bodysides on the Aston Martin Vanquish, and on Aston Martin DB9 for several components such as RH/LH sill appliques, door opening rings and decklid surrounds on both coupés & convertibles.

The substitution of carbon fibre was introduced [12, 23, 24] to achieve further weight reduction over metal or glass fibre counter parts, whilst offering significant cost savings over conventional carbon textile options. The Directed Carbon Fibre Preforming (DCFP) process was developed at the University of Nottingham using a laboratory-scale machine [2, 12, 18, 25]. Carbon fibre is challenging from a manufacturing perspective [2]. The lower density fibre causes difficulty in fibre placement control, and the finished preforms are more difficult to handle compared with glass preforms, due to lower flexural rigidity of the carbon preforms caused by the smaller filament diameter (8 μ m for carbon filament vs. 14 μ m for glass). These problems are the potential cause of non-uniform fibre distribution of DCFP preforms, and consequently reduced mechanical performance of the moulded components.

The key to improving the mechanical performance of DCFP components is to reduce the variations of fibre coverage and make the preforms more uniform [26]. Both inter- and intra- preform variations are considered during process optimisation, where the former aims to minimise the variations of material properties within a part, and the latter is to ensure consistent performance for all parts manufactured by the same robot program [2, 26]. Whilst previous studies have successfully improved the fibre coverage by looking at the effects of constituent materials and machine parameters, numerical simulation tools have also been developed to provide an effective way of rapidly predicting the areal mass variation for different fibre deposition strategies [2, 25]. Early attempts at DCFP process simulation offered solutions for simple planar

structures, but recent developments [25] have considered factors such as the robot trajectory and gravitational effects, which offers a more robust simulation tool for 3D geometries. DCFP type process simulations have been developed by other institutions. In [27], a micromechanics analysis was performed to predict the properties of the consolidated components using the Mori-Tanaka method and texture tensors. The approach successively predicted the preform variability in cases of short fibre lengths and at locations far from preform boundaries. Effects of deposition path direction were studied in [28], and the results were implemented to develop a chopper gun trajectory generation algorithm to support the work at the NCC in Dayton Ohio.

1.3 Problems encountered testing the mechanical performance of discontinuous fibre composites

Correctly specified material parameters is the key to reliable design and good part consistency. Figure 1-3 shows the well-known multi-scale approach used in aerospace design, where material properties are only evaluated at the beginning of the design cycle and then adopted in all subsequent calculations and simulations. The stiffnesses of conventional textile composites are assumed to be independent of specimen size [29, 30], since these materials contain a repeating cell which exhibits the same behaviour. The global elastic constants represent volume averaged properties that can be measured from the domain of the tested material. The strength of larger structures on the other hand, might differ from that of a test coupon, since the possibility of having large flaws increases with the material volume. The strength variations caused by the size effects are commonly predicted with analytical models such as Weibull strength theory [29-32]. Discontinuous fibre composites however, are known to experience size effects in both stiffness and strength [33, 34]. Unlike textile composites, within random discontinuous fibre composites each small segment of the material does not behave in the same manner. The stiffness of the material is a volume averaged property and a representative value can only be achieved when the size of the tested

domain is large enough to ensure there is homogeneity at the macro-scale. Strength related size effects are dominated by the weakest link within the tested domain, and in order to obtain strength of the weakest link, it is necessary that the material tested produces a representative stress-strain response. Therefore, strength size effects can only be studied with larger samples when the stiffness size effects have been eliminated, such that the strength is only affected by the possibility of defects.

Experimental studies of DCFP size effects were performed in [2], where specimens of variable widths were tested up to 50mm. Although it has been demonstrated that the mean tensile stiffness and strength vary with specimen width, it cannot be determined whether 50mm is a representative coupon size without comparing with results from larger specimens. Statistical analysis of the experimental DCFP data in [2] suggests that a large number of specimens of the same fibre architecture are required to achieve 95% confidence of the tensile properties, which is impractical and costly. The suitability of using properties data with high coefficient of variation in structural design is questionable. A larger safety factor must be used to prevent over-estimation of structural performance, but this could equally lead to inefficient, heavy components. There is a distinct lack of understanding of the size effects in materials such as DCFP, and new methods are required to establish and overcome the limitations associated with conventional characterisation routes.

Due to the limitations in various methods of evaluating material properties for discontinuous material, size effects are not yet well understood. Their effect on other structural properties such as notch sensitivity [35-37], flexural behaviour [38, 39] and fatigue behaviour [40, 41] are studied even less in the literature. This lack of knowledge results in very little confidence when contemplating using these materials in structural design.

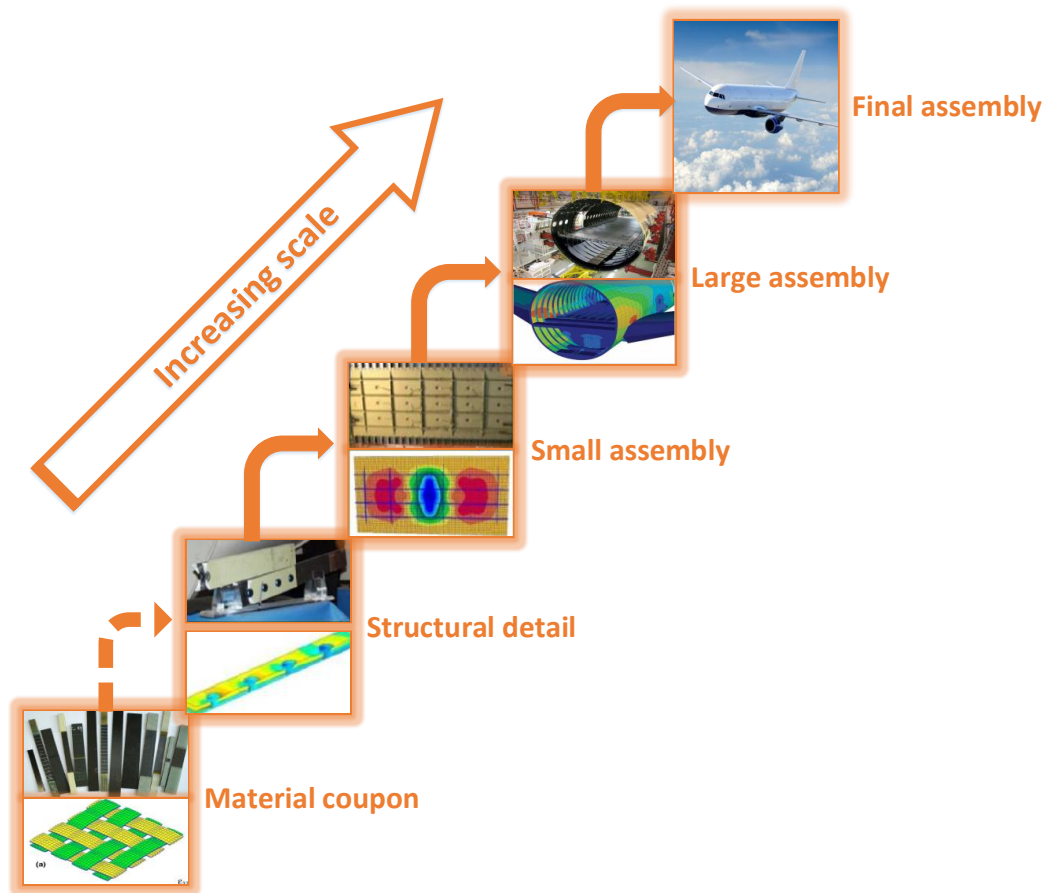


Figure 1-3 Multi-scale approach of structural design of conventional composites[42-44].

1.4 Structural design of discontinuous fibre composites

1.4.1 Structural design of composites: the state of art

Stiffness, strength and impact resistance are the most widely considered criteria in the context of structural design. This thesis focuses on stiffness driven design of discontinuous fibre composites for shell structures. Stiffness is a measure of the deflection of the structure under prescribed in-service load cases, or the dynamic response under dynamic loads. Structural stiffness is influenced by both the material properties and the component's geometry. In many industrial applications, the

design is required to maximise the structural stiffness with the most efficient use of materials. In general, stiffness needs to be improved with minimum impact on manufacturing cost or raw materials, and in addition, weight reduction is also of interest in many cases (automotive and aerospace industries for example).

Conventional designs commonly adopt heuristic approaches in order to meet the design requirements. The flowchart in Figure 1-4 illustrates such approaches, where the design undergoes a design-redesign cycle until the design requirements are satisfied. The released design is the best one selected from all historical designs. With this approach, the final design is only a 'best guess' of which the quality highly relies on the experience of the designer. Nevertheless, there is an increasing trend of using optimisation tools to replace these historical data driven designs.

Structural optimisation is the method of enhancing the structural performance by optimising the material layout within a design domain. While optimisation methods for metals have been well established in the past [38, 40, 45-48] there is a lack of suitable design strategies for modern composite materials. Consequently, composite components are often designed following metal design routines. A typical mistake made in 'black sheet metal' is to assume that part thickness must be uniform. The thickness does not need to be uniform; single sided tooling/ double sided tooling with non-uniform cavity height can be considered at least in lower volumes [49]. There are other typical signs of black metal design such as using ribs wherever extra stiffness is needed. Ribs are not the only option for adding stiffness, and are not necessarily the best option for composites either. The flexibility in composites forming techniques allows more complicated geometries to be made within one part. Additionally with processes such as DCFP, it is also easy to produce locally varied fibre architectures. These are considered to be more efficient approaches for creating locally varied structural stiffness using composites, rather than using ribs as in conventional metal design [49].

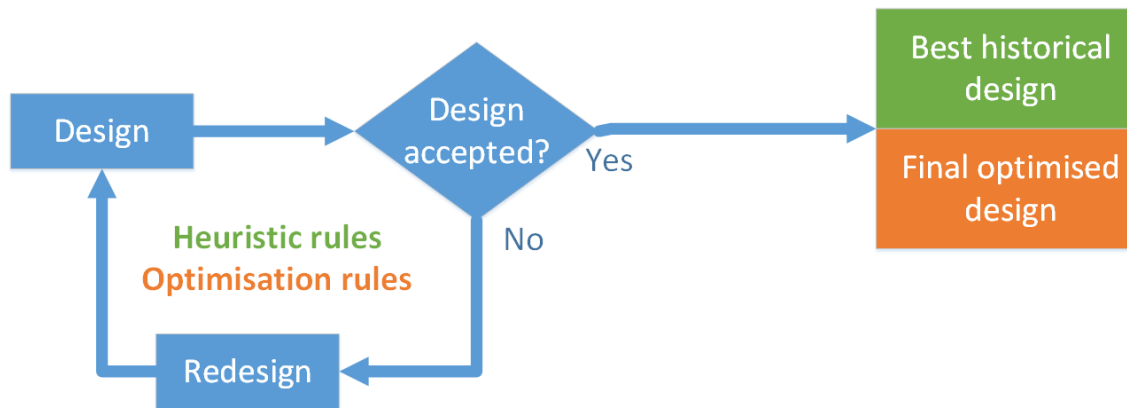


Figure 1-4 Flow charts for comparison between (a) conventional heuristic rules based design (b) Structural optimisation routine.

1.4.2 DCFP design framework

Previous research[2, 12, 25, 50, 51] at Nottingham aimed to establish a complete design package for optimising DCFP components in semi-structural applications. The structure of the DCFP design framework is presented in Figure 1-5. The package contains two main parts: The first focuses on the mechanical performance from a material properties perspective[2, 51] and the other focuses on process simulation and optimisation[2, 25, 50]. A hierarchical multi-scaled approach starts with micro-scale FEA modelling at the filament level, which determines the effective properties of unit cells consisting of UD filaments embedded in matrix[51]. This input data is used in a meso-scale FE model to generate a material database from virtual coupon testing. The material database then facilitates macro-scale component level modelling for structural optimisation. Structural optimisation aims to deliver the required fibre architecture for the optimum design, which forms the input for the subsequent process simulation step. This leads to the simulation of a virtual robot spray program, which enables the final fibre architecture to be predicted ready for validation.

1.5 Scope of thesis

This work focuses on the structural design of DCFP components intended for stiffness driven applications, where component weight, material cost and manufacturing complexity can all be traded to meet multiple design requirements. Whilst previous work [2, 51] has successfully predicted the properties of fibre tows at the micro scale, there is very limited knowledge of producing models for meso-scale (coupon level) predictions. Current work seeks to gain further understanding of the mechanical behaviour of DCFP materials, in order to enable the fibre architecture of the optimum design to be determined.

Chapter 2 and Chapter 3 of this thesis focus on further understanding the material properties of DCFP. Chapter 2 studies the elastic properties of DCFP and their size effects. Due to the restrictions in specimen size for experimental testing, and the poor accuracy of analytical stiffness predictions, a meso-scale FEA model is proposed. Tensile modulus, shear modulus and Poisson's ratio are evaluated and the critical size of the representative volume elements (RVEs) is also studied by tracking the convergence of the effective elastic properties. Understanding the critical RVE size can help to determine the size of experimental coupons for achieving high reliability levels. Chapter 3 studies the damage tolerance of DCFP in term of notch sensitivity using digital image correlation (DIC). Quasi-isotropic non-crimp fabric (NCF) has been used as a benchmark material. Chapter 3 experimentally investigates the specimen width effects (size effects) on the tensile modulus and strength of un-notched DCFP and NCF coupons. This Chapter goes on to investigate the effects of notch size for constant specimen widths and specimen width effects for constant notch size to width ratios. Semi-empirical failure criteria models are also demonstrated and compared for notched strength predictions.

A Stiffness optimisation method is presented in Chapter 4 to intelligently optimise the fibre architecture of DCFP components, using a strain energy density algorithm to maximise the global stiffness according to specific design criteria. Cost, mass and cycle time can all be varied against component performance through local selection of material

parameters. The optimisation is performed in two main stages. The first stage aims to determine optimum local thickness and material stiffness distributions across the component. The second stage aims to develop a fibre architecture map for the optimised component, facilitating downstream modelling of the manufacturing process. A rectangular plate with three circular holes is used to demonstrate the two stages of the structural optimisation model. A case study is presented in Chapter 5, which applies the optimisation algorithm to an OEM automotive component. The model is used to ascertain the real-world cost and weight savings using an optimised DCFP structure over non-crimp fabric and steel benchmarks.

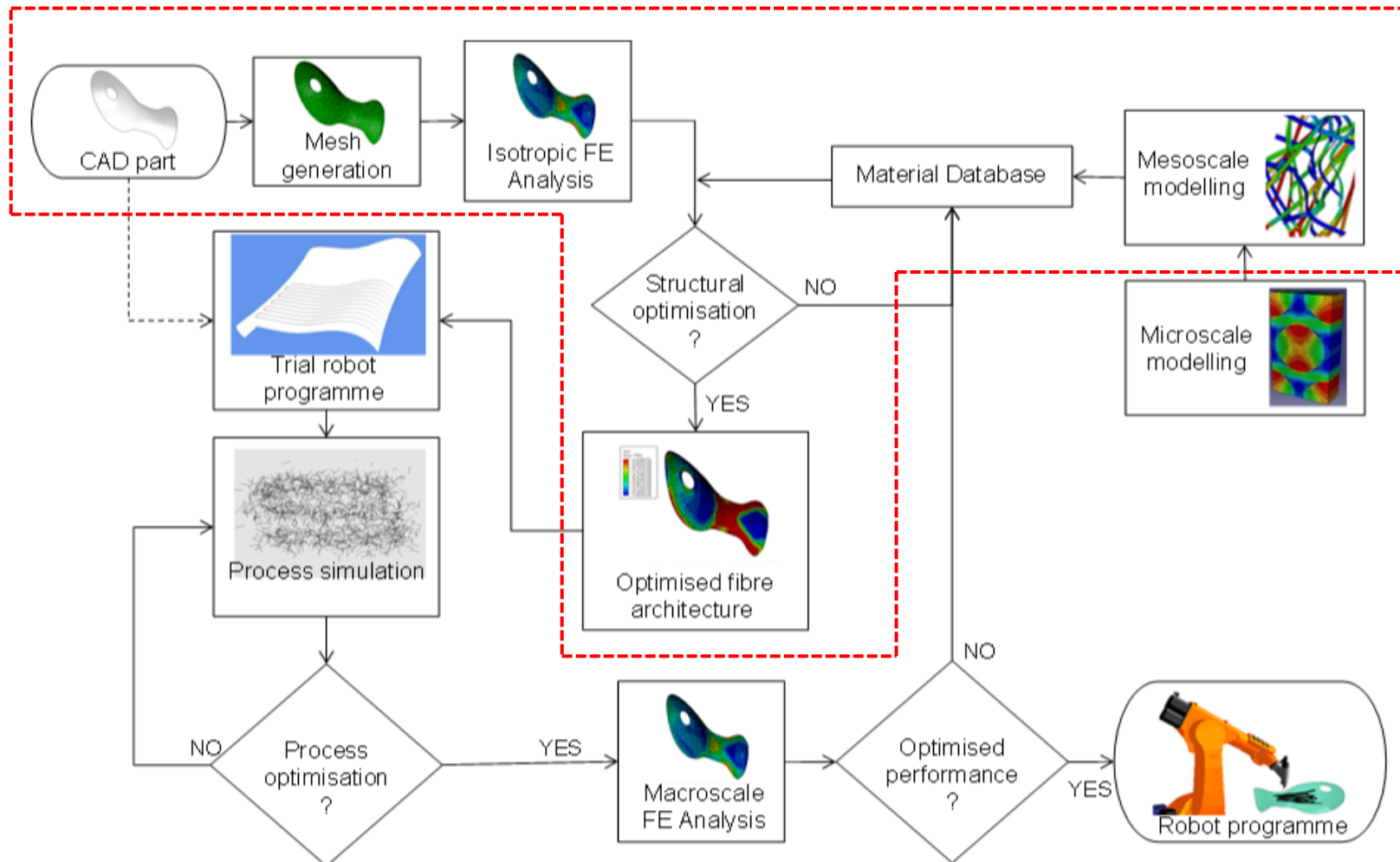


Figure 1-5 DCFP design framework. Work involved in this thesis is bounded by the red box.

Chapter 2. Representative volume elements for predicting elastic properties

The random nature of the reinforcement architecture within discontinuous fibre composites means that a conventional periodic unit cell (e.g. [52, 53]) is unsuitable for FEA modelling. The non-repeating heterogeneous architecture of a discontinuous system makes it difficult to derive appropriate boundary conditions and to choose the size of RVE. A finite element based embedded cell approach is presented in this chapter to provide a good approximation for the elastic constants of a random fibre material. The model is used to determine if a critical (or minimum) RVE size exists, in order to quantify the size and scale effects identified in Chapter 1.

2.1 Background

2.1.1 Random discontinuous fibre architecture modelling challenges

FEA is widely used to model the response of randomly distributed fibre composites. FEA methods potentially reduce the expense of experimental testing by performing 'virtual coupon tests'. Once programmed, the process of creating the destination fibre architecture is also faster compare with manufacture of plaque. The use of micro- and meso-scale models allows the effect of non-uniform fibre distribution and the fibre-matrix stress transfer mechanism to be defined, thus provides much more realistic stress-strain response over the existing analytical models. FEA approach is well documented for studying randomly distributed filaments [54, 55] or spherical inclusions [49] at the micro-scale, but is not so common for modelling 3D randomly packed bundles at the meso-scale. These architectures are far more challenging to model with many more independent variables to consider, particularly for high fibre volume fractions and large aspect ratio fibres [56].

Existing analytical models are reviewed in [57] for predicting the elastic modulus of discontinuous carbon fibre composites. Common methods are typically based on either a mean field inclusion approach [58, 59] or a micro-mechanical [60, 61] approach, where the properties of a discontinuous unidirectional fibre sub-unit are determined (assuming an equivalent fibre aspect ratio and fibre volume fraction to the random material). Orientation averaging is then performed to create an analogous composite with random fibre orientations, either using tensor averaging [62] or classical laminate theory [63, 64]. These methods effectively homogenise the fibre architecture as an infinite extension, discounting effects such as fibre clustering or local bias in the orientation distribution, and are commonly known as asymptotic estimates. Ionita and Weitsman [65] developed the application of classical laminate theory further into the 'laminated random strand' model, which used a 'moving window approach' to statistically assess large volumes of heterogeneous material. No consideration was given to basic failure mechanisms at the micro-scale, such as matrix cracking, fibre/matrix debonding, and consequently strength predictions were poor when compared to experimental data.

FEA methods developed for particle reinforced composites [66, 67] have been modified to model slender fibre inclusions [68], but generating realistic fibre architectures still remains a challenge. High volume fractions are difficult to achieve for fibres with large aspect ratios and distorted finite element meshes can occur at local fibre contact points.

Methods for producing numerical RVEs for random fibre architectures can be categorised into two main groups [56]; random sequential adsorption (RSA) and Monte Carlo (MC) procedures. RSA and MC methods are quite similar in their approach and consequently suffer from the same problems. Random numbers are generated within allowable bounds to represent the orientation and position of the centre of mass of each fibre [56, 68]. For RSA, fibres are added to the RVE consecutively and checks are performed to avoid intersecting fibres. Violating fibres are removed and then reapplied on the next run of the algorithm until the target fibre

volume fraction is reached. In contrast, the MC method deposits all fibres initially inside the RVE and then 'shakes' and/or 'squashes' the volume to rearrange the fibres without violating the contact algorithm [69, 70].

The major problem with both the RSA and MC approaches is that 'jamming' occurs at higher fibre volume fractions, as fibre intersections become unavoidable within the remaining free volume. Fibres are often modelled as slender, non-deformable rods with no out of plane curvature [71, 72], which cannot be packed as efficiently as the fibre bundles in real coupons. Ceiling volume fractions of $\sim 20\text{-}25\%$ have been reported [69, 73] depending on the aspect ratio of the fibre. Kari et al [73] used a range of fibre aspect ratios within the same RVE to increase the volume fraction up to 40%, but this is still not physically representative as values of around 55% can be realistically achieved [12, 74]. Duschlbauer [69] concludes that forced packing and the introduction of agglomerations are required to exceed the ceiling volume fraction. Pan et al [56, 75, 76] modified the RSA approach to enable the fibres to retain some of their 3D features. Local fibre curvature is permitted at fibre crossover points, reducing the fibre rejection rate and consequently raising the maximum fibre volume fraction to 35-40%. However, the RVE is constructed of layers and out of plane curvature is only permitted between neighbouring layers. Whilst fibres should not intersect or make contact, a minimum separation distance is required for 3D geometries to ensure finite elements do not become distorted. Iorga et al [76] and Böhm et al [66] both employ a minimum gap size that equates to $\sim 5\%$ of the cylinder (fibre) radius. Forcing a gap between fibres may lead to incorrect failure strengths, as the model will not capture local failure of the matrix or fibre-matrix interface. The local stress concentration factor increases as the gap size decreases between fibres and this is heavily influenced by neighbouring fibre pairs in high volume fraction composites [75].

Boundary conditions are known to have an impact on the size of the RVE. It is common to see periodic conditions imposed [66, 73, 77, 78], where the inhomogeneous material is approximated by an infinitely extended model material with a periodic phase arrangement. Fibres crossing the

RVE boundary are cut and shifted to the opposite face to maintain periodicity. This concept stems from modelling randomly heterogeneous transverse bundles or spherical inclusions as in [49], where the aspect ratio of the reinforcement phase is typically unity. However, enforcing periodicity for long slender fibres with larger aspect ratios causes a boundary effect, influencing the local fibre volume fraction distribution around the edge of the model, which can affect the critical size of the RVE. Gitman et al [49] show that periodic boundary conditions can be exploited to give much smaller RVEs ($\sim 30\%$) than non-periodic conditions. Periodicity can give rise to periodic configurations of damage and is therefore unsuitable for studying individual crack formation.

Saint-Venant's principle [79] can be exploited so that an approximation to the exact solution (expected from prescribing the correct boundary conditions) can be found if a sub-domain is extracted from the model at some critical 'decay length' away from the boundary (see Figure 2-1). According to [54], the decay length is typically two times the centre-centre spacing of 2D round inclusions. It is unconfirmed if this critical length is appropriate for fibres with high aspect ratios.

An alternative approach uses an embedded cell to avoid imposing periodicity [55, 80], where the embedded core region is some critical distance away from the boundary. The core is embedded in a homogeneous material that acts to transmit the applied load [67]. It allows the core to be studied at a high spatial resolution, but similar to the periodic approach, embedding causes perturbations in the local stress and strain fields at the boundary of the core. This resulting boundary layer may be the length scale of the inclusion, which will increase for non-linear material behaviour [81]. Another concern is assigning material properties to the homogeneous region. The outer region may be described by some macroscopic constitutive law [82], determined self-consistently from the behaviour of the core [83], or it may take the form of a coarse description of the global phase arrangement [84].

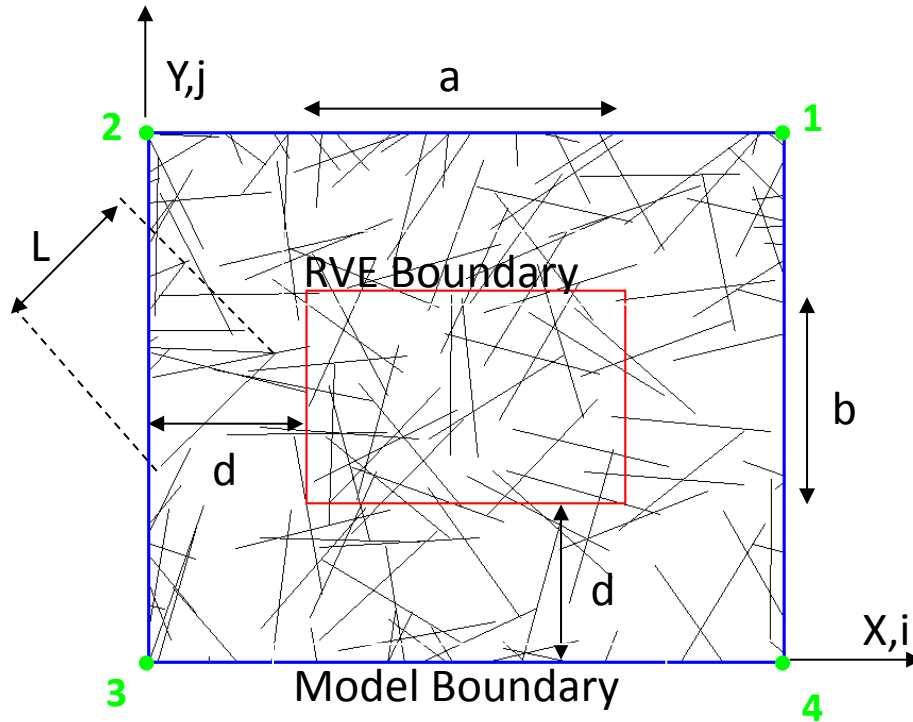


Figure 2-1 RVE generated to exploit Saint - Venant's principle. d represents the decay length. i and j represent the number of periods in the x and y direction respectively.

2.1.2 Size effects in meso-scale RVEs

The behaviour of heterogeneous materials is often described using the concept of a representative volume element (RVE). According to Hill [85], the RVE should be a volume of heterogeneous material that is sufficiently large to be statistically representative, ensuring a sample is taken of all micro-structural heterogeneities that occur in the composite. This is commonly known as the Micro-Meso-Macro principle [86], as a separation of scale is required. Alternatively, Drugan and Willis [87] assert that the RVE should contain the smallest volume of material to define the macroscopic structure, but the volume should be large enough to remain constitutively valid.

The RVE must be large enough to be statistically and micro-structurally relevant, but small enough to be computationally efficient, as previously outlined in Part 1. According to the RVE concept, it is necessary to define

some quantitative criteria that a sample of material must satisfy, in order to be considered representative. Hill's condition [80] is commonly used in the literature as a stress/strain based criterion to determine critical RVE size, assuming that the effective properties of a heterogeneous elastic material are energetically and mechanically equivalent. The kinetic variables (stresses) are compared with the kinematic variables (strains) on the macroscopic scale, and the RVE is defined as the minimum material for which the response does not depend on the volume.

A review in [49] indicates that there is no systematic way to quantify the critical RVE size, but it is important to note that the geometry of the RVE may be influenced by size effects. Size effects can be divided into two categories; deterministic size effects and statistical size effects.

Deterministic size effects can be caused by the ratio between the macroscopic material scale and the microscopic fracture zone and/or the influence of boundary conditions [49]. The RVE should produce the same response under macroscopically uniform boundary conditions (either displacement or traction) if the size of the RVE is sufficiently large [88-90]. According to [85], the displacement and/or traction fields may fluctuate about a mean value due to perturbations at the RVE boundary. However, the effects of such fluctuations become negligible within a few wavelengths of the boundary if the RVE size is sufficiently large, due to St Venant's principle.

Statistical size effects are caused by uncertainty arising from poor sampling in smaller specimens. An example of a statistical size effect includes the Weibull weakest link theory [91] where the strength of a brittle material tends to decrease with increasing specimen volume, as the probability of it containing a critical flaw increases. Other examples for random discontinuous composites include poor representation of the fibre orientation distribution (departure from isotropy) and poor spatial distribution of fibres (departure from homogeneity) within smaller samples.

It is unlikely that the true effective mean material properties can be realised if deterministic size effects are present, as they will always dominate. However, statistical size effects can be controlled by increasing the number of realisations to overcome the statistical uncertainty.

Statistical measures are commonly used to establish the critical RVE size by determining the condition of statistical homogeneity. Convergence of the effective homogenised properties is often studied to determine the characteristic RVE size. It is difficult to establish exactly when the effective size has been reached, and common statistical methods are reviewed in [92]. Kanit et al [93] relate RVE size to number of realisations and estimation accuracy for linear-elastic properties. In their approach a relative error is calculated for the effective properties of models of increasing volume, which is reverse engineered to determine the final RVE size for a given precision. The accuracy of this model strongly depends on the number of realisations performed and can require a large number of computations (~ 2500). Clearly smaller RVE sizes can also be adopted to determine effective properties, but a greater number of realisations are required.

Gitman et al [49] developed a stopping criterion for non-linear properties, using a statistical analysis on the average stress from numerical computations. The procedure uses a *Chi-square criterion* to assess how far a single response deviates from the mean response of all realisations. Gitman's criterion is less time consuming than Kanit's, because only 5 repeats are used for each volume size. However, such a small number of realisations cannot be sufficient unless the volume of material is large, as reported in [93].

An alternative statistical-numerical stopping criterion developed in [92] reduces the number of computations compared with Kanit, offering a compromise between RVE size and CPU time, and is suitable for both linear and non-linear materials. An uncertainty range is calculated for the relative error using a bootstrap technique, which measures the accuracy of the statistical estimate.

Kanit et al [93] demonstrated that different critical RVE sizes exist for different effective properties, such as in the case of thermal conductivity or linear elasticity. In [49] the RVE size for hardening behaviour was ~ 1.5 times larger than for a linear-elastic material, but an RVE could not be established for softening because localised fracture behaviour caused statistical inhomogeneity. In [92] the non-linear RVE corresponding to fracture properties was 8-10 times larger than the linear case.

Limited data exists in the literature for defining the critical size of RVEs for non-aligned discontinuous fibre composites. Results from the laminated strand model [65] show that the variation reduces for increasing coupon thickness and reducing fibre length, (both of these parameters result in more fibre strands per unit area which increases homogeneity of fibre architecture). The RVE size is suggested to be between 3-5 times the fibre length (127mm and 152mm for [65]) based on the convergence of the variation, which is of structural dimensions. However, based on the convergence of the effective moduli, the RVE size is more likely to be 1-2 times the fibre length. The Poisson's ratio appears to be largely unaffected by the RVE size. Iorga et al [76] support these findings by comparing the laminated strand model to an FEM approach, using a random windowing technique. Generally, the FEM produces lower predictions than the analytical approach. Kari [68, 73] investigated the size of 3D cubic RVEs for short fibre composites, assuming periodic boundary conditions. A critical edge length of 1.5 was selected for fibres with an aspect ratio of 5 (length in mm was not quoted), but only 3 realisations per volume were analysed without consideration of the statistical confidence.

Table 2-1: Summary of parameters used in the FE model

Fibre Modulus	144000	MPa
Matrix Modulus	3350	MPa
Matrix Poisson's Ratio	0.38	
Carbon Tow Size	24000	
Tow Volume Fraction	60	%
RVE Thickness	3.5	mm

2.2 Methodology

2.2.1 Generation of meso-scale RVEs

Planar 2D fibre architectures have been generated by a modified random sequential adsorption scheme programmed in Visual Basic®. Fibre bundles are deposited over a region of interest (ROI), indicated by the outer square in Figure 2-2. Random numbers within upper and lower bounds are generated for the x and y coordinates of the centre of mass for each fibre bundle. A third random number is used to generate a fibre orientation about the centre of mass. This can be completely random or can be returned from a statistical distribution depending on the level of fibre alignment. Fibre intersections are ignored and therefore no limitation is imposed on the fibre volume fraction. This 2D approach is computationally inexpensive, and therefore enables larger volumes of material to be studied. Inevitably there is a limit to the level of physical detail that can be modelled, but capturing the stochastic fibre distribution is considered to be more important, based on the level of variation in material properties experienced experimentally [18, 57, 94-96].

In the present work the ROI is two fibre lengths longer and wider overall than the RVE boundary. A Cohen-Sutherland [97] line clipping algorithm is used to trim the fibre bundles to the model/RVE boundary (Figure 2-2). This ensures that both bridging and ending fibres are captured within the model according to the specified fibre length. This is an alternative approach to the moving-window average method employed in [65] and ensures that the target fibre volume fraction is exactly as specified within the RVE boundary. Bundles are sequentially deposited until the volume of fibre meets the target volume fraction for the inner RVE (shown as a black box in Figure 2-2). A drawback of this method is that it doesn't capture the levels of material heterogeneity and local fibre volume fraction variations produced during manufacturing. However, this can be incorporated in the future using process-specific simulation tools to generate more representative networks according to the spatial distribution of fibres resulting from the preforming/moulding process.

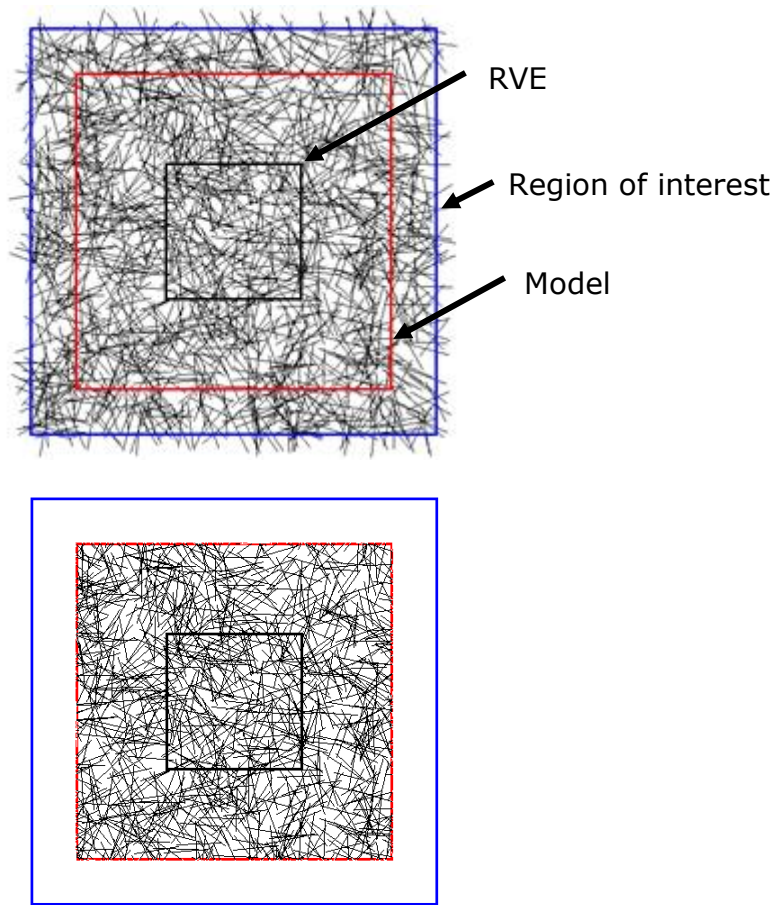


Figure 2-2 Schematic of random sequential adsorption model. (Top) As-deposited state, (Bottom) Trimmed state. Black lines represent carbon bundle centre lines

2.2.2 Finite element modelling

The current modelling strategy simulates the architecture at the mesoscopic level, using 1D beam elements in ABAQUS (type B22) to represent carbon bundles. Each beam is assumed to have a circular cross-section, where the diameter is assigned as a function of the filament count and tow volume fraction (V_{tow}). The internal structure of each bundle contains resin, and therefore the volume of deposited bundles ($V_{deposited}$) is adjusted to satisfy the target volume fraction of the laminate (v_f):

$$V_{deposited} = \frac{V_f}{V_{tow}}$$

Equation 2-1

The tensile stiffness of each beam is calculated using a simple rule of mixtures approach using V_{tow} and the modulus of a single filament. The matrix material is modelled using a regular array of 2D, plane stress continuum elements (ABAQUS type CPS8R). Beam elements are fixed to the solid elements using the *EMBEDDED ELEMENT technique, a type of multi-point constraint within ABAQUS/Standard. The translational degrees of freedom of each beam element are eliminated when it is embedded, becoming constrained to the interpolated values of the corresponding degrees of freedom of the host (matrix) element. Embedding eliminates the need for a complex meshing algorithm to pair the coincident nodes on the fibres to the resin and thus saves time in mesh generation.

It must be noted that the present analysis is a 2D simplification of a 3D problem. The local interaction between fibres in the vicinity of a fibre crossover point is of a genuine 3D nature. While no attempt has been made to capture the full 3D behaviour using the methodology presented in this Chapter, it is believed that the stress-strain response of the 2D model is similar to that of a segment within a real structure. The 2D model is effectively a fibre net of an irregular pattern which is rigidly bonded at the point of intersections. This represents one extreme scenario, with the other extreme being that fibres are free to move relative to each other at the intersection points. The reality falls, of course, somewhere in between. Some primitive analyses conducted by the authors seem to suggest that the differences between the two extremes are insignificant as far as the stresses in the fibres are concerned.

A comparison is provided in Appendix B for the effect of using the embedded element technique versus a more conventional unstructured meshing approach. Simulations show that there is less than 1% error between the two approaches when comparing the in-plane moduli and Poisson's ratios. This error can be partially attributed to mesh density, which is also discussed in more detail in Appendix B. These low errors are considered to be acceptable in the current context, since this approach

eliminates problems with mesh density and distorted elements around fibre crossover points.

2.2.3 Boundary conditions

Effective material properties of each random fibre architecture have been approximated by applying periodic boundary conditions, assuming translational symmetries in the x and y directions and ignoring traction conditions [52]. Two modelling schemes have been investigated, exploiting Saint-Venant's principle to establish the critical decay length of the local incorrectness of the periodic boundary conditions [54].

The periods of translation in the x and y direction are ai and bj respectively, where a is the length of the cell, b is the width and i and j are the number of periods. The cell is subjected to a set of macroscopic strains $\{\varepsilon_x^0, \varepsilon_y^0, \gamma_{xy}^0\}$, which are introduced as three extra degrees of freedom in the FE analysis at three individual dummy nodes. Each of these nodes can be prescribed to achieve a macroscopically uniaxial strain state.

The following relationship is between macroscopic strains and relative displacements at a point P in the unit cell relative to a point P' at an identical location in an arbitrary cell:

$$U_{P'} - U_P = ia\varepsilon_x^0 + jb\gamma_{xy}^0 \quad \text{Equation 2-2}$$

$$V_{P'} - V_P = jb\varepsilon_y^0 \quad \text{Equation 2-3}$$

The translational symmetries in the x -direction for boundaries $x=0$ and $x=a$ ($i=1$ and $j=0$) are as follows:

$$U_{x=a} - U_{x=0} = a\varepsilon_x^0 \quad \text{Equation 2-4}$$

$$V_{x=a} - V_{x=0} = 0 \quad \text{Equation 2-5}$$

The translational symmetries in the y -direction for boundaries $y=0$ and $y=b$ ($i=0$ and $j=1$) are as follows:

$$U_{y=b} - U_{y=0} = b\gamma_{xy}^0 \quad \text{Equation 2-6}$$

$$V_{y=b} - V_{y=0} = b\varepsilon_y^0 \quad \text{Equation 2-7}$$

It should be noted that some of these boundary conditions are not fully independent at the corners of the unit cell, since a corner node is shared by two sides belonging to different pairs. Whilst the above boundary conditions are mathematically consistent, many finite element codes will diagnose them as a source of error and the user must exclude the corner nodes from the node sets for each boundary. Corners 2, 3, 4 (see Figure 2-1) are associated with corner 1 by the following translations, according to Equation 2-2:

$$-U_2 + U_1 = a\varepsilon_x^0 \quad \text{Equation 2-8}$$

$$-V_2 + V_1 = 0 \quad \text{Equation 2-9}$$

$$-U_3 + U_1 = a\varepsilon_x^0 + b\gamma_{xy}^0 \quad \text{Equation 2-10}$$

$$-V_3 + V_1 = b\varepsilon_y^0 \quad \text{Equation 2-11}$$

$$-U_4 + U_1 = b\gamma_{xy}^0 \quad \text{Equation 2-12}$$

$$-V_4 + V_1 = b\varepsilon_y^0 \quad \text{Equation 2-13}$$

The distribution of nodal displacements can be integrated with respect to the nodal position along the boundary in question, in order to obtain the average displacement of the RVE. The average strain in the x -direction along the RVE (Figure 2-2) can therefore be calculated as follows:

$$\varepsilon_x^{ave} = \frac{1}{ab} \int_{y=0}^{y=a} u^b dy \quad \text{Equation 2-14}$$

where u^b is the displacement in the x-direction along width b of the RVE.

In principle, the average stress can be calculated in the same manner, using the distribution of tractions from the nodal values. However, nodal reaction forces can only be requested for nodes subjected to boundary conditions in ABAQUS (i.e. on the model boundary) and therefore are unsuitable for the inner RVE boundary. The average RVE stress is calculated as a volume average quantity, by taking into consideration separate contributions from both resin and fibre within the RVE boundary

$$\sigma_x^{ave} = \frac{1}{abt} \left(\int \sigma_x^{\text{fibre}} dV + \int \sigma_x^{\text{resin}} dV \right) \quad \text{Equation 2-15}$$

where t is the RVE thickness. Separate average stress contributions are required because of the mixed dimensionality of the model and the embedded element approach. This approach is implemented in ABAQUS/Standard by using the SVOL parameter to determine the integrated section volume of each CPS8R element (resin) and the IVOL parameter is used to find the integration point volume for each B22 element (fibre). The average stress in the x-direction can be expressed as

$$\sigma_x^{ave} = \frac{1}{V} \left[\sum_b \left(\sum_i \frac{SF1_{bi} \cos \theta_b}{A_b} SVOL_{bi} \right) + \sum_c \left(\sum_i S11_{ci} IVOL_{ci} \right) \right] \quad \text{Equation 2-16}$$

where subscripts b and c represent the number of beam elements and continuum elements respectively in the model. Subscript i is the integration point number of the relevant element. $SF1$ is the section force of the beam and it is resolved in the loading direction according to the fibre angle θ . $S11$ is the stress component for the matrix material in the loading direction x . A_b is the cross-sectional area of the continuum element b . The average stress in other directions can be similarly

calculated by substituting the relevant stress component into Equation 2-16 and resolving the section force of the beams in the appropriate direction. The average stress and strain calculations have been implemented into a Python script within ABAQUS/CAE in order to calculate the effective moduli.

2.2.4 Determining the RVE Size: Stopping criterion

The stopping criterion developed by Kanit et al [93] has been adopted in the current work to determine how many realisations are required, based on the stabilisation of the estimated mean and variation. The size of the RVE can be directly related to the mean value of the effective property Z , of the domain size V , for different independent realisations n . The absolute error can be expressed as a function of the standard deviation of Z , $D_z(V)$

$$\varepsilon_{abs} = \frac{2D_z(V)}{\sqrt{n}} \quad \text{Equation 2-17}$$

Hence the relative error can be calculated as follows:

$$\varepsilon_{rel} = \frac{\varepsilon_{abs}}{Z} = \frac{2D_z(V)}{Z\sqrt{n}} \quad \text{Equation 2-18}$$

The relative error has been calculated for all scenarios and has been presented as a function of number of realisations. An example is shown in Figure 2-3 for the material with 5mm fibre length, 50% fibre volume fraction and a cell size of 5mm×5mm. A relative error threshold of 5% has been used as the stopping criterion for all subsequent simulations, which represents a confidence of 95% in the mean value of the effective property Z . For example, the curve in Figure 2-3 crosses the 5% relative error threshold at 315; therefore one can be 95% confident that the mean value has been achieved after 315 realisations.

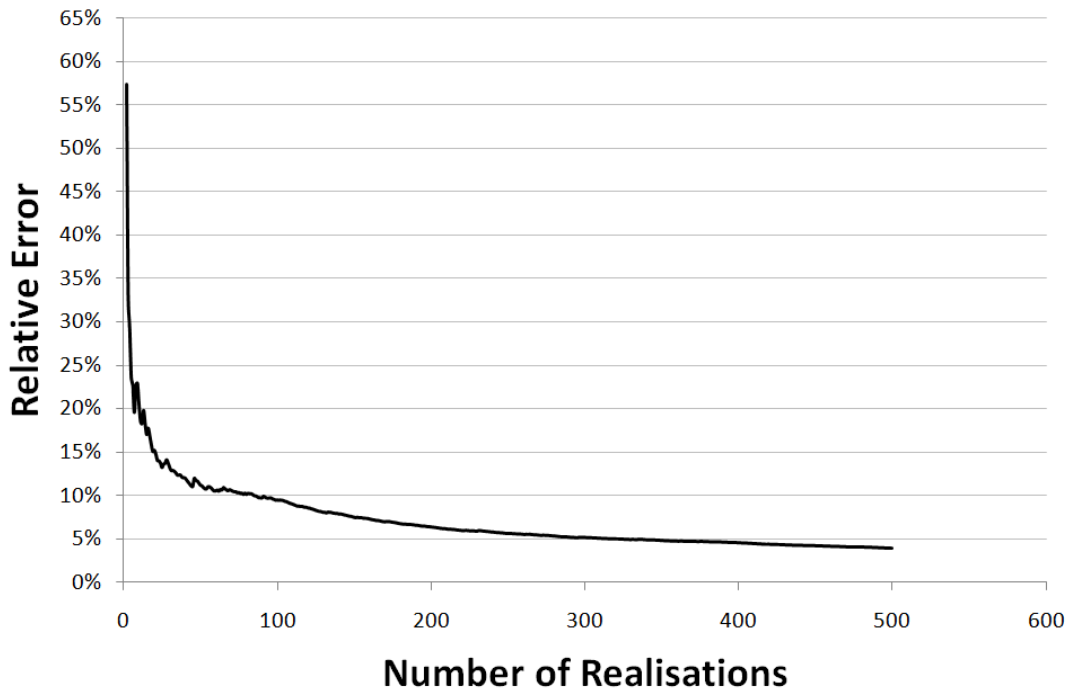


Figure 2-3 Relative error for E_1 as a function of number of realisations. Models consisted of a 5mm fibre length at 50% volume fraction. Cell size was 5mm \times 5mm.

2.2.5 Measure of departure from isotropy

For quasi-random materials, the rate of convergence of the effective elastic properties is expected to be a function of fibre orientation. A measure of the level of transverse isotropy (1-2 plane) has been determined for each RVE using the methodology outlined in [76], to provide a quantitative measure of any bias in the fibre orientation distribution. The departure from isotropy can be expressed as

$$\Delta = \sqrt{\Delta_1^2 + \Delta_2^2} \tag{Equation 2-19}$$

where

$$\Delta_1 = \frac{2(A_{11} - A_{22})}{(A_{11} + A_{22})} \tag{Equation 2-20}$$

$$\Delta_2 = 2 \frac{A_{11} - A_{12} - 2A_{66}}{A_{11} + A_{22} + 2A_{66}} \quad \text{Equation 2-21}$$

The required coefficients from the stiffness matrix for a 2D plane stress problem can be calculated from the engineering constants as follows [98]

$$A_{11} = \frac{E_1}{(1 - (v_{12}v_{21}))} \quad \text{Equation 2-22}$$

$$A_{22} = \frac{E_2}{(1 - (v_{12}v_{21}))} \quad \text{Equation 2-23}$$

$$A_{12} = \frac{v_{12}E_2}{(1 - (v_{12}v_{21}))} \quad \text{Equation 2-24}$$

$$A_{66} = G_{12} \quad \text{Equation 2-25}$$

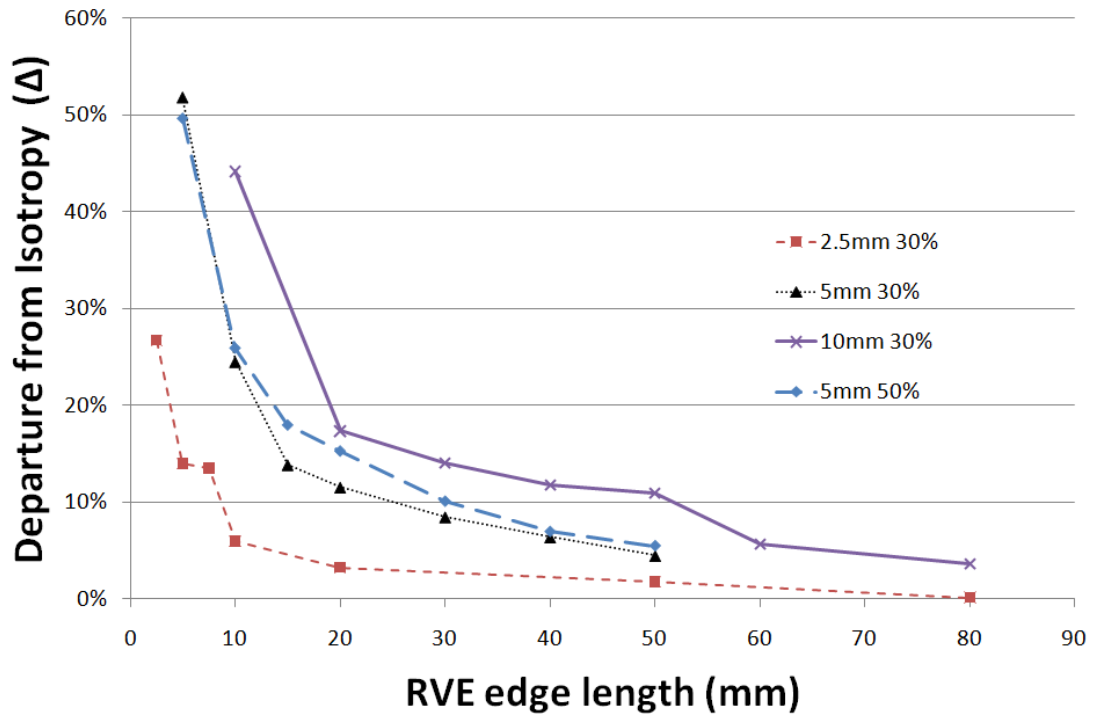


Figure 2-4: Departure from isotropy values as a function of RVE edge length.

Equation 2-19 yields a value of zero for transversely isotropic materials such as SMC, and a value of ~ 2.4 for a UD carbon/epoxy prepreg, using data from [99]. The average departure from isotropy has been calculated for all material scenarios and is presented as a function of the RVE size in Figure 2-4.

2.2.6 Measure of homogeneity

The rate of convergence of the elastic properties with increasing RVE size is also governed by the level of fibre homogeneity (local variation in fibre volume fraction). Iorga et al [76] measured the level of statistical inhomogeneity by comparing the stiffness matrices from two non-identical realisations of the same window size. This approach does not enable the orientation effects (departure from isotropy) to be considered independently from the homogeneity effects.

In the current work, models have been discretised into smaller sub-regions and the local volume fraction v_f has been studied to provide a statistical measure of inhomogeneity, as depicted in the greyscale images in Figure 2-5. This approach is based on that of Lu and Torquato [100], who proposed a *coarseness* parameter (Λ) to provide a quantitative measure of non-uniformity in fibre coverage. The standard deviation of the local volume fraction is scaled as follows:

$$\Lambda = \frac{1}{\bar{V}_f} \sqrt{\langle V_f^2 \rangle - \bar{V}_f^2} \quad \text{Equation 2-26}$$

where \bar{V}_f is the average global volume fraction of the RVE. A value of zero in the current context indicates that all sub-regions contain the same amount of material and the local spatial distribution of fibre is therefore considered to be homogeneous. Curves are presented in Figure 2-6 for the range of material parameters currently under investigation.

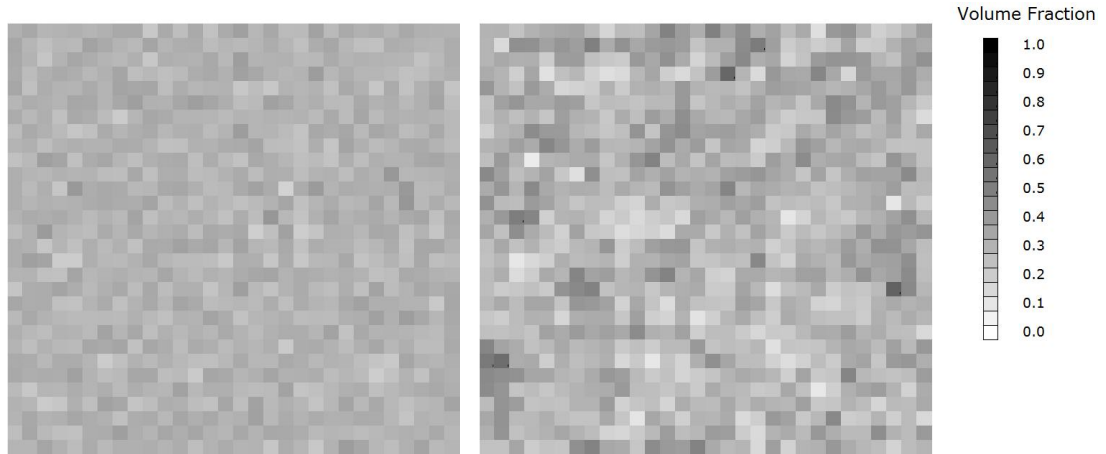


Figure 2-5 Greyscale images showing the local volume fraction variation for two fibre architectures: (left) 2.5mm fibre length at 30% v_f (right) 50mm fibre length at 30% v_f . Both models were 300mm \times 300mm and were discretised into 10mm \times 10mm regions.

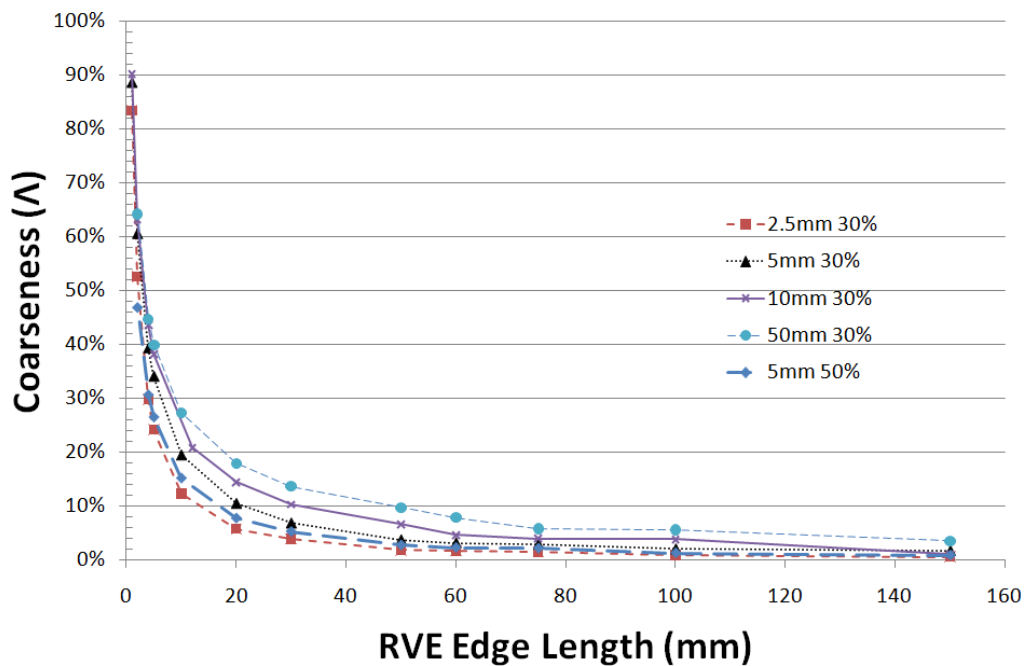


Figure 2-6 Coarseness parameter as a function of RVE edge length.

2.3 Results

2.3.1 Decay length of boundary conditions

The critical decay length has been established for a range of models containing different fibre lengths (2.5mm, 5mm, 10mm), volume

fractions (10%, 30%, 50%) and orientation distributions (random, aligned). The RVE boundary length was set to at least two times the fibre length in all cases, as suggested in [76].

Figure 2-7 shows an example of how the in-plane stiffnesses vary with increasing decay length (d') for a model consisting of 10mm long fibres, randomly distributed at a fibre volume fraction of 10% (results are normalised wrt fibre length l). All three stiffness values converge after a decay length of two times the fibre length (20mm). All three curves plateau at $d/l = 2$ and the error between this point and $d/l=5$ is less than 1% for all three stiffness components. Stress contours plotted in Figure 2-10 show that a decay length ratio of $d/l=2$ gives a good approximation of the stress field within the inner RVE boundary. All three plots share similar features, but the magnitude of the stresses around the boundary of $d/l=0.5$ are generally lower than $d/l=2$ and $d/l=5$. The displaced shape for $d/l=2$ is identical to $d/l=5$. The edges are not straight and therefore conventional displacement boundary conditions for this RVE model would indeed be inappropriate, which further supports the use of Saint-Venant's principle for heterogeneous materials. Results showing the effects of varying the decay length are presented in Appendix B.3. The alternative approach of using homogeneous material in the surrounding region with the equivalent macro-scale properties is also studied in Appendix B.3, named 'homogeneous approach' and compared with the current 'heterogeneous approach'. Results show that using macro-scale properties in the surrounding region does not produce the same stress distribution at the RVE boundary compared with that of the current approach, therefore the homogeneous approach will not be considered any further in this thesis.

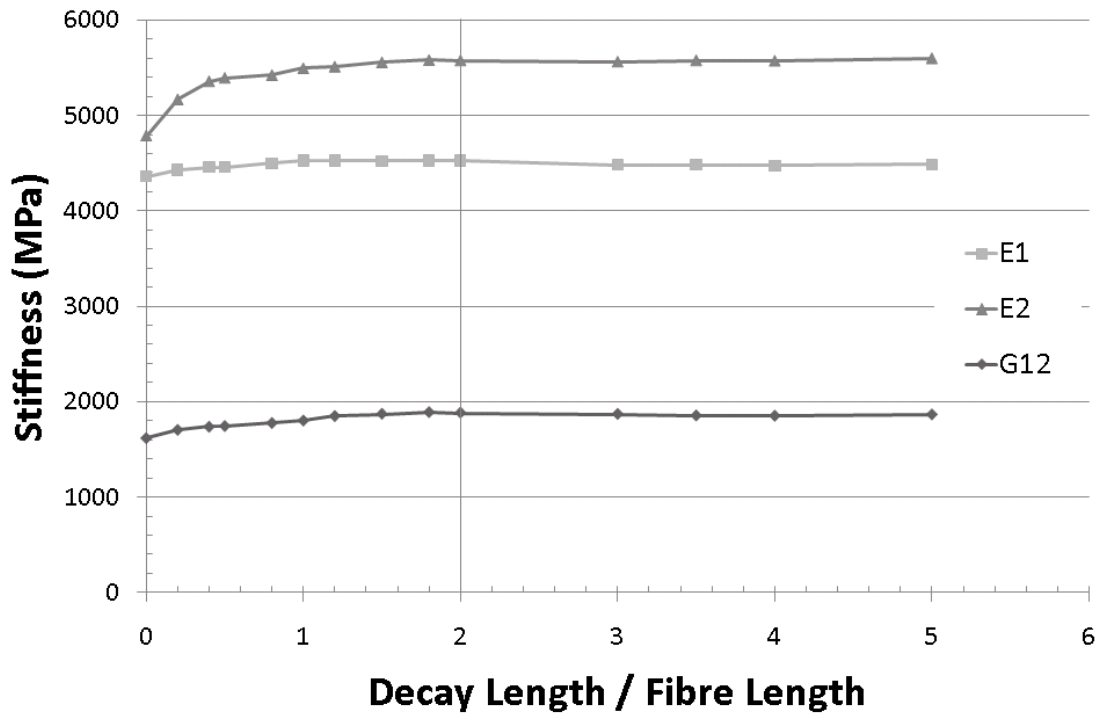


Figure 2-7: Effect of decay length on the in-plane stiffnesses for an RVE containing 10mm long fibres at 10% v_f using the heterogeneous approach. (Decay length is plotted as a function of fibre length).

2.3.2 Convergence of effective properties

Average values for all simulations are presented in Table B-5, including the total number of realisations performed for each scenario. In-plane tensile stiffness values (E_1) are presented in Figure 2-8 as a function of edge length normalised with respect to fibre length (L/l). Simulations were also performed in the E_2 direction but the average error between E_1 and E_2 was generally less than 5% (less than the relative error threshold used to determine convergence), therefore values in Figure 2-8 were averaged from E_1 and E_2 .

Figure 2-8 shows there is an increase in the average tensile stiffness for increasing fibre length and fibre volume fraction for any given RVE size. The average tensile stiffness decreases for increasing RVE size, before reaching a plateau value, for all of the material architectures in Figure 2-8. The average stiffnesses for materials with a volume fraction of 30%

are 4683MPa, 7880MPa and 12227MPa for fibre lengths of 2.5mm, 5mm and 10mm respectively. The highest average stiffness is 13576MPa (5mm fibre length with a 50% volume fraction). The convergence point of the effective stiffness occurs when the RVE edge length is 4 times the fibre length in all cases ($L/l=4$). There is less than 1% error between $L/l=4$ and the next available data point for each material ($L/l=5$ is not available for all scenarios).

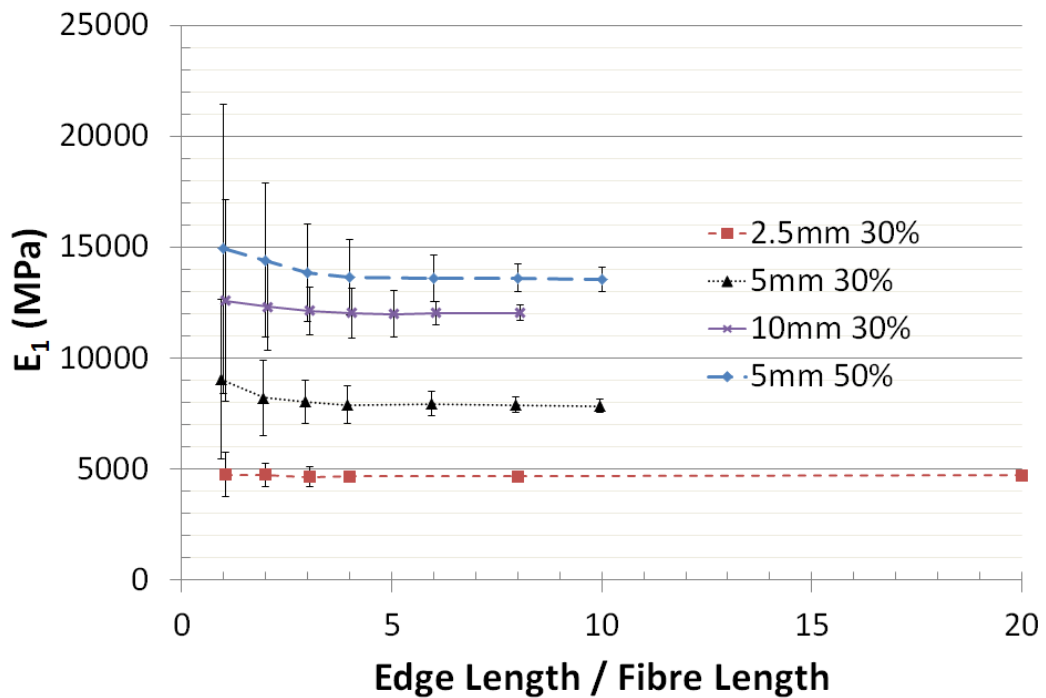


Figure 2-8: In-plane tensile stiffness E_1 as a function of RVE edge length normalised by fibre length. All x-axis values are integers; however some data points have been offset ± 0.05 along the x-axis to provide clarity.

Figure 2-9 shows a summary of the shear stiffness G_{12} . Convergence also occurs at $L/l=4$ and the effective shear stiffness is generally higher for smaller models below this L/l threshold. However, this is not the case for the 10mm fibre length, as the shear modulus appears to be lower for smaller models below $L/l=4$. The average shear stiffness for materials with a volume fraction of 30% is 1719MPa, 2828MPa and 4431MPa for fibre lengths of 2.5mm, 5mm and 10mm respectively. The highest average stiffness is for the 5mm fibre length with a 50% v_f ; 4910MPa.

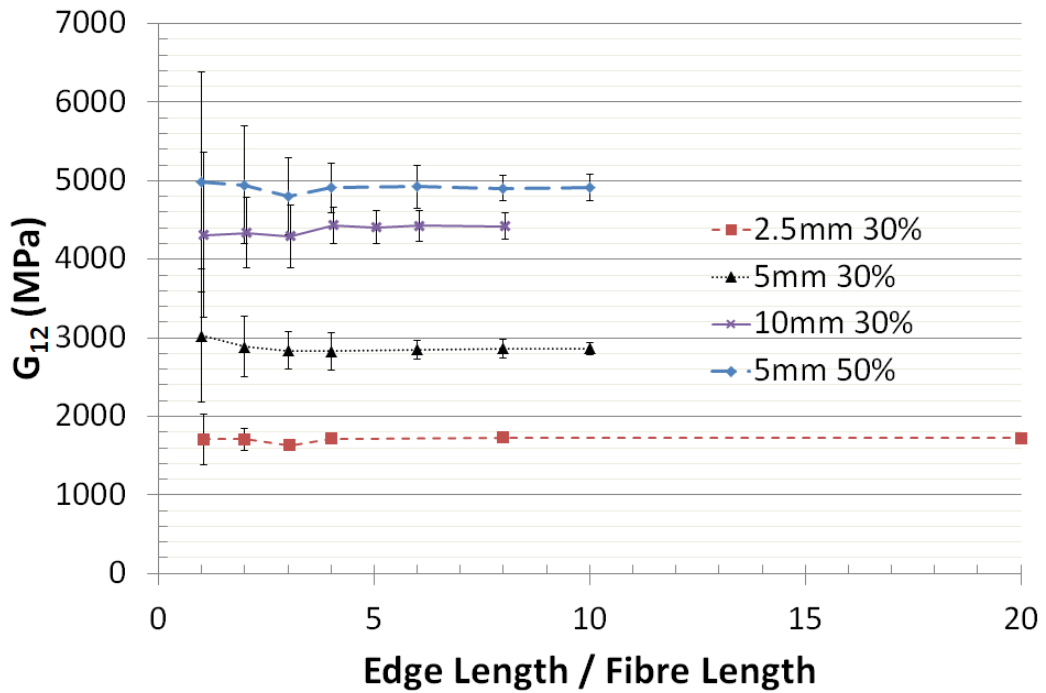


Figure 2-9: In-plane shear stiffness G_{12} as a function of RVE edge length normalised by fibre length. All x-axis values should be integers; however some data points have been offset ± 0.05 to provide further clarity.

The tensile and shear moduli are initially high for smaller models when the fibre length is close to the RVE scale, as fibres can bridge the cell (cross two boundaries) causing the fibre to be directly loaded by the boundary conditions. As the cell size increases, stress develops in the fibres via shear mechanisms at the fibre/matrix interface, which results in a lower average stress. This convergence point is higher than the critical L/l thresholds previously quoted in [68, 76], of 1-2 times the fibre length. This can be partially attributed to the difference in stiffness ratio between the constituent materials and the resulting stress gradient in the fibre/matrix, which affects the required mesh density. A mesh sensitivity analysis was performed in Section B.2 for the embedded beam element approach, to ensure the mesh was fine enough to capture the stress gradients at the bundle ends. This cannot be confirmed for the models presented in the literature, since in some cases the FE discretisation was restricted by memory limitations [76].

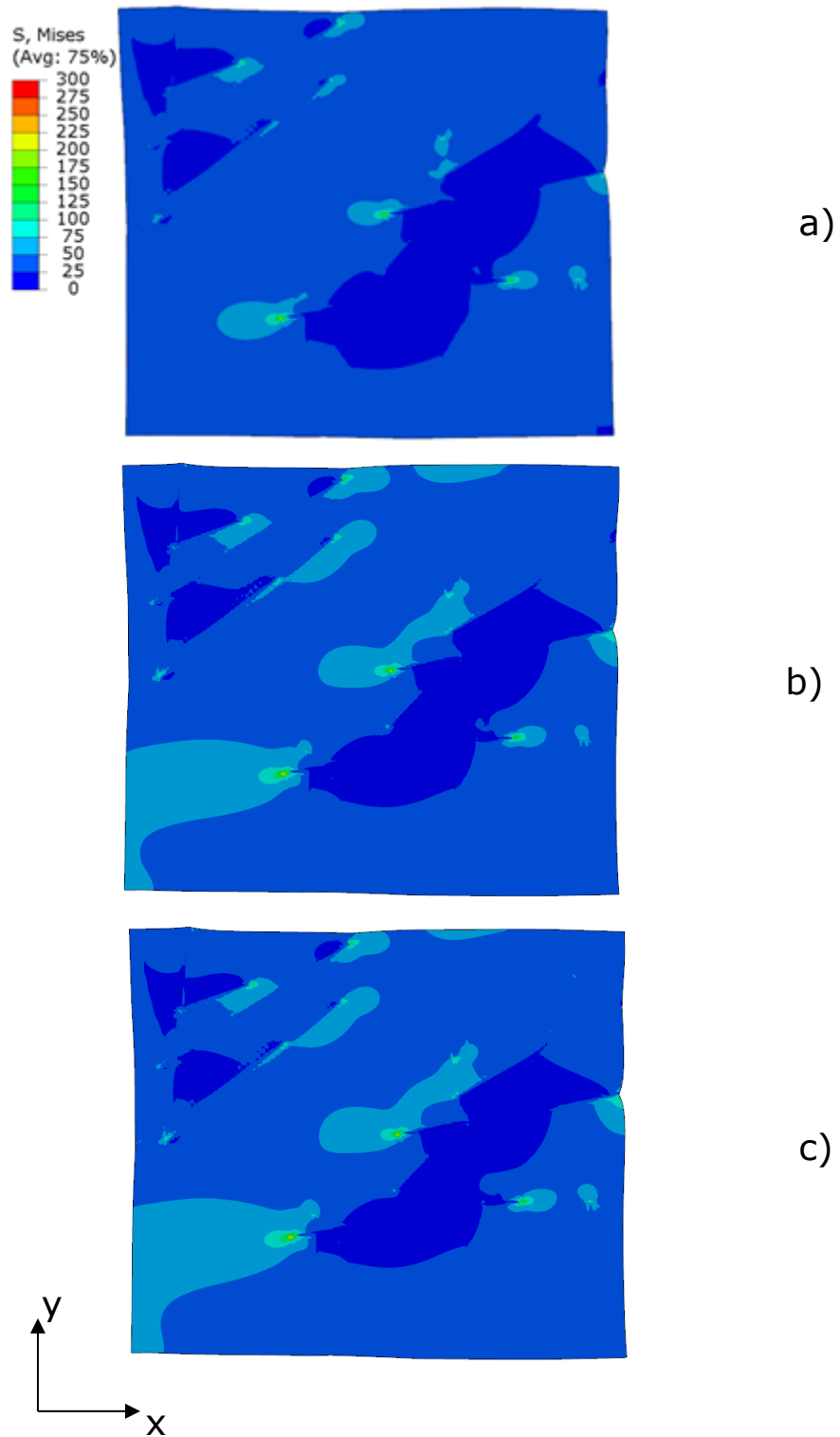


Figure 2-10 Von Mises stress contours extracted from the inner RVE boundary for three different decay length/fibre length ratios using the heterogeneous approach a) 0.5, b) 2, c) 5. RVE consisted of 10mm long fibres at 10% v_f . Loading was in the x-direction. Deformation factor was set to 10 and all plots are scaled to the same peak stress of 300MPa.

Figure 2-11 indicates that the average Poisson's ratio is independent of increasing RVE size. Whilst only results for the 10mm 30% v_f case are presented, the same trend was observed for all other material scenarios studied, supporting results previously reported in [76] and [65]. The average error between v_{12} and v_{21} is less than 3% in all cases; hence a single 'average' line is presented for both. There is no distinguishable trend for the magnitude of the Poisson's ratio as a function of fibre length or fibre volume fraction. The average Poisson's ratio for the 2.5mm, 5mm and 10mm materials with 30% v_f are approximately the same; 0.367, 0.370, 0.360 respectively. The average Poisson's ratio for the 2.5mm, 50% v_f material is 0.360.

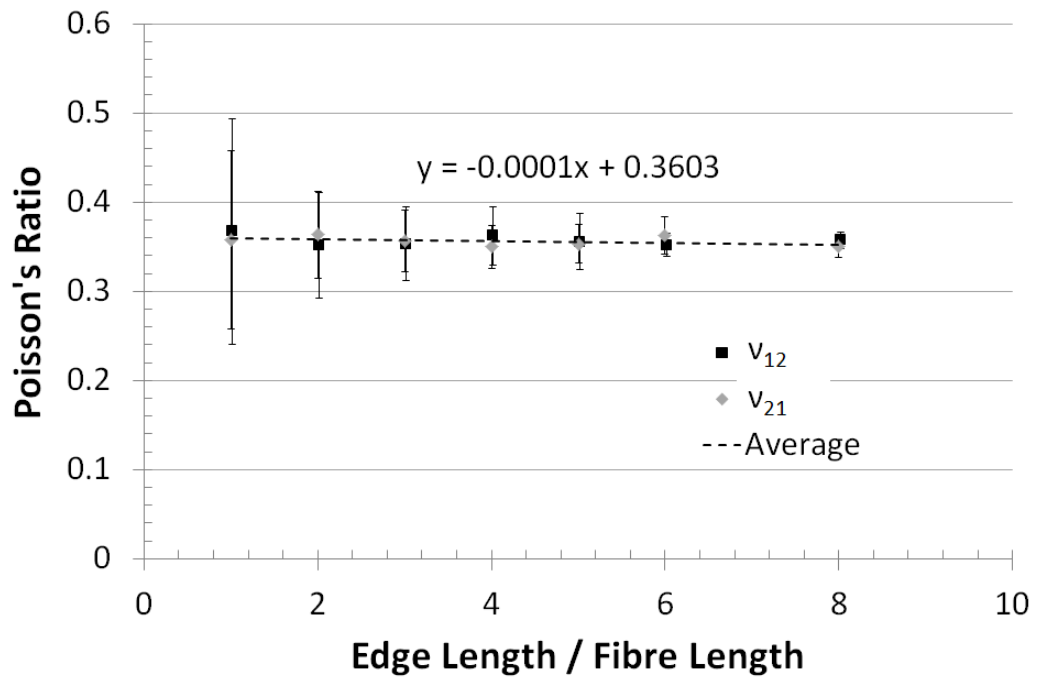


Figure 2-11: Effect of increasing RVE size on the Poisson's ratio. Example curve for the 10mm fibre length / 30% v_f case. Linear equation for trend line is included. v_{12} data series has been offset by 0.02 on the x-axis from v_{21} to provide clarity between standard deviation bars.

The curves presented in Figure 2-8 and Figure 2-9 can be split into two distinct zones based on the convergence of the stiffness at $L/l=4$. A representative average of the effective stiffness cannot be achieved for models where $L/l < 4$ because deterministic size effects are present,

caused by bridging fibres and the material scale. The effective stiffness is constant for $L/l > 4$, but the variation continues to decrease for larger models, as shown in Table B-5. Statistical size effects dominate the properties of larger models, presenting a trade-off between the size of the RVE and the number of realisations required to achieve a representative average. The fundamental question is whether it is more efficient to test many smaller models or fewer larger ones, in order to achieve the effective mean properties at the desired confidence level of 95% ($\epsilon_{rel} = 5\%$).

2.3.3 Convergence of variation

The variation depends on the magnitude of the statistical size effects, which are a function of the departure from isotropy Δ and the coarseness Λ (shown in Figure 2-4 and Figure 2-6 respectively). Both parameters are influenced by fibre length and volume fraction, where fibre length appears to be more dominant in both cases. The departure from isotropy converges quicker than the coarseness; $\Delta = 0.14\%$ for an RVE edge length of 80mm, compared with $\Lambda = 0.6\%$ for an edge length of 150mm (values taken for the 2.5mm fibre length material).

The coarseness and the departure from isotropy parameters both strongly follow power law relationships

$$\Lambda = k L^{-\alpha} \quad \text{Equation 2-27}$$

$$\Delta = k L^{-\beta} \quad \text{Equation 2-28}$$

where L is the RVE edge length in mm and k , α and β are constants. A summary of these parameters is listed in Table 2-3 along with the R^2 coefficient for the goodness of fit. Increasing fibre volume fraction and decreasing fibre length increases the number of fibre segments per unit volume, which improves the probability of achieving a statistically representative sample. This is illustrated in Figure 2-5, in terms of the coarseness parameter. The map of local volume fraction variation is smoother for the shorter 2.5mm fibres than for the 50mm. The

coarseness value is lower for the 2.5mm fibre length (12% compared with 27%), and the minimum and maximum values for the local v_f are much closer to the 30% global mean than for the 50mm material (2.5mm -24% min & 34% max, 50mm -7% min & 61% max).

The standard deviation of the effective properties also follows the same power law as Equation 2-27 and Equation 2-28, as previously suggested in [93]. The coefficients are listed in Table 2-3 for the elastic constants E_1 , G_{12} and ν_{12} , where γ is the scaling exponent and k is a constant. γ is approximately unity in all cases and is much more consistent than α and β , while k is proportional to fibre length and fibre volume fraction. This power law fit has subsequently been used to calculate the number of realisations required to achieve a relative error of 5% for larger RVE sizes, by rearranging Equation 2-18. The number of realisations for each RVE size has been multiplied by the number of degrees of freedom in each model. This provides a measure of CPU effort required to achieve a representative set of elastic constants as a function of RVE size.

Figure 2-12 shows CPU effort as a function of RVE edge length for E_1 , G_{12} and ν_{12} , and a summary of the critical RVE sizes are presented in Table 2-2. Filled points in Figure 2-12 represent the data from the simulations (Table B-5) and lines of best fit have been calculated using the power law from Equation 2-27 and Equation 2-28 and parameters in Table 2-3. A local minimum occurs for each material architecture, indicating the optimum RVE size in terms of CPU effort required to achieve a representative value for E_1 . This local minimum occurs at $L= 24\text{mm}$, 68mm and 94mm for the 2.5mm, 5mm, and 10mm fibre length materials with a 30% volume fraction, indicating that the RVE size is fibre length dependent. The RVE size is also volume fraction dependent, as the minima for the 50% v_f material is at $L=82\text{mm}$, compared with 68mm for the 30% v_f counterpart. This result is unexpected, since higher fibre volume fractions improved the level of isotropy and coarseness in Figure 2-4 and Figure 2-6 respectively, therefore theoretically reducing material variability.

The convergence of the CPU effort appears to be dominated by the number of realisations, rather than the total number of degrees of freedom for each RVE size. Convergence typically occurs when $n=1$, which implies that it is more computationally efficient to test one large model rather than several smaller ones. In practice however, this is not always feasible depending on the scale of the problem and the computational resources available. Also there isn't a common convergence point when the RVE edge length data in Figure 2-12 is normalised with respect to fibre length. This makes it difficult to establish how large the RVE size would need to be in order to have confidence from just one realisation. What is clear however, is that the convergence point due to the variation is generally higher than that of the effective properties at $L/l=4$ ($L/l=9.4, 13$ and 9.6 for the 10mm, 5mm and 2.5mm fibre lengths respectively). This was previously found in [65], where L/a was approximately 3-5 when studying the convergence of the variation, compared with 1-2 for the convergence of the effective stiffness. Larger models are therefore required, in order to be confident that the average effective properties are statistically representative. According to Figure 2-12, only two of the filled data are beyond the respective convergence point. RVEs with edge lengths of 50mm and 80mm for the 2.5mm fibre length are beyond the $L=24$ mm critical threshold. The coefficient of variation for these data points is still non zero however, since the relative error for the stopping criterion is 5%. The convergence point of the variation will occur at larger RVE edge lengths if greater levels of statistical confidence are required, i.e. $\epsilon_{rel} < 5\%$.

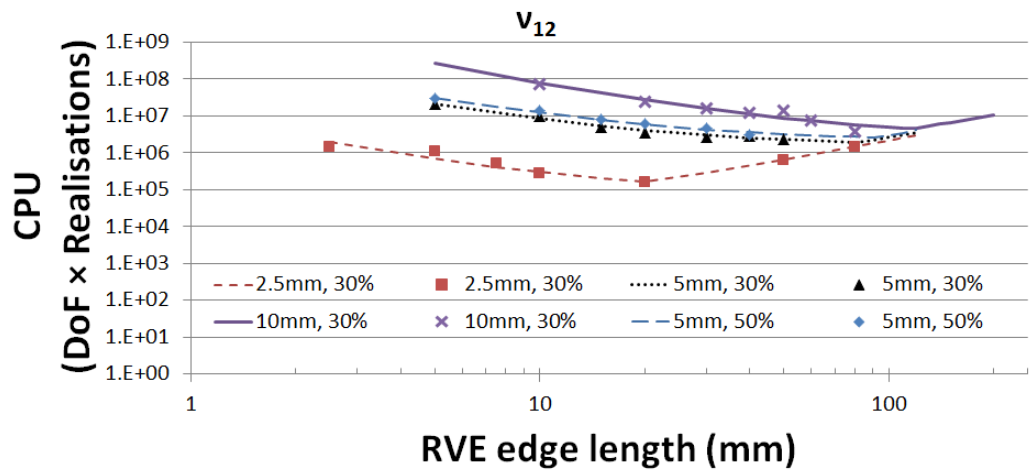
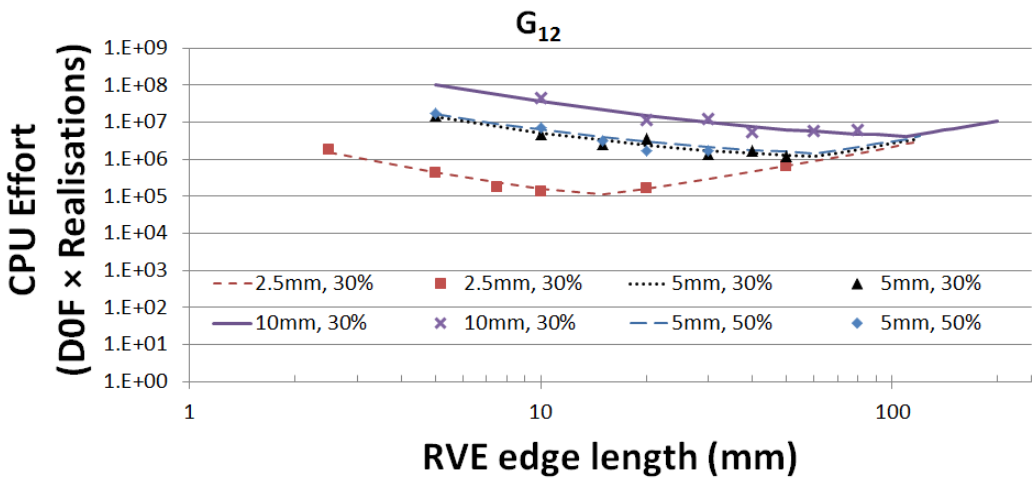
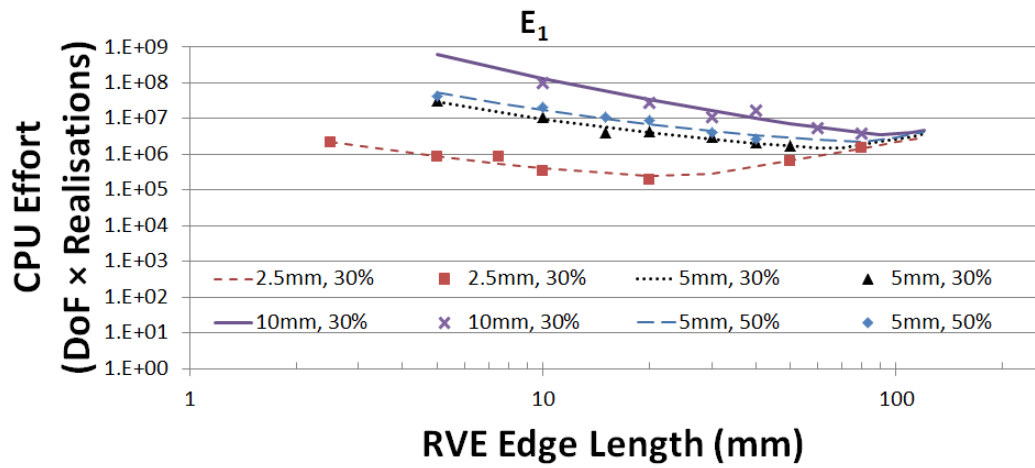


Figure 2-12: Effect of RVE size on CPU effort to determine E_1 , G_{12} and ν_{12} (expressed in terms of degrees of freedom multiplied by the number of realisations) at a target relative error of 5%. Data points represent simulation averages and lines are power-law fits. Note logarithmic scales.

2.4 Conclusions

An approach has been presented which enables large finite element models of discontinuous fibre architectures to be created, in order to predict the elastic stress/strain response. The model is capable of capturing the heterogeneity caused by local variations in fibre areal mass, and has been used to determine critical RVE sizes for random carbon fibre composites with increasing fibre lengths and fibre volume fractions.

An embedded cell approach has been adopted, whereby the RVE under consideration was embedded into a tertiary material and the effective material properties were extracted from the inner region. A critical decay length was found to exist, over which the effect of incorrectly prescribed boundary conditions applied to the outer boundary of the model became insignificant. This critical decay length was found to be 2 times the fibre length in all cases.

The critical RVE size was determined using two convergence approaches. Firstly, convergence of the effective mean values for E_1 , E_2 and G_{12} suggested that the critical RVE edge lengths were 4 times the fibre length, irrespective of the fibre volume fraction. The average Poisson's ratios ν_{12} and ν_{21} were largely independent of the RVE length scale.

Secondly, the convergence of the variation was studied in order to establish the most efficient way of computing a representative average set of elastic constants. The effect of the variation was manifested in the calculation of CPU effort, which was a function of number of realisations and degrees of freedom. The convergence point for CPU effort in terms of RVE edge length was much greater than that of the mean properties, and occurred when the number of realisations was equal to unity. This study confirmed that it is computationally more efficient to test fewer larger models than many smaller models, in order to achieve the same level of statistical confidence in the mean. The difficulty is in determining the size of the RVE required to achieve the desired level of confidence for just one realisation, since there is no clear relationship between the RVE edge length and the fibre length at the critical threshold.

In structural design, size effects should always be considered to ensure that representative material properties are achieved for the chosen fibre architecture. Deterministic size effects should be avoided as the material properties become unpredictable, but statistical size effects will always exist for a heterogeneous material and are a useful measure of the design reliability. It is important to note that the current work only considers size effects for the tensile stiffness of discontinuous fibre composites, while other mechanical properties might be affected to a different extent. For real structures, the material could experience different size effects depending on in-service loads, and critical RVE sizes determined using the current methodology might not always apply. Nevertheless, the FE model developed in this chapter provides an effective way of predicting the elastic properties of discontinuous fibre composites, as an alternative to conventional mechanical testing. A DCFP material database will be established in Chapter 4 and Chapter 5 using the current model, where the predicted elastic properties will be used to determine the fibre architecture for optimised structures.

Table 2-2: Critical RVE size as a function of fibre length and fibre volume fraction. Results are presented for two methods 1) convergence of effective properties, 2) convergence of CPU effort. L is RVE edge length and l is fibre length.

Architecture		Effective Properties						CPU Effort (Degrees of Freedom \times Realisations)					
Fibre length (mm)	v_f (%)	E_1		G_{12}		ν_{12}		E_1		G_{12}		ν_{12}	
		L (mm)	L/l	L (mm)	L/l	L (mm)	L/l	L (mm)	L/l	L (mm)	L/l	L (mm)	L/l
2.5	30	10	4	10	4	-	-	24	9.6	14	5.6	20	8
5	30	20	4	20	4	-	-	68	13.6	59	11.8	81	16.2
10	30	40	4	40	4	-	-	94	9.4	110	11	120	12
5	50	20	4	20	4	-	-	82	16.4	62	12.4	92	18.4

Table 2-3: Constants for Equation 2-27 and Equation 2-28 for coarseness, departure from isotropy and a range of elastic constants as a function of fibre architecture. R^2 values indicate the goodness of fit.

Architecture	Coarseness (Λ)			Dep from Isotropy (Δ)			E_1			G_{12}			ν_{12}		
	k	α	R^2	k	β	R^2	k	γ	R^2	k	γ	R^2	k	γ	R^2
2.5m, 30%	1.09	1.01	0.99	0.38	1.39	0.94	2472	0.95	0.99	850	1.13	0.99	0.23	1.11	0.96
5mm, 30%	1.14	0.84	0.99	2.53	1.02	0.99	20006	1.08	1.00	3904	0.99	0.98	0.57	0.95	0.9
10mm, 30%	1.25	0.80	0.95	5.99	1.12	0.92	62277	1.14	0.93	7454	0.91	0.96	1.36	1.06	0.97
50mm, 30%	1.16	0.63	0.99	-	-	-	-	-	-	-	-	-	-	-	-
5mm, 50%	1.15	0.95	0.99	2.32	0.94	0.99	42355	1.11	0.99	6515	0.96	0.98	0.65	0.96	1.00

Chapter 3. Damage tolerance of discontinuous fibre composites

Metallic materials and textile composites commonly suffer from notch sensitivity, where a reduction in strength is observed with the presence of notches. Understanding the notched performance of the material is important in structural designs where holes are needed for jointing, or when geometrical discontinuities cannot be avoided. Existing notch sensitivity studies often try to understand the influence of notch size, but the size effects associated with discontinuous fibre composites have not been considered in conjunction with the notched behaviour. The aim of this chapter is to investigate the notched tensile performance of discontinuous carbon fibre/epoxy DCFP material, using two studies to evaluate the onset of notch sensitivity. The first study investigates the influence of using a constant specimen width with increasing hole size, while the second studies the influence of using a constant hole-to-width ratio for increasing widths. Notch sensitivities have been evaluated using the strength of un-notched specimens as benchmarks, taken from the same plaques. Fracture models have been evaluated and are used to predict the notched strength of different specimen geometries. Digital Image Correlation (DIC) techniques have been applied to measure the full-field strain response for tested specimens. Strain distribution and strain concentration effects have been estimated from the DIC analysis and have been compared against analytical fracture models to predict notched ultimate tensile strength (UTS).

3.1 Background

3.1.1 Notch sensitivity of discontinuous materials

Notch sensitivity is of particular importance for closure panels because they are often fastened to the main body-in-white using bolts, or contain features which act as discontinuities in the panel. The notch sensitivity of

discontinuous fibre materials is generally considered to be poor because of small damage zone characteristics and poor crack bridging capabilities [35] compared with a continuous fibre system, as the crack path circumvents the fibres as it develops along the fibre-matrix interface.

From the many conflicting arguments in the literature it is clear that in general, the notch sensitivity of discontinuous fibre materials is poorly understood. No testing standard has been developed and consequently various geometries have been adopted. Moreover, the definition of the onset of "notch sensitivity" is ill-defined. For homogeneous materials, the presence of a notch typically leads to localised failure and a definite reduction in strength compared with an un-notched counterpart. Furthermore, sensitivity to notches for discontinuous fibre composites can be clouded by the heterogeneous nature of the material. Variations in tensile strength have been reported to be as high as 44% for some DCFP architecture [57], which can make it difficult to establish trends.

No conclusive trend has emerged from the literature to suggest that there is a relationship between reinforcement length, notch size and the onset of notch sensitivity. Hitchen *et al.* [101] found that the strength reduction of random carbon fibre laminates was independent of fibre length (1, 5, 15mm), but dependent on the notch curvature/diameter ($\text{\O}1$ -10mm). Random materials with long (25mm) or continuous (CFRM) fibres exhibited a low sensitivity to notches for notch diameters in the range of 2-15mm [35, 102]. Agarwal and Giare [103] reported that short glass fibre (50mm average length) reinforced specimens were sensitive to cracks. Toll and Aronsson [104] studied the influence of both crack and circular holes on injection moulded long- and short-fibre composites, and discovered that these material types were more sensitive to cracks than holes. Producing repeatable consistent cracks for experimental specimens is difficult to achieve however, so a central circular hole is often preferred. Mallick [102] reported a marked reduction in strength for SMC-R50, when a larger hole (9.52mm vs. 6.35mm) was present, indicating that the notch sensitivity of this material was likely to increase with hole size.

Whilst the above investigations all recorded failures at the notch, the level of strength reduction were remarkably different, and only notch sizes up to 13mm were targeted. Lindhagen and Berglund [36] discovered that all specimens were found to be notch sensitive when larger hole diameters were used (15-60mm) for short glass fibre based composites. This is supported by an analytical model for glass mat thermoplastics [36], which suggests that the onset of notch sensitivity occurs at much larger hole sizes than previously tested, in the order of 30-140mm. Lindhagen and Berglund went on to propose a baseline for the "onset of notch sensitivity", which was arbitrarily set to 85% of the un-notched strength.

Recently, Feraboli et al. [105] found that prepreg-based discontinuous carbon fibre/epoxy composites were virtually notch insensitive, with several specimens failing away from the hole. The reason was considered to be the heterogeneous nature of the meso-structure, and an "inherent material" stress concentration factor was derived to explain this phenomenon. In their latest paper [96], defect and damage analysis was performed on the same material type using ultrasonic inspection, in order to assess the correlation between macro-structural defects and failure position. However, the study proved to be inconclusive because there was no way of identifying the cause of each defect and final failure did not necessarily occur within the proximity of the 'hot spots'.

Whilst the geometry of hole/crack has been widely studied, the effect of specimen width has been overlooked. The most widely used strategy in existing notch studies is to increase hole diameter for a constant specimen width [102, 104] However, this provides insufficient information for the many stress-based fracture models that are commonly used for predicting the notch sensitivity of these materials. Fracture criteria developed by Kim et al. [106] is dependent on hole radius as well as specimen width. Others [105],[107] have used increasing hole sizes at a constant hole-to-width ratio, but without any consideration for the specimen size effects. Wisnom [29] reports that the ultimate strength of a material may be reduced for increasing specimen

volume, as the probability of critical flaws increases. On the other hand, ultimate strength may increase if the specimen volume is not a representative average of the material architecture [49]. It is therefore considered to be important to compare the notched strength with an un-notched specimen of the same width, for all hole sizes, in order to separate the effects of notch sensitivity from composite size effects.

3.1.2 Stress Fracture Criteria

Semi-empirical fracture criteria have been widely applied to composite materials to predict strength reduction due to the presence of a notch. Modelling parameters in fracture criteria are defined as characteristics of the material system and laminate configuration therefore need to be determined experimentally for any new material. The point stress criteria (PSC) and average stress criteria (ASC) [108] are both two-parameter fracture criteria based on the un-notched tensile strength and a characteristic dimension. The PSC assumes final fracture occurs when the normal stress at some distance d_0 ahead of the hole edge reaches the un-notched strength of the laminate σ_0 . The ASC assumes that fracture occurs when the average stress at some distance a_0 ahead of the hole edge equals σ_0 . Both characteristic dimensions are considered to be material constants and therefore independent of laminate configuration or notch size.

An approximate solution for the normal stress distribution adjacent to the hole (of radius R) in an infinite width plate is derived in [109], in the form of a polynomial. This yields a relationship between the notched strength of an infinite plate σ_N^∞ and σ_0 , which is expressed as

$$\frac{\sigma_N^\infty}{\sigma_0} = \frac{2}{[2 + \xi_1^2 + 3\xi_1^4 - (K_T^\infty - 3)(5\xi_1^6 - 7\xi_1^8)]} \quad \text{Equation 3-1}$$

for PSC, and

$$\frac{\sigma_N^\infty}{\sigma_0} = \frac{2}{(1 + \xi_2)[2 + \xi_2^2 + (K_T^\infty - 3)\xi_2^6]} \quad \text{Equation 3-2}$$

for ASC, where $\xi_1=R/(R+d_0)$ and $\xi_2=R/(R+a_0)$.

For isotropic laminates, the stress concentration factor for an infinite plate $K_T^\infty = 3$ [110].

It was reported in [37] that the assumption of a constant d_0 in the PSC model (i.e. independent of notch size) is invalid. The PSC model has been extended to three parameters by assuming that the characteristic dimension d_0 is in the form of an exponential function, which consists of a notch sensitivity factor C and an exponential parameter m . Pipes et al. [111, 112] developed the PWG (Pipes, Wetherhold and Gillespie) model in which the characteristic length is a function of hole radius R :

$$d_0 = C^{-1}(R/R_0)^m \quad \text{Equation 3-3}$$

R_0 is the so-called reference radius, which typically takes the value of 1. According to the PWG model, the value of K_T^∞ should remain constant for each laminate considered; hence the method has general applicability to macroscopically quasi-isotropic laminates. Kim et al. [106] considered the possibility of varying the notch sensitivity factor C with R_0 , but no comparison of notch sensitivity can be made according to specimen width (W) from the PWG model, therefore it was proposed that

$$d_0 = C^{-1}(2R/W)^m \quad \text{Equation 3-4}$$

A linear function for the characteristic dimension was proposed by Potti et al [113, 114], which was developed from the two-parameter fracture criterion typically used for metallic materials, such that

$$K_{Q^\infty} = K_F [1 - m(\sigma_N^\infty / \sigma_0)] \quad \text{Equation 3-5}$$

in which $K_{Q^\infty} = \sigma_0 \sqrt{2\pi d_0}$ for PSC, and $K_{Q^\infty} = \sigma_0 \sqrt{\pi a_0 / 2}$ for ASC.

Since the notched strength of an infinite width plate σ_N^∞ is required in all of the above models, a finite width correction factor (FWC) is generally applied to scale the experimental data σ_N to σ_N^∞ . Tan [110] derived the

closed-form solution for the FWC for an isotropic plate containing a circular hole:

$$K_{T^{\infty}}/K_T = [2-(2a/W)^2-(2a/w)^4]/2 \quad \text{Equation 3-6}$$

Applications of stress failure criteria are often found in continuous fibre composite materials containing woven textiles [107, 113, 115], which show good agreement (within 9.06%) between prediction and experimental data. However, further improvements (predictions within 2.22%) can be achieved by evaluating the characteristic dimension as described in the modified models.

Modified PSC models have been applied to long and short-fibre [104, 116] reinforced polyamide and the error between predictions and experimental data was found to reduce from 22.6% to 2.7% when introducing the linear function for the characteristic dimension from Equation 3-5. Feraboli et al. [105] applied the PSC model to predict the notched strength of prepreg-based discontinuous fibre composites. A combination of gross/net section specimen failures were observed, but only data from net-section failures was considered to be appropriate for the model. Although reasonable predictions were achieved with the PSC model (within 10%), experimental results showed notched strength for the smallest hole (0.125in) was greater than un-notched strength, which could not be considered using the model.

3.2 Results

The current work consists of two studies: effects of hole diameter for constant specimen width, and the specimen size effects for constant hole-to-width ratios. A ratio of 3/8 was selected according to the methodology outlined by Lindhagen and Berglund [36]. NCF is used for comparison of the notched behaviour. For constant width study, un-notched benchmark specimens have the same width with the notched specimens, while for constant hole-to-width ratio study, un-notched

specimens were tested for each notched specimen width. A fibre length of 30mm was adopted in both studies and the target fibre v_f was 40%. The target specimen thickness was 2.5mm, but small variations existed due an error in the tool cavity height. All specimens were straight sided and 250mm long. Specimen widths and corresponding hole sizes are listed in Table 3-1 for both materials. DIC is also used in order to capture the strain distribution on notched specimens. Detailed experimental procedures can be found in Appendix C.

Table 3-1 Summary of specimen widths and corresponding hole sizes

Constant Hole to width Ratio		Constant width	
Specimen Width (mm)	Hole Diameter (mm)	Specimen Width (mm)	Hole Diameter (mm)
12.5	4.7	37.5	3
24	9.4	37.5	5
37.5	14	37.5	7
50	18.75	37.5	9
		37.5	14

3.2.1 Size effect of un-notched specimens

Un-notched tensile specimens for both DCFP and NCF materials exhibited a brittle failure mode. Figure 3-1 shows examples of the typical linear-elastic stress-strain relationships up to final fracture. Initial failure of the NCF specimens was triggered by fibre/matrix debonding in the 90° ply at approximately 0.6% global strain, followed by the $\pm 45^\circ$ plies at 0.8% strain. Final failure occurred due to fibre fracture in the 0° ply, at a strain level of around 1.3%. DCFP specimens failed due to a combination of fibre fracture, fibre pull-out and fibre/matrix debonding, which progressively occurred during each test. Acoustic emission started at around 0.2% strain and continued until final failure at between 0.5% and 0.8% strain. The final failure strain of the DCFP specimens was at a similar level to the failure of the off-axis plies in the NCF specimens. In general, the average modulus of the DCFP material is comparable to the NCF material at ~ 32 GPa, but the DCFP strength is limited to approximately 60% of the strength of the NCF due to the lack of on-axis continuous fibres. The variations in modulus and UTS for DCFP are also

greater (~24.49% and ~31.85% respectively) than for NCF specimens (~6.9% and ~10.1% respectively).

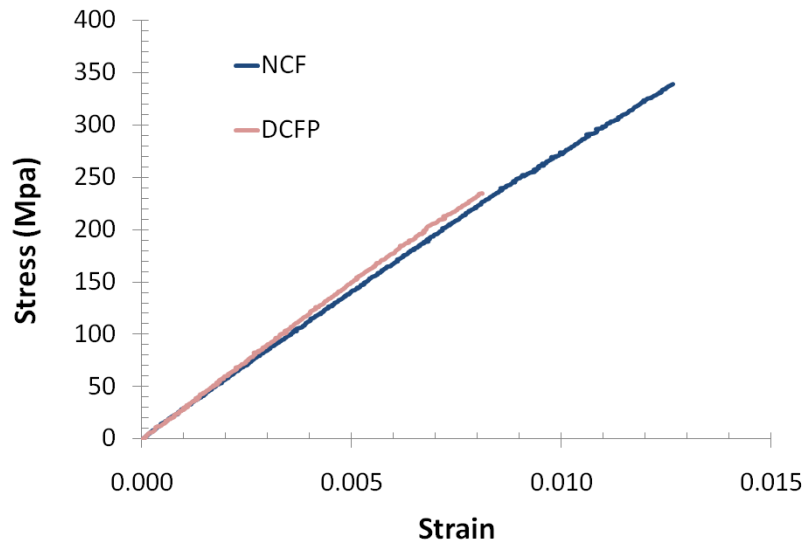


Figure 3-1 Typical stress-strain curves for un-notched NCF and DCFP specimens (both 25mm gauge width).

Modulus and UTS values are summarised in Table C-3 and plotted in Figure 3-2 for specimens of increasing width. Different trends are observed for increasing width for both NCF and DCFP. For NCF specimens, there is an 8.3% increase in modulus as specimen width increases from 12.5mm to 25mm, and 8.6% from 37.5mm to 50mm. The UTS for NCF specimens increases by 12.3% from 12.5mm to 25mm, but no measurable increase was observed between 25mm and 50mm. The width of the 12.5mm specimens is similar to the width of a single 12K tow and therefore a complete unit cell is not always captured. This problem is exaggerated by minor fibre misalignment, as a single continuous tow does not lie between the grips of the testing machine. It is also interesting to note that the variation in UTS for the NCF decreases (10%-3.74%) with increasing specimen width (25-50mm), indicating that a greater level of confidence can be achieved for wider specimens.

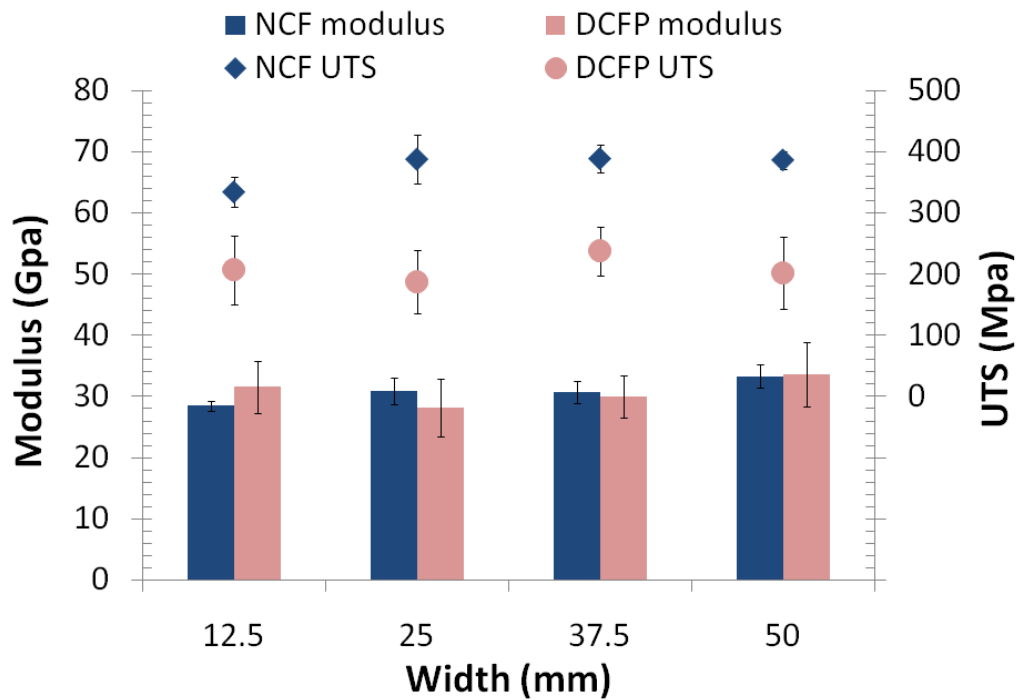


Figure 3-2 Variation of Modulus and UTS with specimen width

For DCFP specimens, there is a definite increase (19.2%) in modulus for specimen widths increasing from 25mm to 50mm. It is difficult to distinguish a trend at the 12.5mm width because of high levels of scatter (14%), resulting from the specimens being narrower than half of the chopped fibre length (30mm). The effect of increasing specimen width on the UTS of DCFP specimens is swamped by the high levels of scatter in the experimental results (up to 17%). UTS variation for DCFP is almost twice the level quoted for the NCF material, due to the random fibre architecture. Linear regression indicates that there is a marginal increasing trend between increasing specimen width and UTS, but the Pearson Correlation Coefficient of 0.04 provides little confidence in this trend.

According to Chapter 2, the critical RVE size for 30mm fibre length is approx. 120mm. However in this study, the specimen width was limited to 50mm due to the size constraint of the testing equipment. As a result, the modulus data obtained here were affected by a deterministic size effect. Although a trend of modulus reduction with increased specimen

width was expected according to Chapter 2, the disagreement in experimental results could be explained by the large variation in modulus when dominated by deterministic size effects. While specimen stiffness represents the average properties of the volume between the two jaws, specimen strength is dominated by the weakest point. Therefore, it could be expected that the strength is less affected by size effects than modulus. Nevertheless, there is an increased probability for the presence of defects as the specimen size increases, it is therefore considered to be important to compare the notched strength with an un-notched specimen of the same width, for all hole sizes, in order to separate the effects of notch sensitivity from composite size effects.

3.2.2 Constant width study for notched specimens

In advanced composite design, the common approach to computing the open-holed tensile strength is to use the gross-sectional area, since it is independent of notch geometry. However, for large notches this method can lead to over conservative safety factors, since the reduction in cross sectional area is not taken into consideration. The net strength however, is commonly used to establish notch sensitivity. Average notched gross- and net-section strength have been calculated for each specimen width and are summarised in Table C-4, Figure 3-3 and Figure 3-4.

Notched specimens also failed in a brittle manner, but the position of the final fracture surface varied between materials and hole sizes. For NCF specimens, the presence of the hole caused localised failure within the net section for all hole diameters (see Figure 3-5), whereas a variety of either gross or net section failures was observed for the DCFP material depending on the hole size.

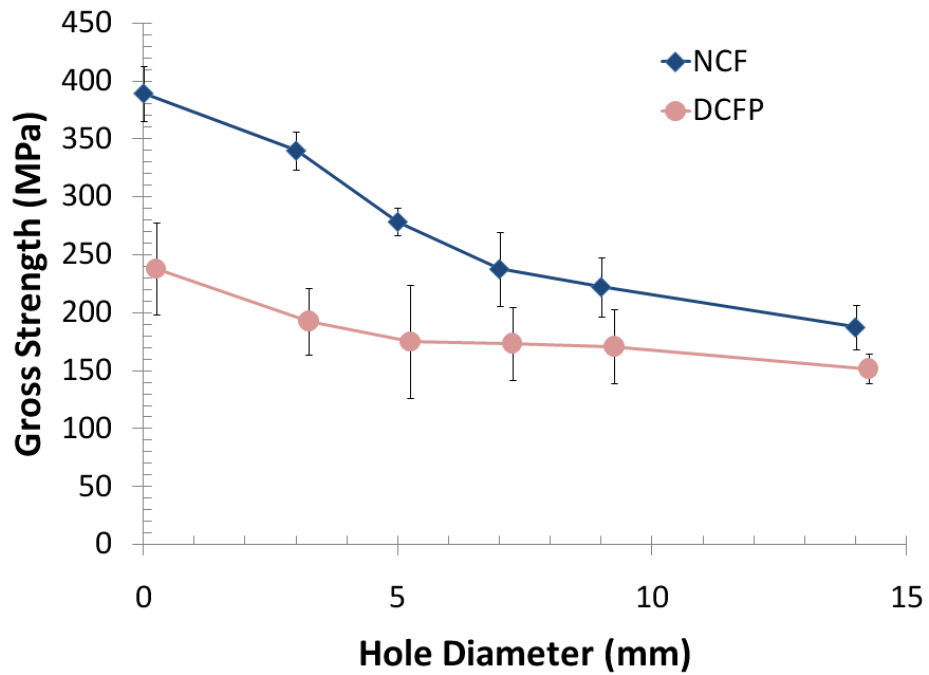


Figure 3-3 Gross section strength for constant width study specimens. Horizontal axis values are offset by 0.25mm to clarify data.

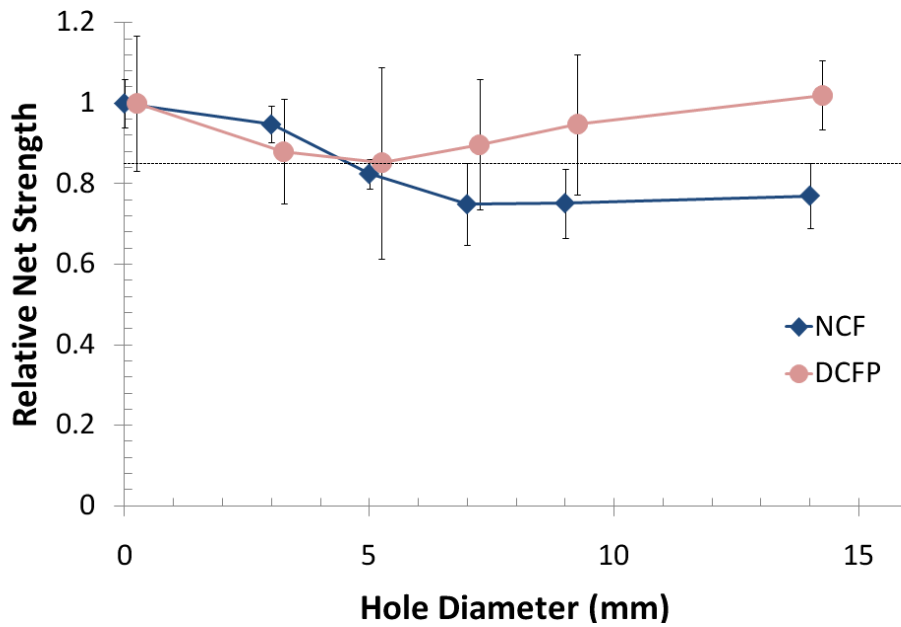


Figure 3-4 Relative net section strength for constant width study specimens. Dotted line represents 85% strength retention threshold. Horizontal axis values are offset by 0.25mm to clarify data.

Data presented in Figure 3-3 and Figure 3-4 indicates that the tensile strength of the NCF material is sensitive to the presence of circular notches. Figure 3-3 shows that the gross strength is reduced by the presence of increasing hole sizes. A 52% reduction in gross tensile strength (389MPa to 187MPa) is observed for a notch diameter of 14mm compared with the unnotched NCF benchmark. The relative net strength values presented in Figure 3-4 indicate that NCF specimens were sensitive to hole diameters greater than $\varnothing 5\text{mm}$, according to the 85% threshold proposed in [36]. The relative net strength is reduced from 0.95 to 0.75 from $\varnothing 3\text{mm}$ to $\varnothing 7\text{mm}$, but no further reduction was observed as the hole size increased to $\varnothing 14\text{mm}$. This critical hole size will be influenced by the size of the unit cell (a function of tow size) and is therefore only applicable to the current data set.



Figure 3-5 Examples of tested notched specimens (37.5mm wide, $\varnothing 9\text{mm}$ hole). (a) NCF with net-section failure; (b) DCFP with net-section failure; (c) DCFP with gross-section failure.

The position of the failure zone for DCFP specimens is a function of notch size, as indicated by the number of net vs. gross failures in Table C-4. All DCFP specimens with a $\varnothing 3\text{mm}$ hole failed within the gross section. The number of net section failures increased as the hole diameter increased from $\varnothing 5\text{mm}$ to $\varnothing 9\text{mm}$. All specimens with a $\varnothing 14\text{mm}$ hole failed in the net section at the edge of the hole (refer to Figure 3-5). Gross section failure is uncommon for isotropic materials, as failures are typically caused by

the geometrical stress concentration at the root of the notch. The heterogeneous macro-structure of the DCFP material causes large stress concentrations to form at the bundle ends, due to the large disparity in stiffness between the epoxy and carbon fibre and the coincident positions of filament ends [117]. These 'material stress concentrations' are often larger than the 'geometrical stress concentration' and can therefore be responsible for initiating failure away from the notch. Figure 3-6 shows a comparison of the strain distribution in NCF and DCFP 37.5mm wide specimens with $\varnothing 5$ mm holes. For NCF, major strain concentrations appear around the hole in a cross pattern, which are influenced by the strain concentration at the fibre-matrix interface in the $\pm 45^\circ$ plies. For the DCFP sample, strain concentrations not only occur around the hole but also randomly within the gross-section, due to the heterogeneity of the material. For smaller hole-to-width ratios, these strain concentrations exceed the geometric strain concentrations at the notch, causing failure in the gross-section.

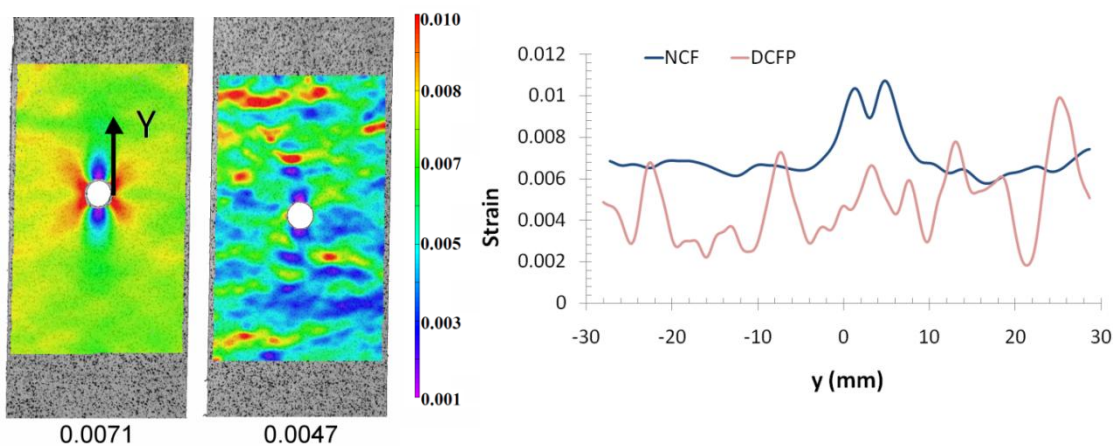


Figure 3-6 Example of NCF (left) and DCFP (right) full-field strain distributions for a 37.5mm wide/ $\varnothing 5$ mm hole. Values indicate global strain. Graph shows strain distribution along a line in the direction of y, centred about the right hand edge of the hole.

Figure 3-7 shows the strain history for a DCFP specimen which has failed within the gross section. As the global strain increases from 0.1% to 0.2%, noticeable strain concentrations develop around the hole and at the top of the gauge area. Between 0.4% and 0.55% global strain, a

number of these major strain concentrations coalesce in the gross section, causing a sudden catastrophic failure at 0.58%. Post failure inspection of the sample indicated that a resin rich region in the vicinity of an isolated fibre bundle was the cause of the larger strain concentration in the gross section. Cracks developed in the resin region, meeting the boundary of an off-axis fibre (85° from vertical). The crack propagated along the interface of the fibre, which can be seen on the left hand side of the failure zone in Figure 3-7.

It should be noted that there is still the possibility of a net-section failure occurring for DCFP specimens with small hole sizes, since failure occurs randomly along the gauge length at the weakest point. The material strain concentration may coincide with the notch, which makes it difficult to determine the dominant cause of failure for small hole sizes directly from the position of the fracture site.

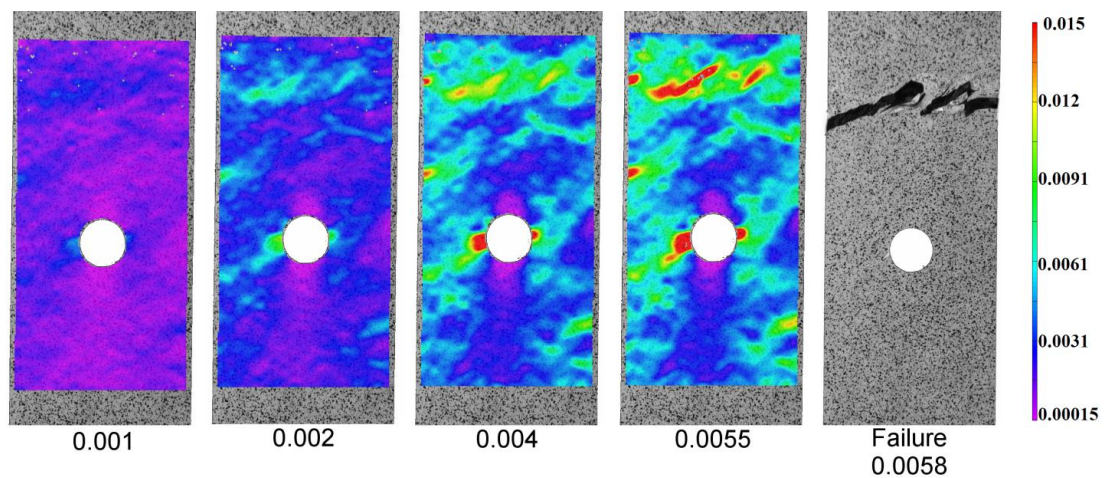


Figure 3-7 Example of strain plot for a 37.5mm/Ø9mm specimen. Global strain values shown.

Data presented in Figure 3-3 and Figure 3-4 indicates that the DCFP material is notch insensitive. A 36% reduction in gross tensile strength (238MPa to 151MPa) is observed for a Ø14mm notch, compared with the un-notched DCFP benchmark. However, according to the Figure 3-2, the UTS of the 37.5mm wide un-notched benchmark is higher than any of

the other specimen width, giving rise to this large gross strength reduction. This is supported by the fact that only a 14% reduction in gross strength is observed between $\varnothing 7\text{mm}$ and 14mm for DCFP. Although the UTS of DCFP is approximately 60% of NCF, the presence of a circular notch reduces this deficit. The gross strength of DCFP is only 20% lower than NCF when a $\varnothing 14\text{mm}$ hole is present in a 37.5mm wide specimen, which means that the disadvantage of low strength of DCFP is greatly reduced due to its notch-insensitivity.

The relative net strength presented in Figure 3-4 indicates that DCFP specimens were insensitive to all notch diameters, as all data points are above the 85% strength retention threshold. There is an initial 12% reduction in net strength between the benchmark and the $\varnothing 3\text{mm}$ hole size. This may be attributed to the superficially high UTS of the benchmark, but also due to the large number of gross section failures for small hole sizes. All $\varnothing 3\text{mm}$ specimens failed in the gross section, implying that the material stress concentration was greater than the geometric stress concentration for this batch of samples. Consequently, the reduction in net strength for small hole sizes can be attributed to the heterogeneity of the material in this case, which is supported by the high error bars in Figure 3-4. Further support is that the strength of the notched specimens tends towards the un-notched benchmark, as the hole size increases and consequently the percentage of net-section failures increases. The net strength of the $\varnothing 14\text{mm}$ specimen is 242MPa compared with 238MPa of the un-notched benchmark.

3.2.3 Constant hole-to-width ratio study for notched specimens

A hole-to-width ratio of $3/8$ was selected according to [36], which was also common to the $\varnothing 14\text{mm}$ hole/ 37.5mm wide specimens studied in the constant width study above. All specimens at this constant ratio failed within the net section, regardless of the material type. Clearly a critical hole-to-width ratio exists beyond which the geometrical stress concentration dominates, causing failure to always occur at the notch.

Notched gross and net section strength are summarised in Table C-5. The gross section strength is plotted in Figure 3-8 and the relative net section strength is plotted in Figure 3-9, using the un-notched strengths of specimens at the same corresponding widths as benchmarks.

In general, the NCF is demonstrated to be notch-sensitive, supporting the results in the constant width study. A clear reduction in gross strength is evident in Figure 3-8 and the straightforward trend observed in the unit width study (Figure 3-2) yields a clearly distinguishable trend for the relative net strength in Figure 3-9. The relative net strength crosses the 85% retention threshold between a hole diameter of $\varnothing 4.7\text{mm}$ and $\varnothing 9.4\text{mm}$. Consequently the onset of sensitivity to notches occurs at slightly larger hole diameters compared with the constant width study, but this can be attributed to the influence of the specimen size effects which are taken into consideration with the current method. The un-notched 12.5mm wide NCF specimen has a UTS of just 334MPa, compared with approximately 388MPa for the other widths tested. If 388MPa is used as the benchmark for the $\varnothing 4.7\text{mm}/12.5\text{mm}$ wide specimen then the specimen crosses the 85% threshold at approximately $\varnothing 5\text{mm}$. The constant width study therefore under-predicts the onset of notch sensitivity, since it neglects specimen size effects. Beyond the onset of notch sensitivity, the relative net strength plateaus at a value of ~ 0.75 for large ($< \varnothing 14\text{mm}$) hole sizes, using both methods.

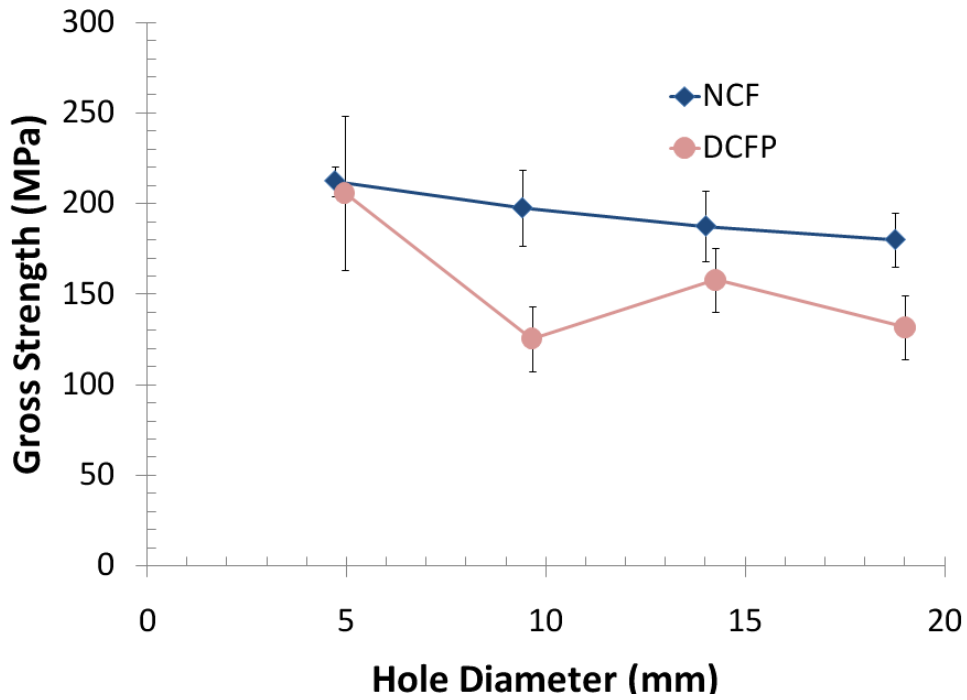


Figure 3-8 Gross section strength for constant ratio study specimens. Horizontal axis values are offset by 0.25mm to clarify data.

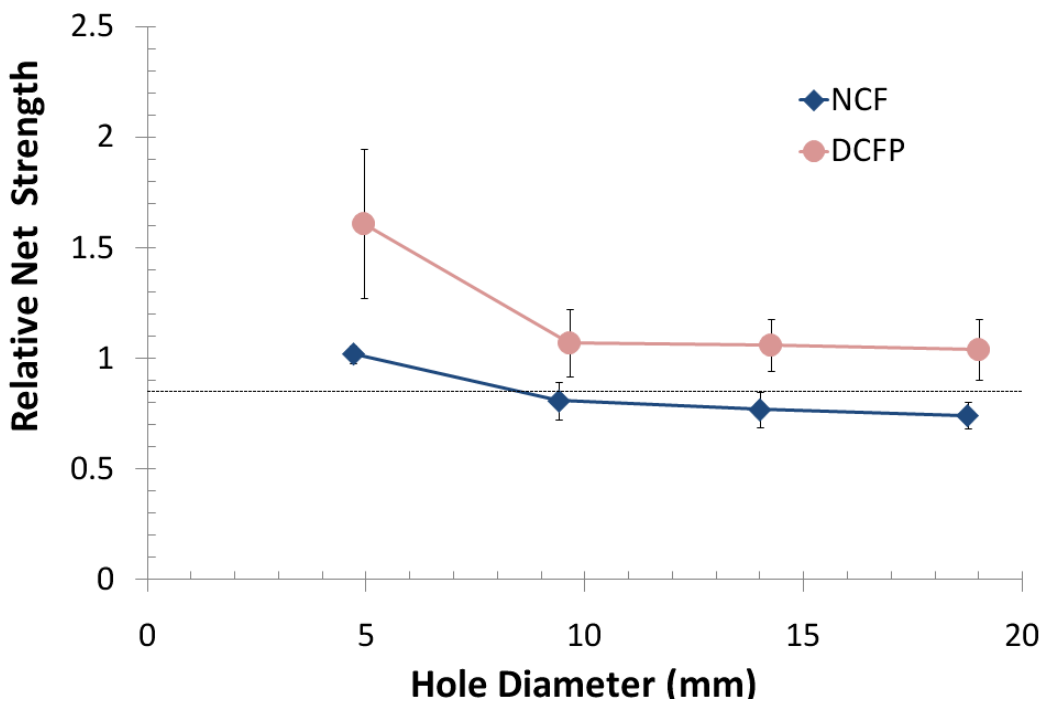


Figure 3-9 Relative net section strength for constant ratio study specimens. Dotted horizontal line represents 85% strength retention threshold. Horizontal axis values are offset by 0.25mm to clarify data.

From Figure 3-8 it is not immediately clear if DCFP is notch sensitive when testing constant ratio specimens. The gross strength versus hole diameter follows a similar trend to the unit width study presented in Figure 3-2. Specimens with a $\varnothing 5\text{mm}$ hole are only 12.5mm wide and therefore susceptible to strength variation. It is unlikely that the average notched strength from only 6 test repeats is representative for this narrow specimen width. This is evident when the notched strength of the 12.5mm wide DCFP specimen is compared with the NCF counterpart. The average notched strength for DCFP is within 97% of the notched strength for NCF at $\varnothing 4.7\text{mm}/12.5\text{mm}$ wide and the COV is over 20%, which implies that the DCFP data point is superficially high. It is likely that the local fibre volume fraction is higher for these samples than the global volume fraction of 40%.

The relative net strength in Figure 3-9 however, clearly shows that DCFP is notch insensitive when using a constant hole-to-width ratio approach. None of the data points fall below the 85% critical threshold. Apart from the first data point, which is seemingly high, the other hole sizes exhibit a relative net strength of approximately 1.00. This correlates well with the constant width study, particularly for those specimens that failed exclusively in the net section.

3.2.4 Fracture criteria

Fracture models were only applied to data from the constant width study, since size effects were observed for both NCF and DCFP. In order to achieve higher confidence, gross section failures were omitted and at least 3 specimen repeats were used for the net section failures. DCFP specimens with $\varnothing 3\text{mm}$ and $\varnothing 5\text{mm}$ holes were omitted. The characteristic dimension is the most significant parameter in all of the failure criteria studied. Digital image correlation has been applied to assess the validity of the fracture models, by obtaining the stress distribution across the ligament ($\frac{1}{2}[w-D]$). Figure 3-10 shows the stress distribution as a function of distance from the edge of the hole for 37.5mm/ $\varnothing 14\text{mm}$ specimens. The theoretical solution is included for comparison, which has been calculated from the normal stress distribution for an isotropic

material [109], corrected for a finite width plate using Equation 3-6 [110]. The strain resolution at the root of the notch is limited because of the Vic3D[®] software, so it was not always possible to capture the strain at the edge of the hole. However as Figure 3-10 shows, the experimental curves generally follow the theoretical solution, which supports the assumption of using isotropic failure criteria for both materials.

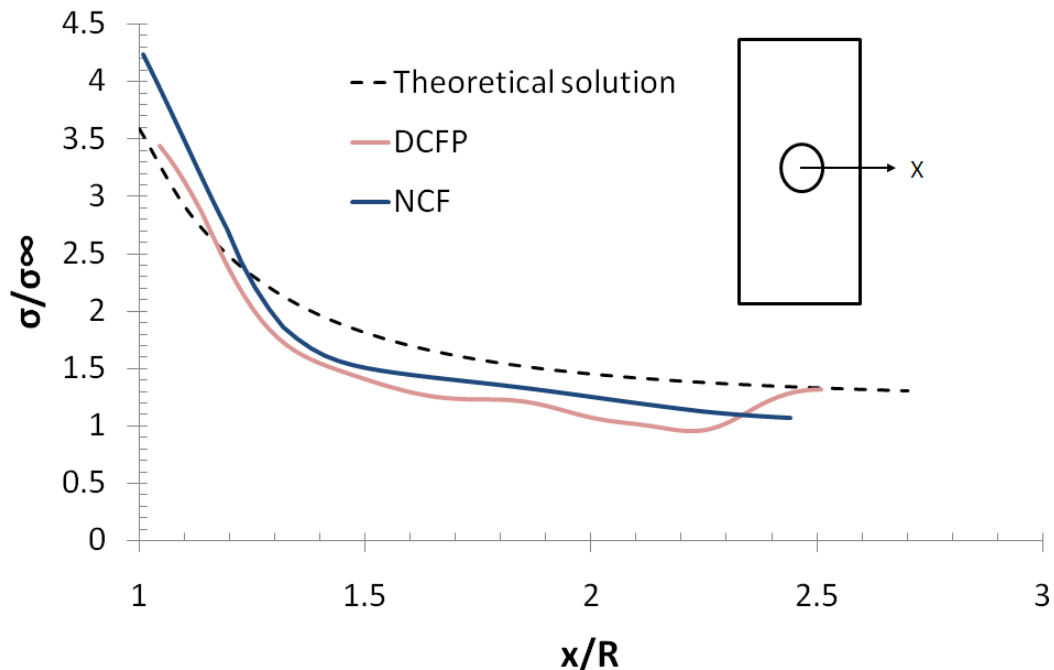


Figure 3-10 Example of X-direction relative stress distribution for 37.5mm/Ø14mm specimens. σ_{∞} denotes the remote stress applied to the specimen.

Only PSC-based models were shown to be valid for the DCFP data, since the characteristic dimension in the ASC-based models was calculated to be larger than the width of the specimen ligament, hence they were not physically representative. The modified PSC model proposed by Potti et al [113, 114], described by Equation 3-5, was also invalid because the parameters returned from the regression analysis were negative.

The characteristic dimension, d_0 , is common for each of the PSC-based models and is presented in Table C-6 for both materials. The values of d_0 generally increase with increasing hole size, which makes the modified PSC models more accurate than the original PSC model (See Table C-6

and Figure 3-11). Notch-sensitivity factors for NCF and DCFP are calculated to be 0.92 and 1.23 respectively, using Equation 3-3 from the PWG model [111, 112]. These results are not physically meaningful because DCFP was notch insensitive in practice. However, notch sensitivity factors calculated from Kim's model [106] (Equation 3-4) are 0.30 and 0.07 for NCF and DCFP respectively, indicating that NCF was more notch sensitive than DCFP. For this reason, Kim's model is considered to be the most appropriate for studying DCFP.

Comparisons between predictions and experimental results are presented in Table C-6 and Figure 3-11 for NCF and DCFP. For NCF, the maximum relative error of the original PSC model was 8.15%, compared with 3.75% and 3.72% for the PWG and Kim's model respectively. Similarly, the maximum relative error for DCFP was reduced from 10.52% to 0.69% and 0.72% for the PWG and Kim's model.

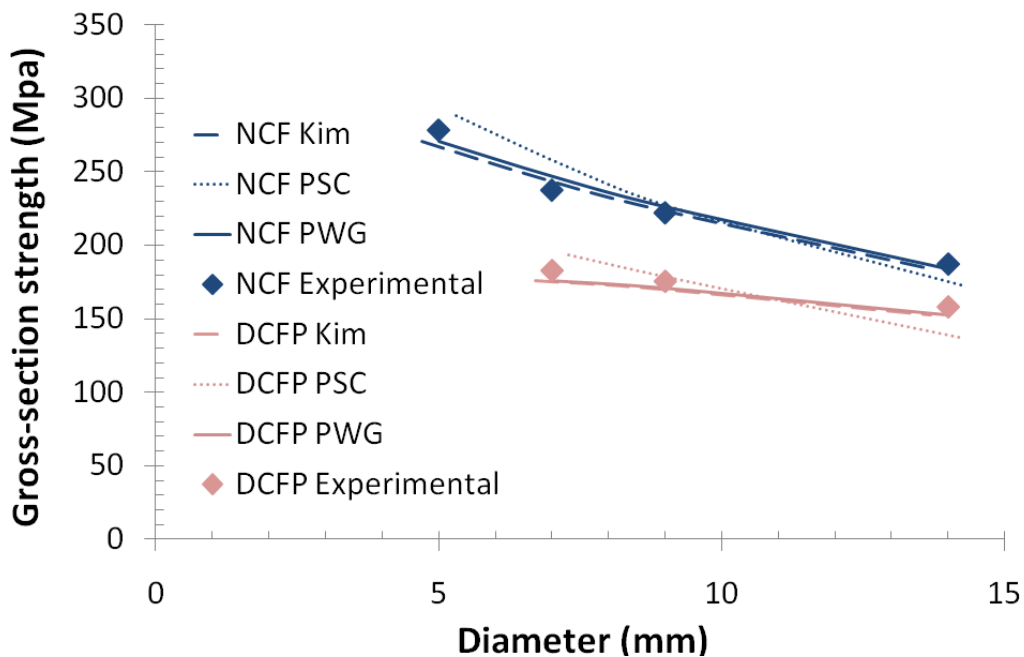


Figure 3-11 Comparison of experimental notched strength with predictions from Kim's model and Point Stress Criterion.

3.3 Conclusions

The notched tensile performance of a discontinuous carbon fibre/epoxy DCFP material has been compared against a quasi-isotropic non-crimp fabric of the same fibre volume fraction. Two studies have been completed, using different geometries to identify a reliable method to determine the onset of notch sensitivity. The first study investigated the influence of using a constant specimen width with increasing hole size, while the second study used a constant hole-to-width ratio for increasing widths.

Both methods indicate that the DCFP material is notch insensitive for the current set of material parameters studied. Failures were observed in the gross section for smaller hole sizes and the relative net strength was found to remain above the critical threshold of 85% for both geometry types. In comparison, the NCF material was found to be notch sensitive by both methods, but the onset of sensitivity to notches was different in each case. The critical hole size was determined to be approximately $\varnothing 5\text{mm}$ for the constant width study and $\varnothing 9\text{mm}$ for the constant ratio study. This discrepancy is attributed to the unit width effects of the material. The constant ratio study uses individual un-notched benchmark specimens for each width, which show clear signs of the UTS of the NCF material being sensitive to the width of the specimen.

There are clearly pros and cons for each specimen geometry set up. Specimens of constant width have been used almost exclusively in the literature, providing valuable input data for fracture-based analytical models. The constant ratio study is more time consuming, since un-notched specimens are required for each width. However, using a constant hole-to-width ratio makes it possible to isolate the effects of the internal material stress concentration from the geometrical stress concentration at the notch. This causes failure to occur at the root of the notch, generating more distinguishable trends. This method relies on the hole-to-width ratio being above a critical threshold, which is difficult to determine without prior testing. The threshold is considered to be a function of fibre length, degree of fibre orientation, tow size and fibre

volume fraction. The critical hole-to-width ratio threshold for the current DCFP material is found to be between 0.25 and 0.375.

Fracture models have been evaluated and used to predict the notched strength of specimens with increasing hole diameter but constant width. Digital Image Correlation (DIC) techniques have been applied to measure the full-field strain response for tested specimens. Strain distribution and strain concentration effects have been estimated from the DIC analysis and have been compared against analytical fracture models to predict notched ultimate tensile strength (UTS). The experimental curves generally follow the theoretical prediction, which supports the assumption of using isotropic failure criteria for both materials. Consequently, predictions for the notched tensile strength are within $\sim 1\%$ of experimental values for both materials, when adopting the modified Point Stress Criterion developed by Kim et al [106].

From a structural design point of view, although the un-notched ultimate strengths for DCFPs are lower than those of NCF, DCFPs are much less sensitive to notches. Notches are one of the major concerns in structural design, often resulting in larger safety factors to compensate for strength reductions. Consequently, the overall design strengths used for DCFP could conceivably compete with those of NCFs in the presence of notches within a full-scale structure. It is also worth noting that according to the current studies, both un-notched and notched net-section strengths of DCFP are shown to be influenced by size effects. This further supports the results from the FE model presented Chapter 2.

Chapter 4. Development of a stiffness optimisation algorithm for discontinuous fibre composite components

This chapter presents a model to optimise intelligently the fibre architecture of components manufactured from discontinuous fibre composites, taking advantage of the design freedom that these materials offer. A stiffness optimisation algorithm is adopted to derive distributions of section thickness and of constituent properties concurrently. A segmentation algorithm is developed to divide the component into zones consisting of elements with similar areal mass values. For the current model, cost, mass and cycle time can all be traded against component performance through local selection of material parameters, ensuring a minimum stiffness requirement is met. A simple geometry is used for validation, in preparation for optimising an automotive structure in Chapter 5.

4.1 Introduction

A structural optimisation problem can be described with a statement consisting of the following:

1. *The design domain*; which is the allowable volume within which the material can exist
2. *The objective function*; which is the goal of the optimisation and is to be minimised or maximised over the design domain
3. *The design variables*; which are the specifications that can be controlled by the designer. These often include the material type, composition and section thickness.
4. *The design constraints*; which are the conditions that must be satisfied for the design to be feasible. Examples include component weight, cost and limits for design variables (e.g. maximum and minimum thickness).

The optimisation process establishes mathematical relationships that link the objective function and the design constraints to the design variables. The design variables are iteratively updated according to these mathematical relationships, causing the objective function to converge towards a maximum/minimum value, whilst ensuring the design constraints remain satisfied. Compared with a conventional heuristic design route, structural optimisation provides a much better way of approaching the fully optimised design (Figure 1-4 (b)).

Topology, shape and size are commonly used terms to define the geometry of a structure. Topology refers to the overall configuration of the design domain, which determines the load paths of the structure under given loads. Shape is a subset of topology which refines the boundary of the design boundary and size is the dimensions of the geometry.

The most widely used structural optimisation methods for composite materials adopt genetic algorithms, a metaheuristic type approach [47]. These are only practical for handling discrete problems and are more widely used for optimising laminated composites where fibres are arranged in discrete plies. The lay-up design for these materials is somewhat limited by the manufacturing route, where optimisation of the local thickness is controlled by the number of plies. This approach is considered to be unsuitable for optimising DCFP, as the number of search points increases dramatically due to the design variables (local thickness and stiffness) being continuously variable.

Other methods, such as non-linear programming [45, 118], require constant re-evaluation of the design objectives and constraints, and are therefore very computationally expensive, particularly for large structures. In comparison, optimality criterion approaches [119] use simple local rules to update design variables, which are much more efficient and suitable for complex or larger problems.

Structural optimisation of meso-scale discontinuous fibre architecture composites involves a combination of continuous and discrete design

variables. The local thickness can be continuously varied across the component and is independent of the fibre architecture, whereas a continuous change of fibre length or tow size is unrealistic and therefore can only be varied in discrete regions. It is worth noting that the section stiffness of a structure is determined by its cross sectional dimensions and effective material properties, where the effective material properties for discontinuous fibre composites are a function of the fibre architecture. Therefore, the optimisation problem for DCFP can be solved in two stages: The first stage is to evaluate the optimised thickness contour of the component and the corresponding local material properties, using structural optimisation algorithms. The second stage is to determine the optimised fibre deposition strategy based on the structural optimisation results. This can be implemented using decision making methods such as weighted score and TOPSIS [120], providing the material properties database and the design preference. The spray strategy can be calculated following the optimisation and the results can be compared back to the simulation.

This chapter presents a structural optimisation algorithm to adjust local thickness and material stiffness concurrently for a DCFP component. The algorithm enables the flexibility of the DCFP process to be exploited, by creating locally varied material thickness and section property distributions. A stiffness optimality criterion is derived and the method of solving Lagrangian multipliers is adopted for each optimisation constraint, which include material volume and material cost. The local section thickness and stiffness values are updated concurrently through an iterative process.

A segmentation algorithm is employed to ensure that the fibre architectures generated by the structural optimisation routine are suitable for manufacture [12]. It is impractical for the local section thickness and material stiffness to vary continuously over the surface of the component, as the precision of the fibre deposition is controlled by the robotic spray head. Neighbouring elements with similar material properties are merged into larger zones using a common set of material

parameters (fibre length and orientation, tow size etc.), controlling the local stiffness of the zone. The size and shape of each zone are tailored to suit the fibre deposition process, so that small areas or patches with small dimensions are avoided. It is also rational that a critical zone size exists in order to achieve a representative fibre architecture, according to the results presented in Chapters 2 and 3. The size of the representative volume element for achieving a homogeneous distribution of discontinuous fibres has been shown to be a function of fibre length and volume fraction [121, 122].

The model has been demonstrated by optimising the bending performance of a flat plate with three arbitrary holes. A detailed description of the geometry is included in Appendix D, which has been adopted throughout this Chapter to explain the development of the model.

4.2 Stiffness optimality criterion

4.2.1 Problem formulation

The stiffness is often the primary issue in most structural design problems. Stiffness optimisation aims to achieve the stiffest structure whilst fulfilling all of the design constraints, so that the overall deflection of the part is minimised under the prescribed load case. The objective of maximising the structural stiffness is equivalent to minimising the total strain energy within the structure [119]. It has been proposed in [46] that, for a single load case evaluation subjected to a constant volume constraint, the total strain energy is minimised when the strain energy density distribution through the part is uniform. However, this average strain energy density criterion was derived assuming the material properties are constant. When designing a shell-like structure the local thickness is normally the only variable to be updated during a size optimisation process. The use of DCFP has introduced the local effective modulus of the material as an additional design variable, therefore a new

stiffness optimality criterion has been determined to optimise the thickness and modulus values concurrently.

With the additional stiffness design variable, a second constraint is required to determine the limits when updating the local modulus values. Restricting the material cost is a reasonable approach, since increasing the section thickness requires a larger quantity of material to be used, while increasing the modulus potentially requires increased fibre volume fraction or a smaller fibre tow size, further increasing the unit cost of the material. The mechanical performance of meso-scale discontinuous fibre composites is linked to the homogeneity of the bundle ends and the number of fibre to fibre contacts [57] and this therefore simply means that smaller, more expensive tows make stronger and stiffer components.

For a structure subjected to prescribed load and boundary conditions, the optimisation problem can be constructed as

$$\begin{aligned}
 & \min U(E, t) \\
 & \text{subject to } V(t) = V_0, C(E, t) = C_0 \\
 & \text{and } E \geq E_{min}, t \geq t_{min}
 \end{aligned}
 \tag{Equation 4-1}$$

where E and t denote the modulus and thickness design variables respectively. U denotes the total strain energy in the structure. V and C denote the overall volume and material cost of the structure, and V_0 and C_0 are the target volume and cost. E_{min} is the lower bound of the modulus, which has been taken from the literature [57], and t_{min} is the lower bound of thickness value to prevent local buckling of the structure. The minimum thickness is influenced by the lower modulus bound, since the stiffness and strength of the component change with thickness due to the homogeneity effects.

4.2.2 Stiffness optimality criterion and the Lagrangian multiplier approach

The optimisation process is performed based on the results from finite element analyses of the structure. The overall strain energy, component volume and material cost can be individually expressed as a summation of the corresponding value from each element in the part. The optimality criterion is derived by solving the Karush–Kuhn–Tucker (KKT) conditions of the Lagrangian expression. The Lagrangian expression from Equation 4-1 is

$$L = U + \lambda_1(V - V_0) + \lambda_2(C - C_0) + \lambda_3(E_{min} - E_i) + \lambda_4(t_{min} - t_i)$$

Equation 4-2

where λ_1 , λ_2 , λ_3 and λ_4 are Lagrange multipliers corresponding to each constraint. The subscript i denotes the element number. The stationary of the Lagrangian leads to the following KKT conditions:

$$\frac{\partial L}{\partial E} = \sum \frac{\partial U_i}{\partial E_i} + \lambda_2 \sum \frac{\partial C_i}{\partial E_i} + \lambda_3 = 0$$

Equation 4-3

$$\frac{\partial L}{\partial t} = \sum \frac{\partial U_i}{\partial t_i} + \lambda_1 \sum \frac{\partial V_i}{\partial t_i} + \lambda_2 \sum \frac{\partial C_i}{\partial t_i} + \lambda_4 = 0$$

Equation 4-4

If the lower bounds for modulus and thickness are inactive, then λ_3 and λ_4 are both equal to zero. It was stated in [123] that for an optimal design problem with the number of variables equal to the number of active constraints, the solution yields a fully utilised design. The stationary conditions in this case produce n constraint equations with n unknowns, and each can be solved independently of the Lagrangian multipliers. (i.e. each constraint equation is sufficient to determine one design variable). Therefore, Equation 4-3 and Equation 4-4 can be rearranged as:

$$\frac{-\sum \frac{\partial U_i}{\partial E_i}}{\lambda_2 \sum \frac{\partial C_i}{\partial E_i}} = 1 \quad \text{Equation 4-5}$$

$$\frac{-\sum \frac{\partial U_i}{\partial t_i}}{\lambda_1 \sum \frac{\partial V_i}{\partial t_i}} = 1 \quad \text{Equation 4-6}$$

The optimality criterion aims to solve Equation 4-5 and Equation 4-6 with an iterative scheme. The recurrence relations for modulus and thickness may be written as:

$$E_i^{k+1} = \left(\frac{-\frac{\partial U_i}{\partial E_i}}{\lambda_2 \frac{\partial C_i}{\partial E_i}} \right)^{\frac{1}{r}} E_i^k \quad \text{Equation 4-7}$$

$$t_i^{k+1} = \left(\frac{-\frac{\partial U_i}{\partial t_i}}{\lambda_1 \frac{\partial V_i}{\partial t_i}} \right)^{\frac{1}{n}} t_i^k \quad \text{Equation 4-8}$$

where the superscript k denotes the iteration number, and r and n are the moving limit parameters to define the step size of each iteration.

The algorithms described in Equation 4-7 and Equation 4-8 require the partial derivatives of U , V and C to be calculated for each element at each iteration. Assuming the section forces and moments applied to each element remain constant, the elemental strain energy can be written as:

$$U_i = \frac{1}{2} [d_i]^T [K_i] [d_i] = \frac{1}{2} [F_i]^T [K_i]^{-1} [F_i] \quad \text{Equation 4-9}$$

where $[d_i]$ and $[F_i]$ are the element displacement and force vectors, and $[K_i]$ is the section stiffness matrix of the i th element. Therefore, the partial derivatives of U_i are:

$$\frac{\partial U_i}{\partial E_i} = \frac{1}{2} [F_i]^T \frac{\partial [K_i]^{-1}}{\partial E_i} [F_i] \quad \text{Equation 4-10}$$

$$\frac{\partial U_i}{\partial t_i} = \frac{1}{2} [F_i]^T \frac{\partial [K_i]^{-1}}{\partial t_i} [F_i] \quad \text{Equation 4-11}$$

The elemental volume is simply a function of thickness, thus

$$\frac{\partial V_i}{\partial E_i} = 0 \quad \text{Equation 4-12}$$

$$\frac{\partial V_i}{\partial t_i} = A_i \quad \text{Equation 4-13}$$

where A_i is the area of the i th element.

The material cost model employed here assumes a basic linear relationship between the material cost and the modulus value, such that:

$$C_i = \alpha E_i A_i t_i \quad \text{Equation 4-14}$$

where the factor α can be estimated by calculating the material cost for a range of DCFP laminates with known properties. Example cost versus modulus relationships are presented in Figure 4-1, where a range of fibre tow sizes, fibre length and volume fractions are used. For each fibre type or tow size, the value of α can be determined from the gradient of the best fit (dotted) line in Figure 4-1. The current optimisation method uses a constant cost as an equality constraint, thus the evaluation of the actual cost value is unnecessary. In a more refined solution, a more extensive database of material properties and costs would be used to provide greater fidelity. The value of α is taken as unity in the current study, which denotes the ratio of the current cost to the constraint value. Therefore;

$$\frac{\partial C_i}{\partial E_i} = A_i t_i \quad \text{Equation 4-15}$$

$$\frac{\partial C_i}{\partial t_i} = E_i A_i \quad \text{Equation 4-16}$$

The values of the Lagrangian multipliers λ_1 and λ_2 need to be correctly determined such that the overall volume and cost constraints are satisfied at every iteration, i.e.

$$\sum \left(\frac{-\frac{\partial U_i}{\partial t_i}}{\lambda_1 \frac{\partial V_i}{\partial t_i}} \right)^{\frac{1}{r}} t_i^k A_i = V_0 \quad \text{Equation 4-17}$$

$$\sum \left(\frac{\frac{\partial U_i}{\partial t_i} \frac{\partial U_i}{\partial E_i}}{\lambda_1 \lambda_2 \frac{\partial C_i}{\partial E_i} \frac{\partial V_i}{\partial t_i}} \right)^{\frac{1}{n}} t_i^k A_i E_i^k = C_0 \quad \text{Equation 4-18}$$

Substituting Equation 4-10 to Equation 4-16 in to Equation 4-17 and Equation 4-18 yields a system of two non-linear equations with two unknowns λ_1 and λ_2 , where λ_1 can be determined by Equation 4-17, and the value of λ_2 , E_i^{k+1} and t_i^{k+1} can be calculated subsequently.

The design variables are also subjected to bound constraints, E_{min} and t_{min} . A reduced step size method is adopted here to prevent the updated value of each design variable exceeding its limit. If the output value at the current step falls below the lower bound when updating E_i and t_i at the k th step (using Equation 4-7 and Equation 4-8), the step size parameter (r or n) is adjusted globally until the bound limits are satisfied.

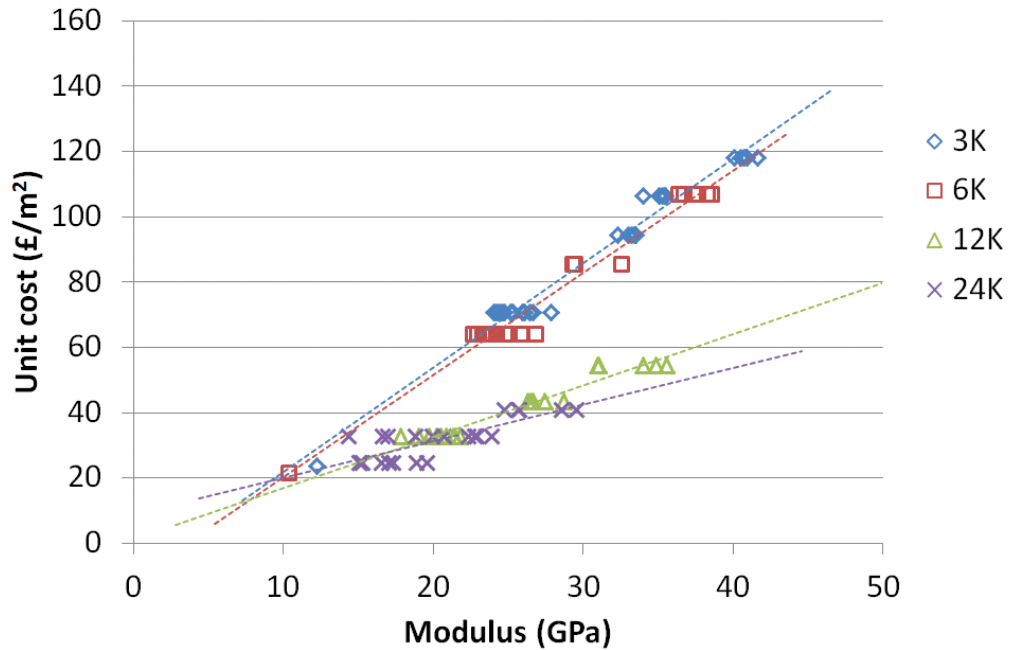


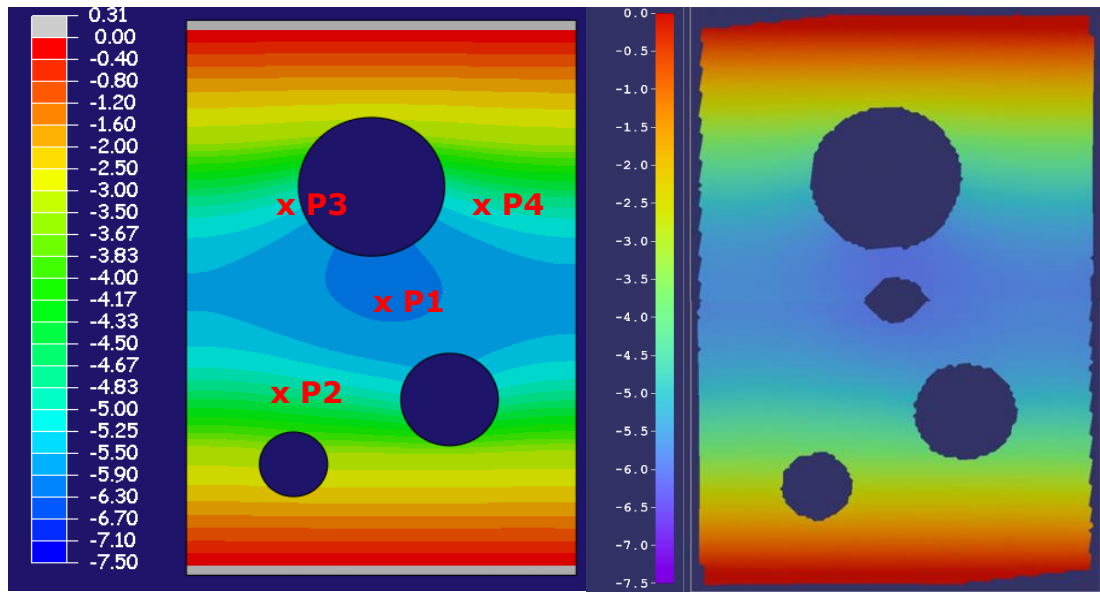
Figure 4-1: Relationship between material cost per square meter and composite modulus. For each tow size, data was obtained for specimens of various fibre length and volume fraction, but a linear relationship can be approximated between increase in material cost and composite modulus, as indicated by the dotted lines. The gradient of the line is highly influenced by the fibre type.

4.2.3 Model validation results

The quality of the FEA model setup has been evaluated by studying the bending performance of a flat plate with three arbitrary holes. Flat plates were manufactured from 2mm thick mild steel, and 4mm DCFP, which were subsequently tested on a fixture designed to impose the same boundary conditions as applied in the FEA. Details of the geometry and methodology can be found in Appendix D.

The displacement plot from the DIC analysis is presented in Figure 4-2 and compared with the FE results. No displacement data is available in the centre region of the DIC plot as the speckle was covered by the indenter. Nevertheless, the displacement contour from the DIC is in very good agreement with the FE prediction. Comparisons of displacement values from DIC, LVDTs and FE are presented in Figure 4-3 for four different locations. The errors are less than 5% between the different methods. This exercise has given confidence in the FEA setup, including

the choice of boundary conditions, the use of shell elements to represent the plate and the quality of the mesh.



(b)

Figure 4-2: Deflection (mm) distribution of the steel plate. (a) FE results. (b) DIC results. P1-P4 indicate the locations of the four LVDTs.

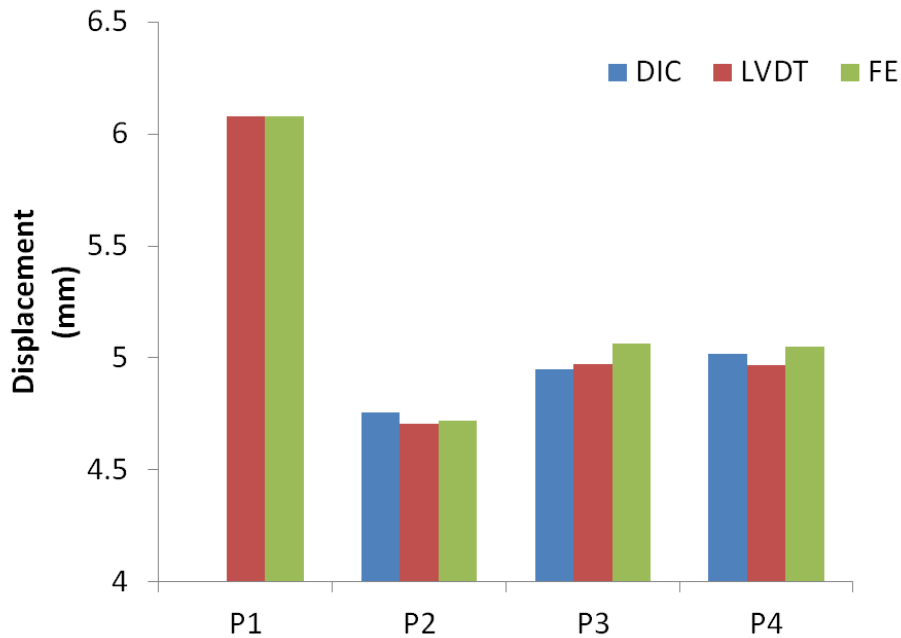


Figure 4-3: Comparison of the displacement values measured using different methods. Location of each point is indicated in Figure 4-2. No DIC data is available at P1 due to the loss of information under the indenter.

4.2.4 Optimisation results

The random fibre architecture of the 4mm thick DCFP plate used in Section 4.2.3 has been optimised using the algorithm outlined above. The optimisation starts from the un-optimised model with 4mm uniform thickness and 27.1GPa uniform modulus for all elements, which yields an overall weight of 1.04kg and fibre cost of £19.96. The model maximises the bending stiffness of the plate by minimising the total strain energy iteratively, while the overall weight and fibre cost remain constant. The maximum and minimum thickness bounds are 6mm and 2mm, and the modulus limits are 45GPa and 15GPa (Table D-1) based on volume fraction limits of 50% and 15% respectively.

Convergence of strain energy (Figure 4-4) is observed at the 10th iteration where the change in strain energy drops to less than 1% (see Figure 4-4). Variations of strain energy density distribution and total strain energy are presented in Figure 4-5 at three different stages (as indicated in Figure 4-4). According to Figure 4-4, the total strain energy has been reduced to only 47% of the un-optimised case. It is worth noting that at this stage, since the fibre architecture has not been determined, the variation of the effective composite density is ignored. Therefore, the constant volume constraint is effectively a constant mass constraint in this example (the mass of the two DCFP models is the same).

The thickness and modulus distributions for the optimised DCFP model are presented in Figure 4-6. Local changes in thickness and modulus appear in the regions where local stress concentrations exist (as shown in Figure 4-6). These continuously variable distributions are currently unrealistic from a manufacturing perspective, since the fibre deposition process is difficult to control to this level of precision. Discrete regions of high stiffness material need to be applied over much larger areas. This will be addressed by the developments in Sections 4.3.2 and 4.3.3, by introducing a zoning algorithm to group and then smooth areas of similar moduli. Continuously varying thicknesses however, can be achieved by varying the cavity height of matched tooling.

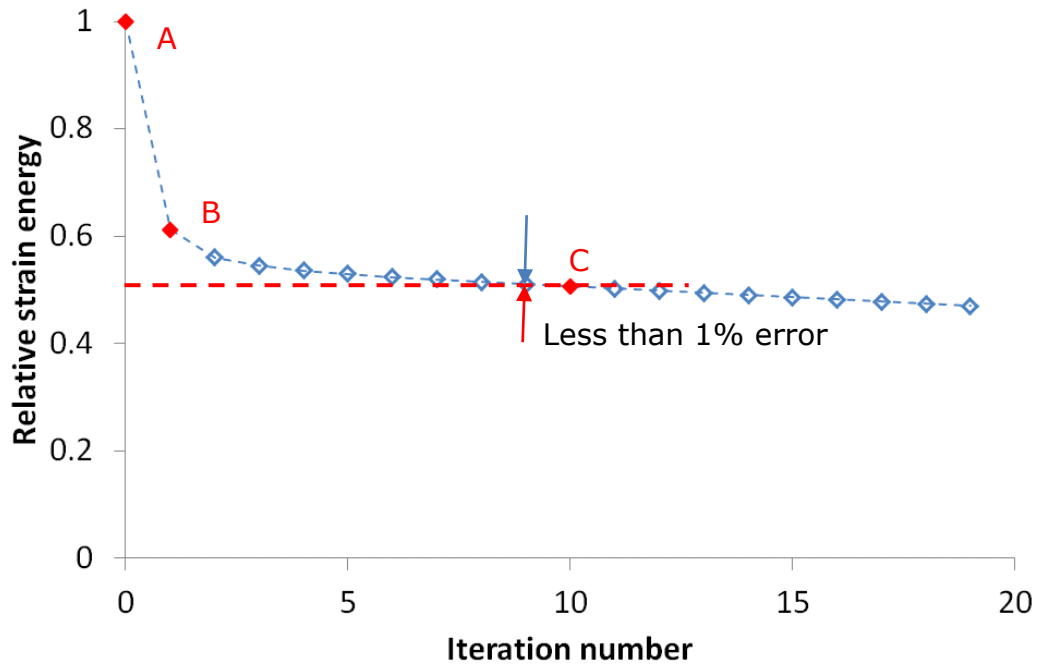


Figure 4-4: Convergence of strain energy (normalised to un-optimised value) during stiffness optimisation process.

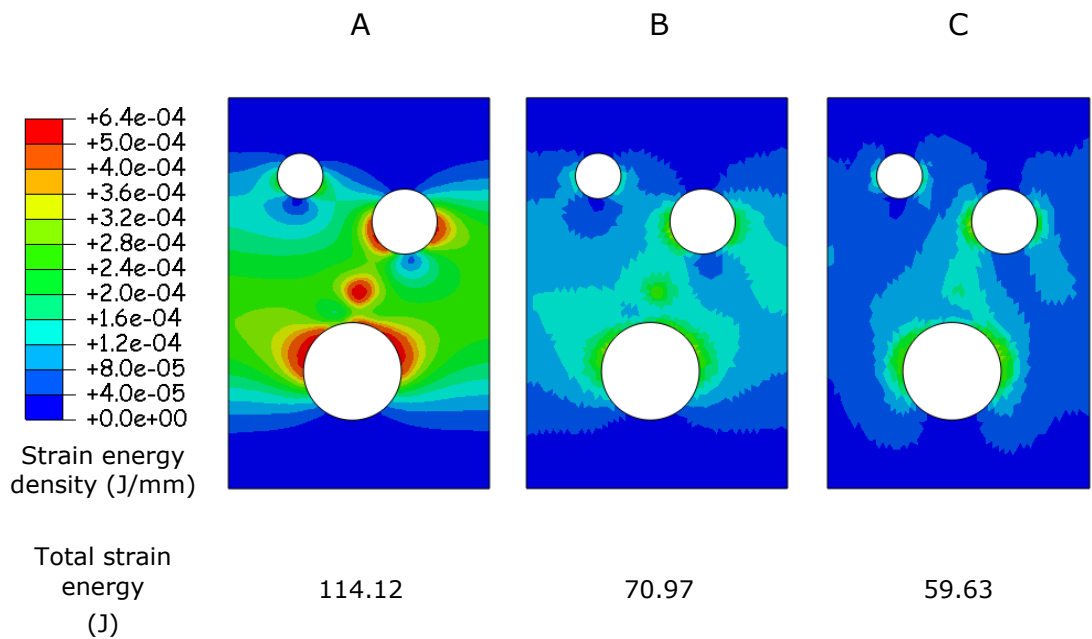


Figure 4-5: Comparison of strain energy distribution and total strain energy for iteration A, B and C (see Figure 4-4) of the optimisation process.

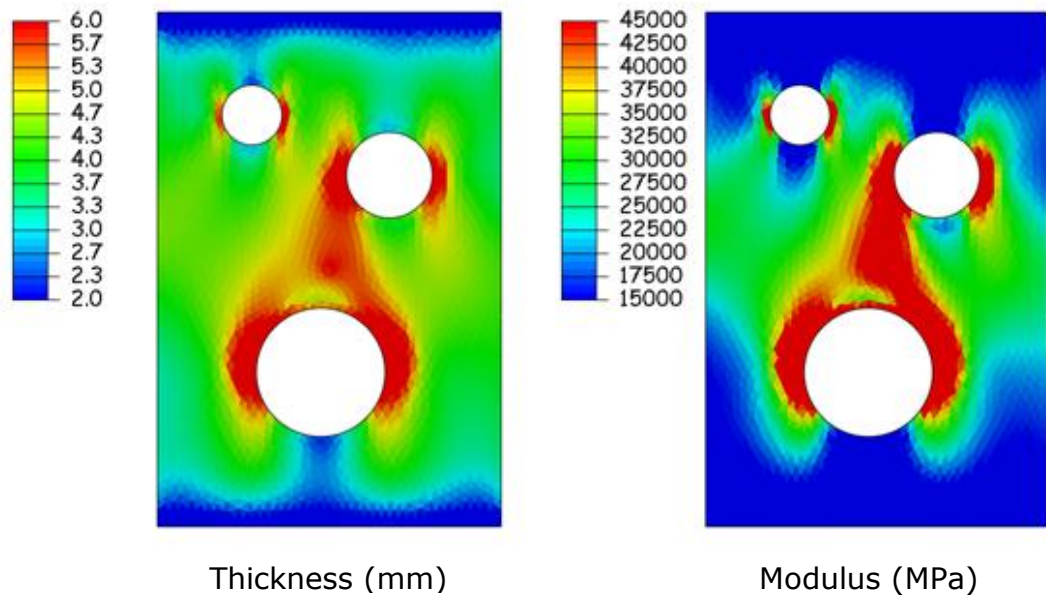


Figure 4-6 Thickness (left) and modulus (right) distribution of the DCFP plate after stiffness optimisation.

4.3 Determining the fibre architecture

4.3.1 Material assignment

This part of the model assigns the appropriate fibre architecture (selected based on material properties) to the optimised component. It takes the output from the initial stiffness optimisation (in the form of a local thickness and modulus distribution) and converts it into a fibre areal mass distribution of constant fibre tow size and fibre length. The optimisation routine is linked to a material database (see example in Figure 4-7) containing experimental Young's moduli for a range of DCFP plaques with various fibre architectures.

The database has been analysed to form simple relationships between each fibre architecture parameter and the resultant Young's modulus. The model utilises these continuous functions to express the thickness and modulus distributions in terms of fibre volume fraction for any predetermined fibre length and tow size. The volume fraction result is then combined with the thickness result to calculate the areal mass distribution, which is used directly to produce the robot deposition profile.

The FEA model developed in Chapter 2 has been used here to study the influence of fibre volume fraction on the tensile modulus of DCFP. A modified rule of mixtures (ROM) approach is shown to be a good approximation for summarising the relationship between Young's modulus and fibre volume fraction for DCFP. Figure 4-8 shows typical data for plaques with a fibre length of 57.5mm. Points on the graph are a combination of experimental and predictions from the FE model presented in Chapter 2, with lines representing predictions from ROM. Furthermore, Figure 4-9 suggests that there is a tendency for the modulus to reduce for thinner specimens, which is common for discontinuous fibre architectures. This thickness size effect has been considered in the current model by locally increasing the fibre volume fraction to compensate.

Figure 4-9 shows the relationship between Young's modulus and specimen thickness in more detail. It is evident that the data follows a bi-linear relationship, with a transition point occurring at 3.5mm for this particular fibre architecture. The Young's modulus increases linearly for increasing thickness, after which a plateau is reached. This transition point depends on factors such as fibre length, volume fraction and tow size, as they all influence the level of homogeneity and departure from isotropy [122]. However, due to limited experimental data, a 3.5mm transition point has been assumed for all DCFP materials in the current work.

It is worth noting that the current material model is only valid within certain thickness and volume fraction ranges: Very thin panels can cause buckling problems when used in real structures, and it is difficult to achieve uniform fibre distributions for very low fibre volume fractions or large tow sizes. In general, thickness values of less than 1mm are not recommended for DCFP of any tow size, fibre length or volume fraction. Feasible thickness and fibre volume fraction ranges are also limited by the liquid moulding process: Preform permeability may be too low for volume fractions approaching 50%, whereas preform washing may occur if the volume fraction is too low (<15%). Therefore the fibre volume fraction for the current study has been limited to 15-50%. Whilst the

thickness can be directly constrained within the stiffness optimality criterion method, the fibre volume fraction can be effectively constrained by restricting the Young's modulus limits in Equation 4-1.

Tow size	Fibre length (mm)	Vf	Thickness (mm)	Modulus (GPa)
3	50	0.25	2	19.25
3	50	0.3	2	22.57
6	25	0.3	2	20.75
6	25	0.35	2	23.77
6	50	0.25	2	17.95
6	50	0.35	2	24.07
6	50	0.3	2	21.01
12	25	0.25	2	14.85
12	25	0.3	2	17.29
24	25	0.25	2	11.43

Figure 4-7: Example of material database.

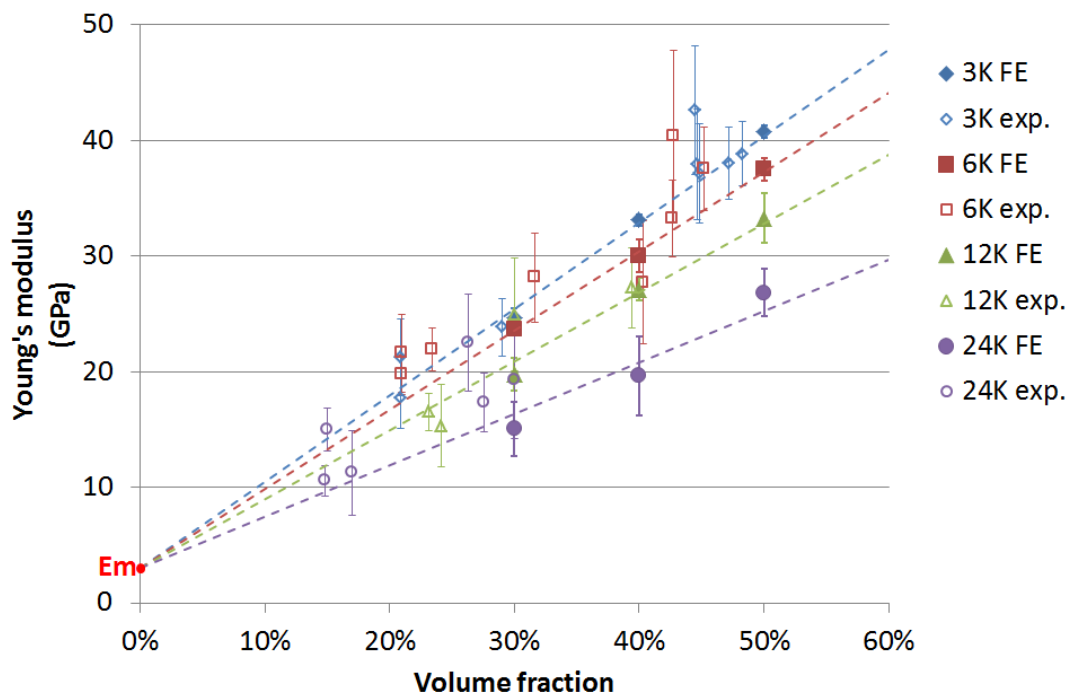


Figure 4-8 Young's modulus vs. fibre volume fraction for DCFP plaques with a 57.5mm fibre length. Error bars indicate the standard deviation of the Young's modulus value.

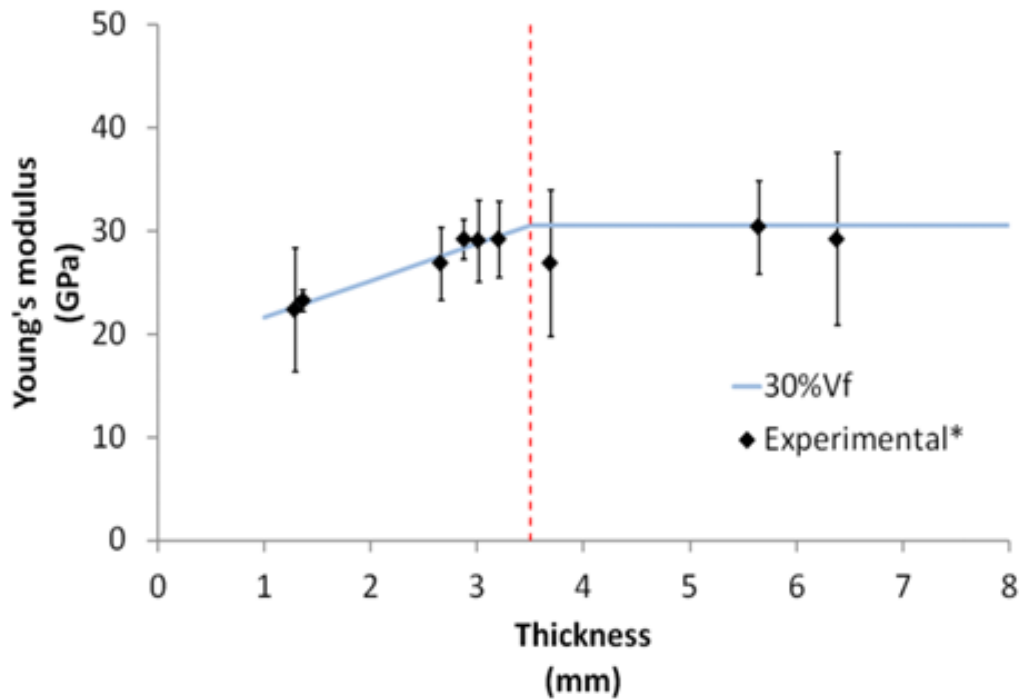


Figure 4-9: Young's modulus vs. specimen thickness for 6K 57.5mm DCFP. Experimental data are normalised to 30% v_f using rule of mixture. Error bars indicate the standard deviation of each specimen type.

4.3.2 Segmentation with multi-level thresholding

Otsu's method [124] is one of the most common thresholding methods for segmenting bi-level images. It states that the optimum threshold value should divide an image into two classes of pixels, so that the intra-class variance is minimised. A modified version [125, 126] has been used in the current work to conduct multi-levelled thresholding of the areal mass distributions generated by the stiffness optimality criterion.

The model searches within the areal mass range of 1000 to 4000gsm, using a fixed increment size of 10gsm, to determine optimum thresholds. Let ρ_A denote element areal mass, where ρ_{Amax} , ρ_{Amin} are the maximum and the minimum values. The range in areal mass is divided into N intervals K_1, K_2, \dots, K_N by the end points [1000, 1010, ..., 4000], such that $\{\rho_{Amin} \leq \rho_A < 1000\}$ for K_1 , $\{1000 \leq \rho_A < 1010\}$ for K_2, \dots , $\{4000 \leq \rho_A < \rho_{Amax}\}$ for K_N .

Assuming K_1, K_2, \dots, K_N are divided into M classes C_1, C_2, \dots, C_M by $M-1$ thresholds, the intra-class variance can be written as:

$$(\sigma_B)^2 = H_{C_1} + H_{C_2} + \dots + H_{C_M} \quad \text{Equation 4-19}$$

in which:

$$H_{C_i} = S_{C_i}^2 / P_{C_i} \quad \text{Equation 4-20}$$

P_{C_i} and S_{C_i} are called the zeroth-order moment and first-order moment of class C_i . Let K_a, K_b denote the first and the last intervals within C_i :

$$P_{C_i} = P_{(K_a, K_b)} = \sum_{n=a}^b p_{K_n} \quad \text{Equation 4-21}$$

$$S_{C_i} = S_{(K_a, K_b)} = \sum_{n=a}^b (p_{K_n} \cdot \mu_{K_n}) \quad \text{Equation 4-22}$$

where p_{K_n} is the probability that a ρ_A value belongs to interval K_n , and μ_{K_n} is the average areal mass value of elements enclosed by K_n .

The adopted algorithm searches the optimum thresholds by calculating the intra-class variance $H(K_a, K_b)$ for any possible class containing interval K_a to K_b ($1 \leq a < b \leq N$), using equations (7)-(9), and stores them in the following array:

$$\begin{bmatrix} H_{(K_1, K_2)} & H_{(K_1, K_3)} & \dots & H_{(K_1, K_{N-1})} & H_{(K_1, K_N)} \\ 0 & H_{(K_2, K_3)} & \dots & H_{(K_2, K_{N-1})} & H_{(K_2, K_N)} \\ \vdots & \vdots & \vdots & \vdots & \vdots \\ 0 & 0 & \dots & H_{(K_{N-2}, K_{N-1})} & H_{(K_{N-2}, K_N)} \\ 0 & 0 & \dots & 0 & H_{(K_{N-1}, K_N)} \end{bmatrix} \quad \text{Equation 4-23}$$

The optimum thresholds t_1, t_2, \dots, t_{M-1} can be determined by calculating $(\sigma_B)^2$ for any possible combination of $H(K_1, K_{t_1}), H(K_{t_1+1}, K_{t_2}), \dots, H(K_{t_{M-1}}, K_N)$ using the H array, and identifies the combination that yields a minimum value for $(\sigma_B)^2$.

Once all elements have been classified according to their areal mass, the model is refined into zones. A zone is defined as a group of elements that all belong to the same class and are bounded with one continuous boundary without self-intersection. The zoning process starts by randomly choosing an element as the seed. The zone expands by

continuously searching and merging surrounding elements if they belong to the same class. When no further merging can be performed, a new zone will be started with a random new seed. The process continues until all the elements have been allocated a zone.

4.3.3 Length scale and size control

The multi-level thresholding method uses the element areal mass value as the only criterion during segmentation, and does not take into account the connectivity between elements. Therefore, model zones can result in random shapes and sizes, especially for cases where the areal mass distribution is highly scattered. Length scale and size constraints have been enforced to remove small zones and repair any zone that contains regions narrower than the robotic fibre deposition head.

The minimum length scale of the zone is measured by constructing an equidistant curve from the zone boundary. The curve is formed by generating points that are perpendicular to the boundary, at a constant distance on the inside of the zone (see Figure 4-10).

If $2r$ denotes the minimum length scale of the zones, then r denotes the offset distance. Therefore the equidistant curve does not self-intersect unless the minimal length scale is smaller than $2r$. Figure 4-10 illustrates this approach, showing the approximate bounding polygon of the boundary nodes. The original zone (Figure 4-10a) contains a narrow region, therefore the equidistant boundary (dotted line) produces a singularity, due to self-intersection. The narrow region is removed by defining a new zone boundary (solid line, Figure 4-10b), which encompasses elements at a constant distance r in the outward direction to form a new equidistant boundary.

Elements removed from narrow regions are re-allocated into neighbouring zones, but care is taken to prevent narrow regions reforming. This is demonstrated in Figure 4-12, where elements removed during the previous iteration (white elements) are surrounded by four other zones (coloured and numbered). The white elements are reallocated to one of the other four regions using a 'region growth

process'. Only one layer of the white elements are merged at a time and the zone is selected based on the longest boundary (in this case the row of elements bordering zone 2). Size control is performed as the last stage and is to reduce manufacturing complexity by minimising the number of smaller zones. It can be easily achieved by adopting a threshold value of the minimum zone size, where areas smaller than the critical size will be discarded. A subsequent merging process is required to reallocate the resultant un-zoned elements, which can be performed in the same manner as the region growth step following the length scale control.

The final outputs after segmentation and length/size control can be converted into a thickness map and a fibre areal mass map, where the former can be used for the design of the RTM tool, and the latter for planning the fibre deposition program. The complete optimisation program is illustrated in Figure 4-11, with the initial stiffness optimisation steps on the left and the segmentation steps on the right. The optimisation program is implemented using the ABAQUS Python interface.

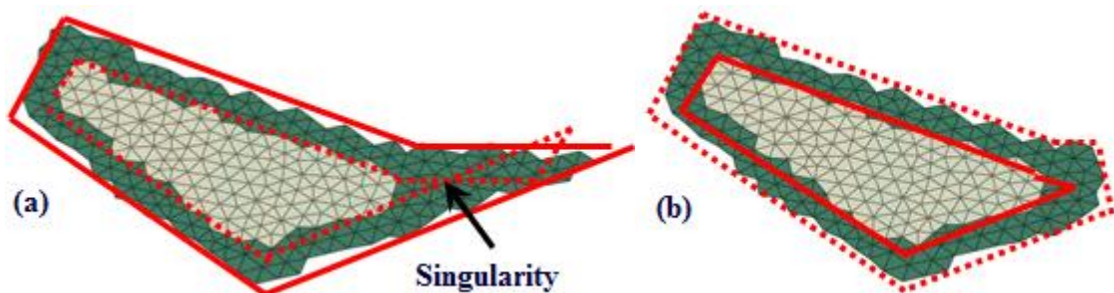


Figure 4-10 The equidistant boundary approach to control the minimum length scale of a zone. All solid lines indicate reference boundaries and all dotted lines indicate corresponding equidistant boundaries.

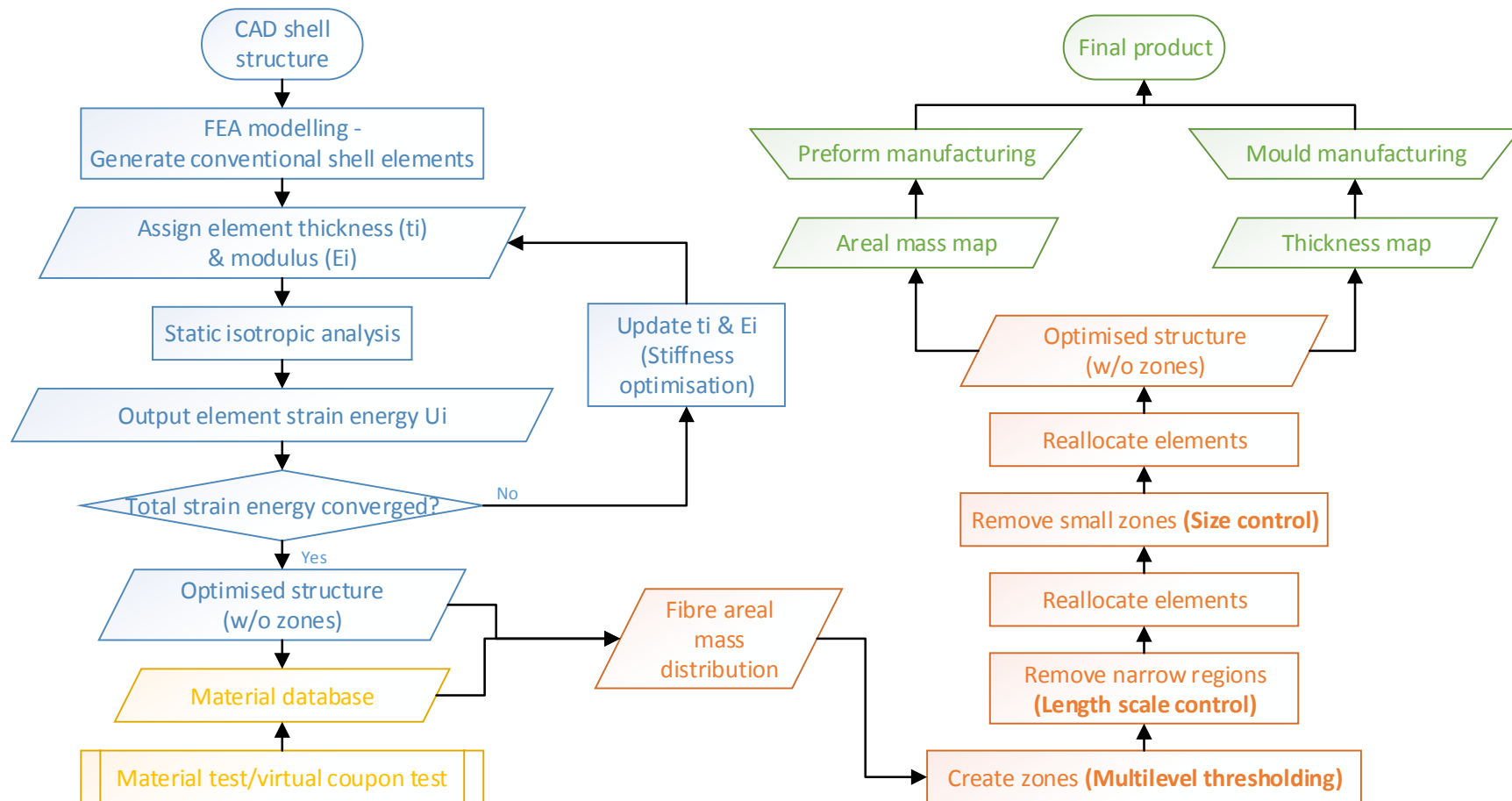


Figure 4-11 Flow chart of the optimisation process. Blue blocks indicate steps of the stiffness optimality criterion method. Orange blocks indicate steps of areal mass segmentation process. Yellow blocks indicate input data from the upstream material database generation. Green blocks indicate downstream manufacturing process.

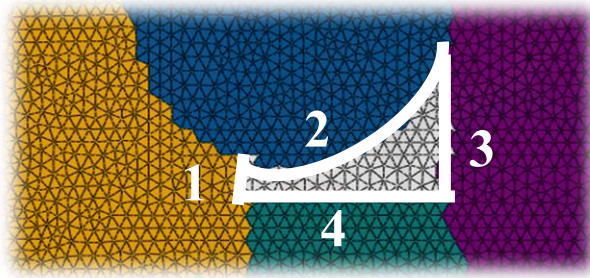


Figure 4-12 Schematic diagram of the region growth process. The white region in the centre indicates the un-zoned elements and the coloured, numbered regions indicate the existing zones.

4.3.4 Results

This section will continue with the model presented in section 4.2 to demonstrate the segmentation and size control methodology described in 4.3.1-4.3.3. Figure 4-13 shows the effect of varying the number of areal mass levels on the overall areal mass distribution, based on a 3K tow size and 30mm fibre length. As expected, a reduction in component stiffness is found as the number of levels decreases, indicated by an increase in maximum deflection. With 9 levels, the maximum deflection is increased by 1% compared with the original model before segmentation. However, there is just a 4.5% increase in maximum deflection when the number of segmentation levels is reduced to 4. This equates to an error of just 5.4% compared to the fully optimised model presented in Figure 4-6.

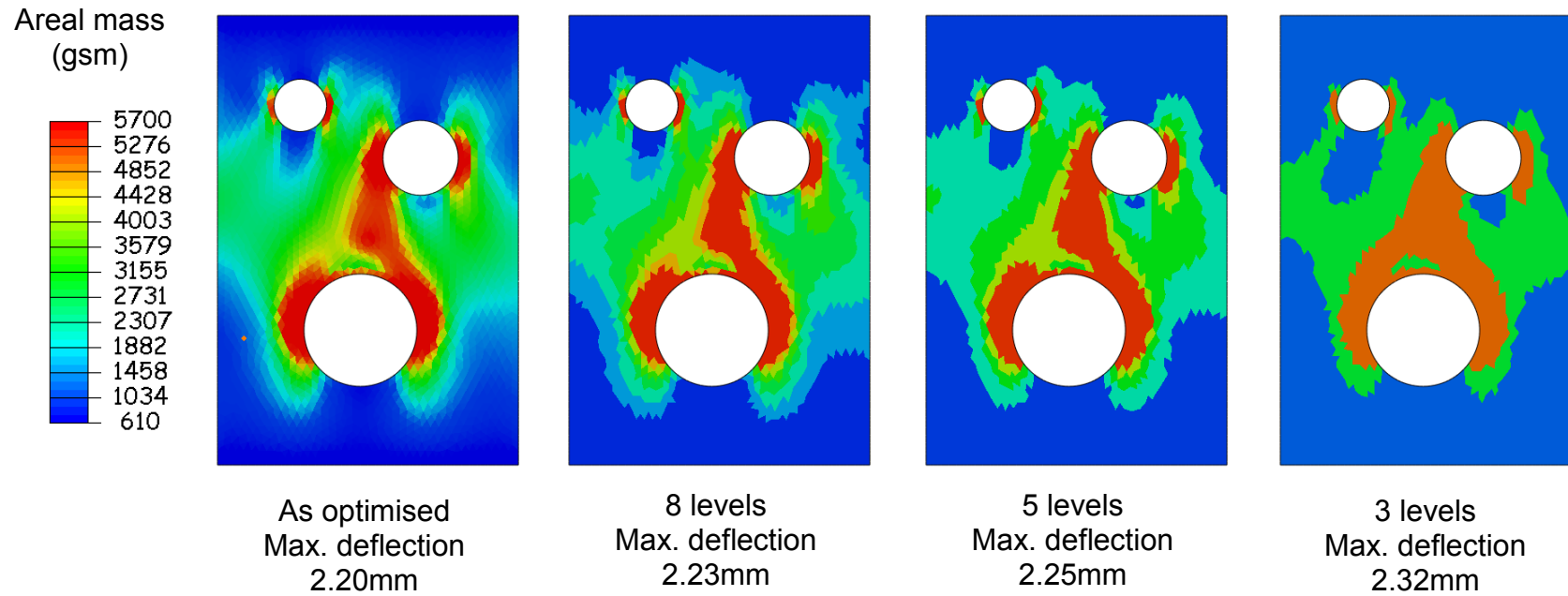


Figure 4-13 Preform fibre areal mass distribution of the optimised model after segmentation with multi-level thresholding.

Models with length-scale and zone size control are presented in Figure 4-14, where 30mm minimum length-scale and 80x80mm² minimum zone size limits are applied. From Figure 4-14, it can be shown that applying length-scale and size control reduces the complexity of the zones. However, as the modifications to the zones are driven by geometry considerations, further reduction in structural stiffness is expected. For models based on 3 levels, the maximum deflection is increased by 4% due to the length-scale and size control, and for the case of 5 levels, the maximum deflection is increased by 5%. Nevertheless, there is still a notable gain in structural stiffness even with the model segmentation process: For models with 3 levels presented in Figure 4-14, the maximum deflection is 52% of the un-optimised model, and 51% for the case of 5 levels.

Figure 4-15 demonstrates the impact of applying areal mass segmentation on the structural stiffness of the plate, for the models presented in Figure 4-14. The total strain energy of each model is normalised according to the un-optimised model and compared. In strain energy terms, the total strain energy for the 3-level model increases by 10% after all segmentation steps, and 8% for the 5-level model. Consequently, the maximum deflection of the model is increased from 2.20mm to 2.40mm for the 3-level model (9%), and to 2.36mm for the 5-level model (6.8%). Breaking these values down step-by-step, it is possible to see that the thresholding stage is the most significant source of error for the 3-level model and length-scale for the 5-level model, with the size control the least significant for both cases. After thresholding (step 2 in Figure 4-15), the 3-level model experiences a 5.5% increase in strain energy, compared with 3.2% for the 5-level model, due to its less refined areal mass distribution. Following length-scale control (step 3 in Figure 4-15), a further 3.5% strain energy increment is introduced to the 3-level model, compared with 4.9% for the 5-level model. Higher errors were expected for the 5-level model since it was more likely to contain small areas, which would be classified into zones bounded by a different set of thresholds. Finally, the size control (step 4 in Figure 4-15) increases the error for the 3-level model by a further 0.89%, and 0.87%

for the 5-level model. It is clear that applying model segmentation and geometric constraints only compromise the overall level of optimisation by a very small amount. However, this compromise is considered to be essential in terms of producing realistic fibre architectures that are fit for manufacture.

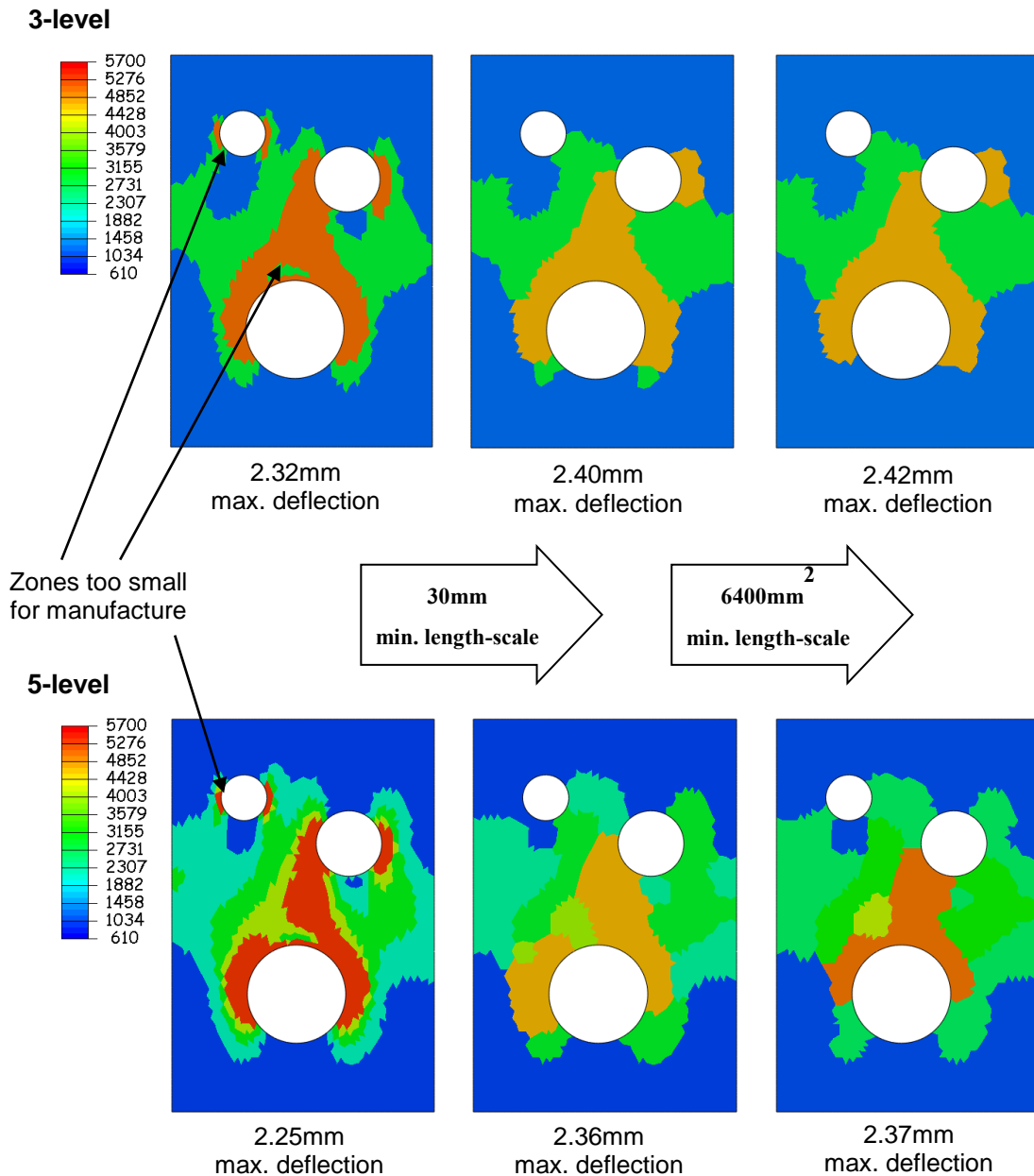


Figure 4-14: Areal mass distribution after applying length-scale control and size control.

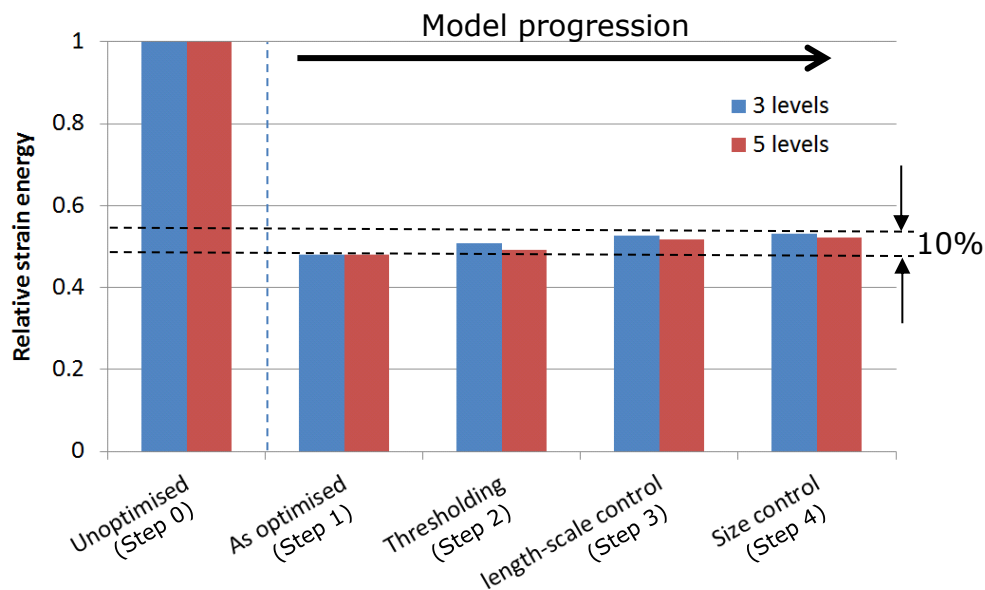


Figure 4-15: Influence of areal mass segmentation on the overall stiffness of the optimised model. Strain energy values are normalised to un-optimised model.

The sensitivity analysis presented in Figure 4-15 has been extended to understand the impact of varying all of the segmentation parameters (thresholding levels, minimum length-scale and minimum zone size) on the stiffness of the final optimised model. Models for a range of thresholding levels (3 to 6), minimum length-scales (30, 40 and 50mm) and zone sizes (2500mm² and 6400mm²) have been studied, and the results are presented in Figure 4-16 in terms of the increase in strain energy compared with the 'as-optimised' model. It should be noted that the final segmentation level is not necessarily the same as the number of thresholding levels due to the subsequent length-scale control and size control.

In general, the increase in strain energy is dominated by the length-scale control (except models with 3 thresholding levels and 30mm minimum length-scale), which increases as the minimum length-scale increases. Increasing the number of thresholding levels also causes a further rise in strain energy, as it increases the likelihood of small, narrow zones forming. These subsequently get modified during the length-scale control,

which is reflected in the associated errors. Size control has minor impact for all scenarios in Figure 4-16, with the influence only increasing as the minimum zone size increases. It is interesting that some scenarios are not affected by the subsequent size control at all, which is because the previous length-scale control has effectively removed zones that are smaller than the minimum size. It is worth noting that the influence of each segmentation parameter varies as the initial areal mass distribution changes, therefore proper implementation of the segmentation strategy should consider the geometry of the model and the as-optimised areal mass distribution.

This study has shown that the length-scale control represents the biggest compromise to the stiffness when compared to the as-optimised model. In order to minimise the effect of the segmentation process, all parameters need to be carefully selected. For example, the number of thresholding levels directly influences the number of zones, and therefore must be minimised to reduce the length and complexity of the robot program. The length-scale of the zone needs to be large enough to achieve representative material properties; to reduce variation and improve reliability, as demonstrated in Chapter 2. The minimum length-scale is also influenced by the fibre deposition cone of the chopper gun, but the selected value should be minimised to reduce the resulting compromise in stiffness. Finally, the minimum zone size is also important in term of preform variability as the boundary effects can increase as the zone size decreases.

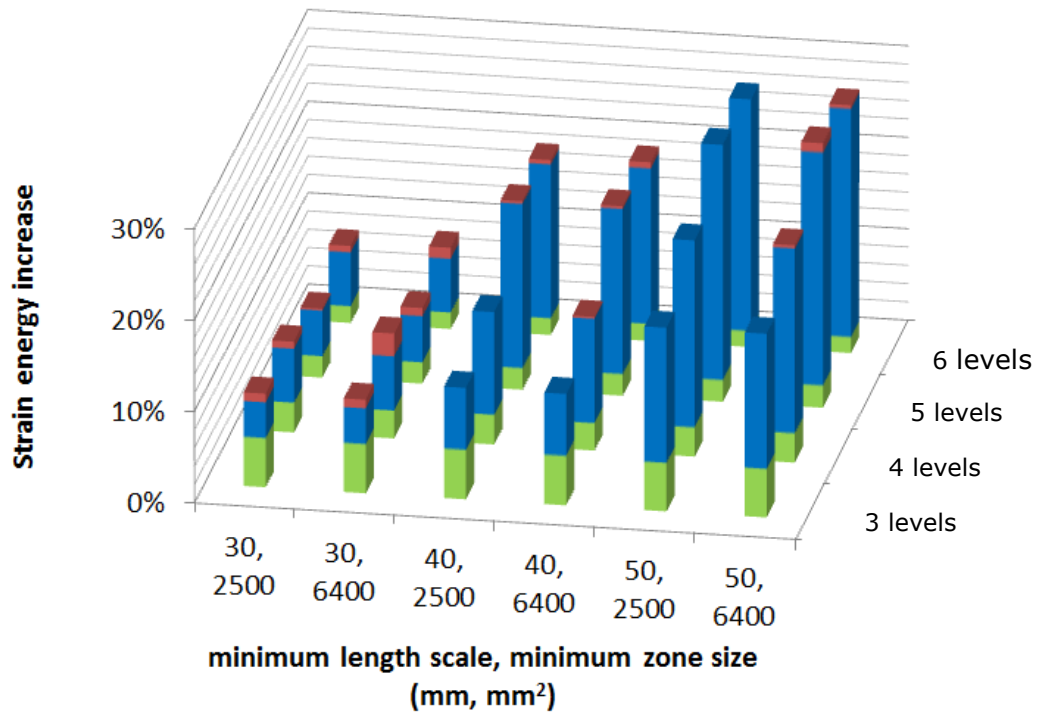


Figure 4-16: Effect of varying the number of thresholding levels, minimum length-scale and minimum zone size on the structural stiffness of the plate. Increase in strain energy is calculated based on the as-optimised model (step 1). Green bars indicate strain energy increase caused by thresholding (step 2), blue bars by length-scale control (step 3) and red bars by size control (step 4).

4.4 Conclusions

A stiffness optimisation method has been developed to locally vary the thickness and areal mass distribution for a DCFP component. The stiffness of the component is maximised under the constraints of constant volume and material cost. The optimisation algorithm is derived using the stiffness optimality criterion, and the Lagrangian multipliers are solved for each optimisation constraint. A segmentation algorithm has been implemented to divide the resulting fibre architecture into several zones of similar areal mass, where the size and shape of each zone is optimised to suit the precision of the fibre deposition process.

The optimisation algorithm has been demonstrated using a flat rectangular plate with three holes. Results suggest that the current method can effectively improve the stiffness of the component without sacrificing weight-saving potential or adding additional cost over the

original DCFP benchmark. The subsequent segmentation model ensures that the optimised structure is fit for manufacture, with little impact on the overall structural performance compared with the as-optimised solution. Comparison of various segmentation strategies suggest that the correct approach should be determined according to the model geometry and the areal mass distribution of the as-optimised model, where the optimisation strategy needs to be determined from the historical structural stiffness data of the trials.

The plate geometry presented in this chapter only demonstrates the basic capability of the model; to maximise the stiffness and to determine the fibre architecture of the optimised structure. It is worth noting that utilising this structural optimisation tool allows more efficient use of materials, therefore there is great potential for achieving weight and cost reduction with the proposed model. This will be demonstrated in more detail in Chapter 5, using an automotive component case.

Chapter 5. Case Study: Stiffness optimisation of a structural automotive component

5.1 Introduction

The structural optimisation of an automotive spare wheel well is presented in this Chapter to further demonstrate the optimisation model proposed in Chapter 4. The spare wheel well forms part of the rear floor structure for a large luxury-sector vehicle and is currently in production using a combination of carbon/glass non-crimp fabrics. The aim of this study is to understand if a highly optimised DCFP solution can compete in terms of specific stiffness, whilst presenting an opportunity for cost reduction against the NCF counterpart.

Whilst stiffness is one of the most significant drivers in structural optimisation, quite often the design is assessed against multiple criteria, of which some are non-structural, such as weight, cost and manufacturing cycle time. Although stiffness is the only design objective in the current model, weight and cost reduction can be achieved by manually reducing the target component mass and material cost. The model proposed in Chapter 4 is not capable of directly solving multi-objective problems; therefore a material selection step is performed, prior to the stiffness optimisation and material assignment, to determine the initial fibre architecture for the optimisation process.

A series of structural optimisation solutions are derived at different weight and cost levels, using a TOPSIS approach (see Section 5.2) to rank candidate materials according to different weighting strategies. The automotive demonstrator component has been specifically selected to demonstrate how the model can be successfully used to optimise the fibre architecture of discontinuous fibre components. The component is used to primarily house the spare wheel, but also a pair of 12V batteries. The 'spare wheel well' (Figure 5-1) is required to be sufficiently stiff to avoid NVH (Noise, vibration, and harshness) issues within the passenger

cell, but also needs to be durable, as the exterior surface is exposed to impact from road debris.

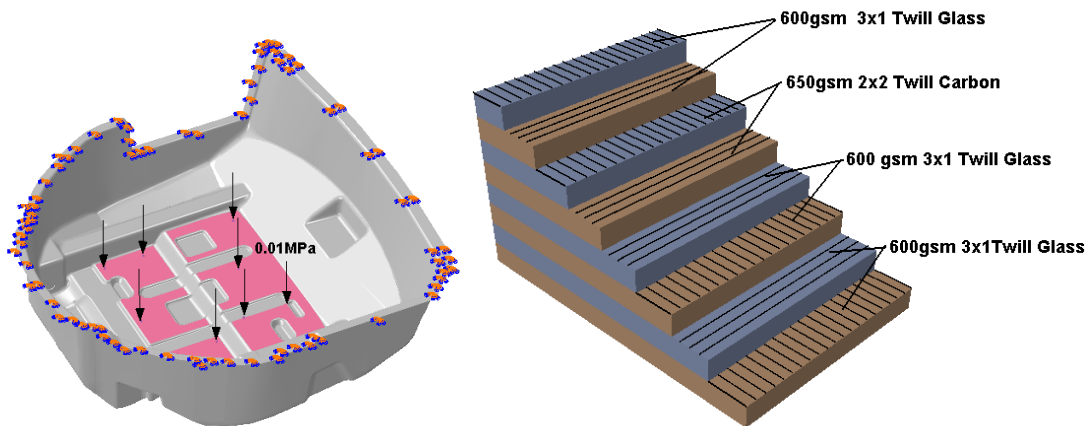


Figure 5-1 Left: Un-deformed shape of the spare wheel well. (0.01MPa uniform pressure applied on the pink surface) Right: Ply layup arrangement of the current composite laminate.

5.2 Decision Making Criterion

A Multi-Criteria Decision Making (MCDM) strategy is adopted to judge alternative solutions [127] produced from the large volume of mechanical data (currently 385 scenarios) available in the material database (various tow sizes, fibre lengths, volume fractions and thicknesses).

The weighted sum model (WSM) is the most well-known and simplest MCDM strategy, where the weight of each criterion is determined by the user [128]. For every alternative solution, a score can be obtained for each criterion and the optimum solution is determined from the sum of the weighted score. The WSM does not involve normalisation of data, therefore only works when all criteria are measured with the same unit. The weighted product model (WPM) [129] is an improvement of the WSM which is suitable for dimensionless analysis, regardless of the quantities measured and the units. The problem with both WSM and WPM is that

they require all criteria to be monotonically increasing or decreasing, which restricts their implementation in many cases. For instance, they are unsuitable for many automotive design problems, since primary structural components usually require the fracture toughness to be maximised but the weight to be minimised.

The Technique for Order of Preference by Similarity to Ideal Solution (TOPSIS) [130, 131] is an alternative MCDM that uses weights to estimate the relative importance of each criterion, but criteria can be either increasing or decreasing. Two artificial solutions are hypothesised with the TOPSIS method; an ideal solution that has the most preferred values of all criteria, and a negative ideal solution that has the least preferred values of all criteria. For each alternative solution, TOPSIS measures distances from the ideal solution and from the negative ideal solution, and the best solution is chosen that is closest to the ideal and farthest from the negative ideal. A full derivation of the TOPSIS approach is provided in Appendix E.

5.3 Candidate materials

The production component comprises an inner and outer skin with local areas of foam core to create a sandwich construction. The layup has been simplified into a monolithic component (ignoring cores) for the purpose of this study and the assumed layup is presented in Figure 5-1. A single ply of 650gsm 2×2 twill weave carbon fabric is sandwiched about 3 plies of 600gsm 3×1 twill weave glass, in order to prevent a conductive path between the battery terminals and the body in white.

A replacement for the glass/carbon woven composite has been proposed using an all-carbon fibre layup consisting of 650gsm 2×2 twill weave carbon fibre plies. The ply count is manually optimised (as shown in Figure 5-2) to provide a comparable maximum deflection to the glass/carbon hybrid, whilst minimising the weight and cost of the part. The all-carbon NCF solution offers great weight saving potential without

impacting on the structural stiffness. However, the anticipated reduction in component mass cannot be justified in this case because of the added material cost, which is typically greater than 50%.

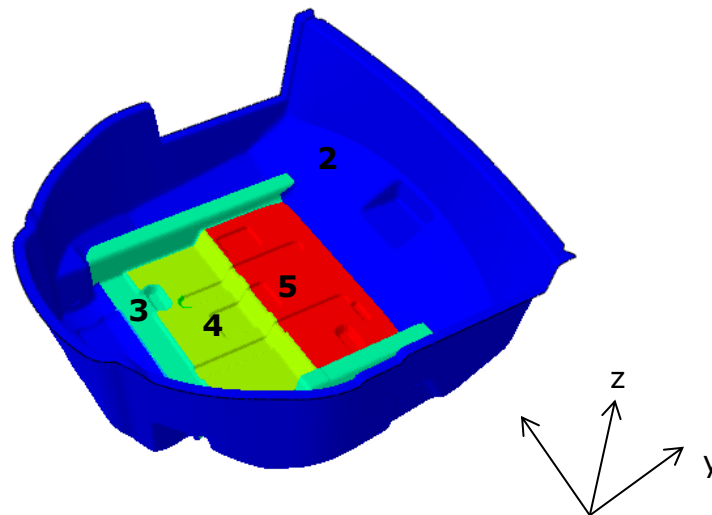


Figure 5-2: Ply configuration of the continuous carbon model. Numbers indicate the ply count of 650gsm 2×2 twill weave carbon fibre. The compass shows the material orientation where x- axis refers to 0 deg and y-axis refers to 90 deg.

A series of optimised DCFP replacements has been designed using the structural optimisation algorithm, to demonstrate that the performance of DCFP can compete against continuous fibre solutions, albeit at a fraction of the cost. The material cost for DCFP is approximately 50% lower than a textile solution because no intermediate processing is required and there is no fibre wastage. The process is also fully automated, which eliminates all touch labour to create further cost savings. DCFP fibre architectures selected in this chapter are based on tow sizes of 3K, 6K, 12K and 24K, at available fibre lengths of 25mm and 50mm. Smaller tow sizes (3-6K) are typically preferred for higher performance applications where the higher material costs can be justified. (The cost per unit mass for 3K fibre is three times that for 24K fibre). The global fibre volume fraction for the un-optimised version is chosen from 25%, 30%, 35% and 40%, and the thickness varies from 2mm to

4mm in 0.2mm increments. The critical length-scale is chosen to be four times the fibre length in the segmentation step, to ensure a suitable RVE size is used to achieve representative in-plane stiffnesses according to Chapter 2. A minimum zone size constraint of 22500mm² is used.

The material database used in this chapter is presented in Figure E-1, which includes fibre architecture parameters, the resulting Young's modulus, and all criteria considered in the TOPSIS analysis. Materials are assessed by three main criteria: stiffness, weight and cost. Sub criteria are applied to stiffness and cost to account for the influence of additional factors. The stiffness criterion is divided into three parts: tensile stiffness, bending stiffness and stiffness retention. The cost criterion is divided into the cost of the raw materials and a cycle time dependent manufacturing cost. The tensile and bending stiffnesses can be calculated as

$$\text{tensile stiffness} = Et \quad \text{Equation 5-1}$$

$$\text{bending stiffness} = \frac{Et^3}{12} \quad \text{Equation 5-2}$$

where E , t denote the Young's modulus and section thickness.

According to the specified loading configuration of this model, a ratio of 1:2:1 has been assigned to the tensile stiffness, bending stiffness and stiffness retention criteria. The cost model adopted for the material selection consists of two elements: the cost of the raw materials and a cycle time dependent manufacturing cost. A ratio of 5:2 has been adopted for the cost sub-criteria in this work.

As discussed in Chapter 4, segmentation of areal mass always introduces reduction in structural stiffness due to the error between the as-optimised model and the segmented model. The stiffness retention sub-criterion therefore means the ratio between the stiffness of the segmented model and that of the as-optimised model. Results from Chapter 4 suggest that varying the critical length-scale during segmentation has a significant impact on the stiffness retention of the segmented model. As the critical length-scale here is proportional to the fibre length, stiffness retention is expected to be higher for 25mm fibre

lengths than for 50mm fibre lengths. It is therefore assumed that the retention value is 75% for 25mm fibre lengths and 50% for 50mm fibre lengths.

Two case studies are presented in the following section. One seeks a high stiffness and lightweight design regardless of cost, and the other takes component cost into consideration to provide the most economical solution for the same target specific stiffness. Further refinement can be achieved by restricting the materials available at the selection stage, by imposing limits on total weight and cost. Therefore for each case study, two scenarios are discussed. The first one selects the most appropriated fibre architecture without any restriction. The second scenario only rates materials with areal mass smaller than that of the continuous glass/carbon benchmark (3650gsm), and areal cost smaller than that of the continuous carbon option (£54.02/m²). The four studies are summarised in Table 5-1. The material properties for the continuous glass/carbon and all carbon models and the un-optimised DCFPs are summarised in Table 5-2.

Table 5-1 Summary of scenarios investigated for the two case studies

	Without restrictions	With cost and weight limits
Case 1: High stiffness & lightweight	Scenario 1	Scenario 2
Case 2: Low cost	Scenario 3	Scenario 4

Table 5-2 Material parameters for all benchmark materials and un-optimised DCFPs used for the case study.

	E_1 (MPa)	E_2 (MPa)	ν_{12}	G_{12} (MPa)	G_{13} (MPa)	G_{23} (MPa)	Ply thick (mm)	Density Kg/m ²	Unit price (£/m ²)
3x1 Twill Glass Fibre (600gsm) [132]	43400	9770	0.256	4090	4090	3560	0.44 *	3.650	5.12
2x2 Twill Carbon Fibre (650gsm) [133]	132500	10530	0.256	4444	4444	3787	0.66**	3.042	24.40
Scenario 1: DCFP 3k 50mm , 40% ν_f	37570	37570	0.3	14450	14450	14450	4	5760	126.59
Scenario 2: DCFP 3k 25mm , 30% ν_f	21570	21570	0.3	8296	8296	8296	2	2754	47.47
Scenario 3: DCFP 12k 25mm, 30% ν_f	22230	22230	0.3	8550	8550	8550	4	5760	43.82
Scenario 4: DCFP 24k 50mm, 25% ν_f	13510	13510	0.3	5196	5196	5196	2	2754	13.69

* Idealised laminate contains 2×0.22mm UD plies.

** Idealised laminate contains 2×0.33mm UD plies.

5.4 Results

5.4.1 Influence of fibre architecture parameters

In order to understand the effects of varying fibre architecture parameters, a statistical analysis has been performed to sum the TOPSIS score of all possible permutations for each of the 385 fibre architecture considered. The weighting for each criterion is changed in 1% increments, with the sum of all weights remaining unity. A total of 171700 weighting strategies were analysed (see Figure 5-4). Main effects on the total TOPSIS score are presented in Figure 5-3, where the influence of tow size, fibre length, volume fraction and thickness is demonstrated. The analysis is performed using Minitab v16.2.2, and the value of each data point is calculated as the mean value of all options of the same fibre parameter value. The total TOPSIS scores in Figure 5-4 reflect the possibility that certain fibre architectures may be ranked as the best option more frequently than others, whilst lower values are never selected for any weighting strategy.

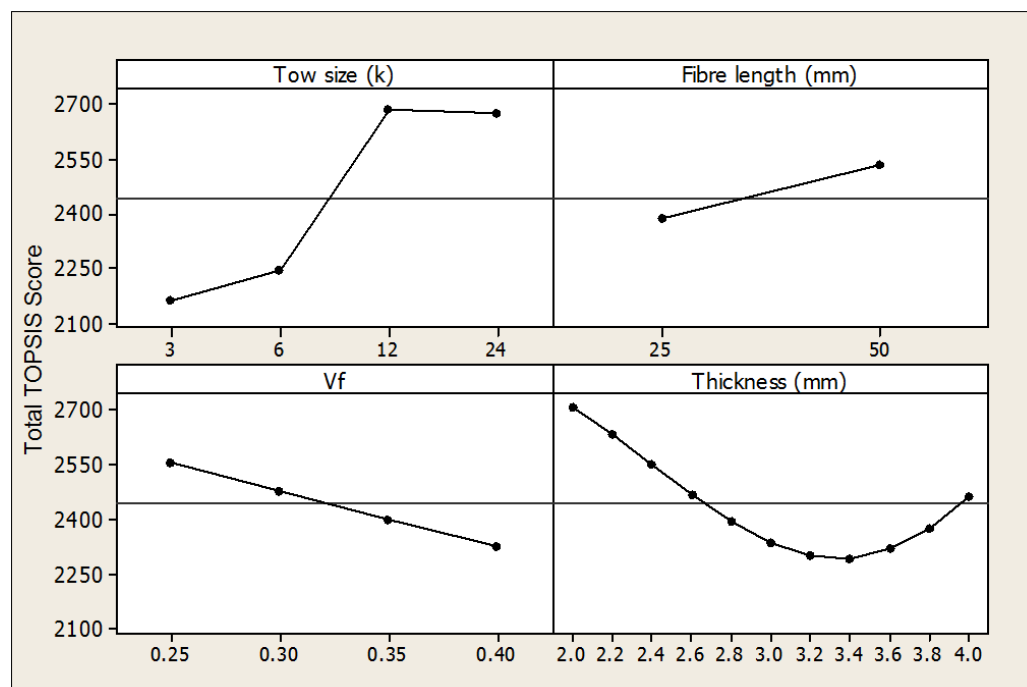


Figure 5-3: Main effects plot for the total TOPSIS score of all weight permutations. The weights are changed in step size of 0.01, therefore a total of 171700 permutations are included. The TOPSIS score for a single permutation is between 0 and 1.

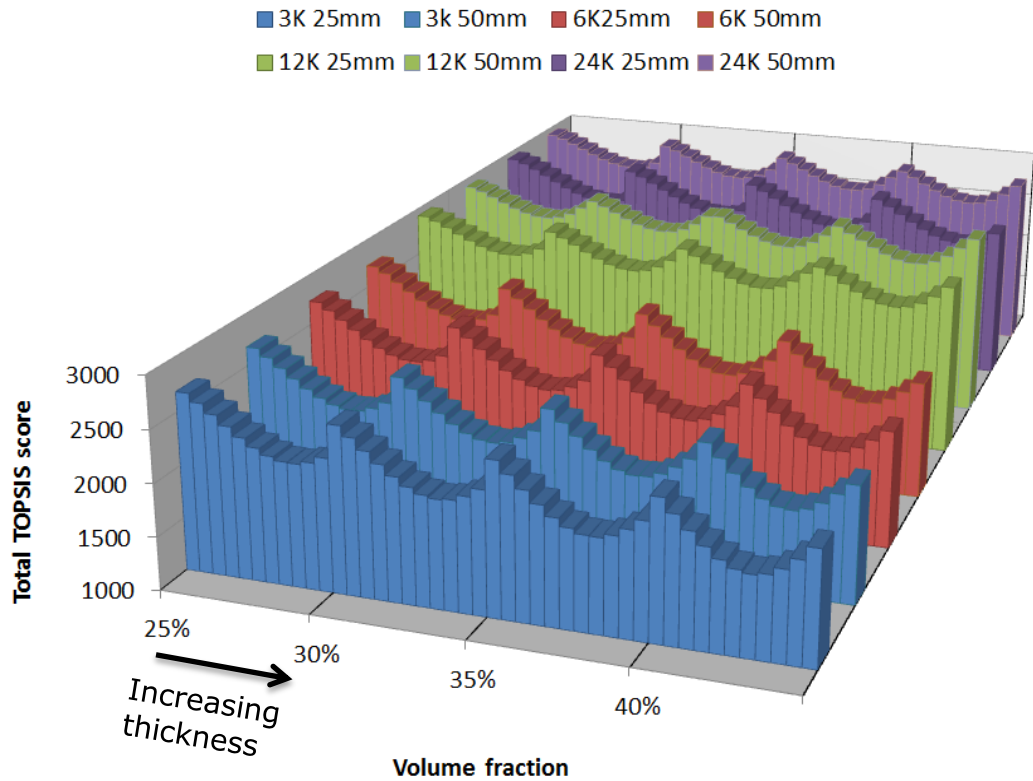


Figure 5-4: Total TOPSIS scores for 385 fibre architectures available from the material database, calculated from a total of 171700 weight permutations.

In general, tow size has the most significant effect on the total TOPSIS score. The influence of tow size on the TOPSIS score reflects the cost to stiffness ratio of each tow size, which is lowest for 3k fibre and highest for 12k and 24k fibre.

Thickness has the second most significant effect on the total TOPSIS score. The influence of varying thickness is relatively complicated as the majority of criteria including tensile stiffness, bending stiffness, weight and cost are all associated with thickness. Influence of varying thickness is demonstrated in Figure 5-5 where the example data are taken from all DCFPs of 3k, 25mm fibre length and 35% volume fraction. Note that in Figure 5-5, the weight, material cost and cycle time are plotted in reverse order to indicate an undesirable trend of increasing weight and cost. Whilst weight, material cost and cycle time are linearly proportional to the thickness, tensile stiffness and bending stiffness increase at a

higher rate. This is partly because the cross-sectional area and second moment of area increase non-linearly with thickness, but also the Young's modulus increases concurrently due to the size effects as demonstrated in Figure 4-9. Therefore, for thinner panels (less than 3.4mm according to Figure 5-3), the TOPSIS score is improved by lightweight, low cost and low cycle times. Additionally, if the thickness continues to increase, the TOPSIS score is also improved by a high stiffness value.

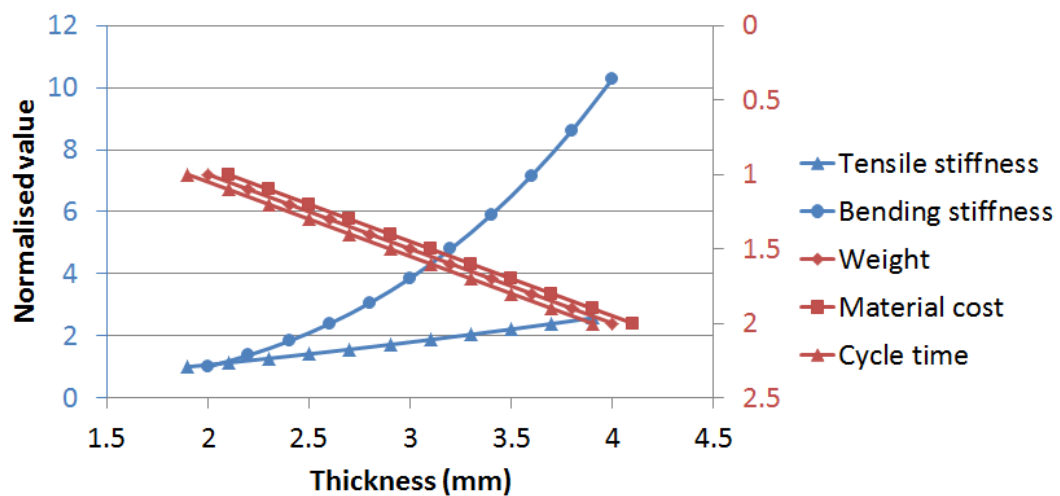


Figure 5-5: Effects of varying thickness on the tensile stiffness, bending stiffness, weight, material cost and cycle time. Example data are based on DCFP of 3k, 25mm fibre length and 35% v_f . Vertical axis values are normalised to 2mm thickness. Thickness values are offset to clarify the data. The secondary axis (red) is plotted in reversed order to represent the unfavourable trend of increasing weight and cost.

Both volume fraction and fibre length have a relatively minor influence on the total TOPSIS score. Similar to thickness, the influence of varying fibre volume fraction is also complicated, as stiffness, weight and cost are all affected (see Figure 5-6). The influence of volume fraction on the five sub-criteria shown in Figure 5-6 for a 3k, 25mm DCFP plaque with a 3mm section thickness. All criteria are shown to exhibit a linear correlation to volume fraction. According to Figure 5-6, the gradient of the weight curve is the lowest, while material cost and cycle time have the largest gradient due to the large cost ratio between fibre and resin (5274 for 3k fibre and 1826 for 24k fibre). Therefore, the overall TOPSIS

score is dominated by the negative effects of increased weight, material cost and cycle time, and continuously decreases as the volume fraction increases. Fibre length only affects the stiffness of the part. Although Young’s moduli for DCFPs of 50mm fibre length are generally 5% higher than those of 25mm fibre length, a 50mm fibre length has a lower optimality due to lower stiffness retention from segmentation. It is worth noting that there are insufficient entries in the current material database to study in detail the sensitivity of total TOPSIS score to the change in fibre length.

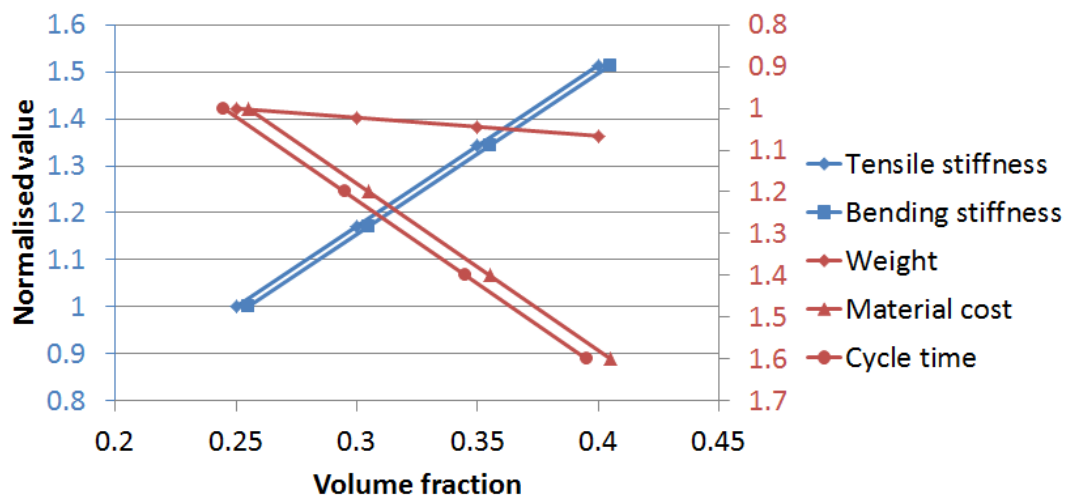


Figure 5-6: Effects of varying volume fraction on the tensile stiffness, bending stiffness, weight, material cost and cycle time. Example data are based on DCFP of 3k, 25mm fibre length at 3mm thickness. Vertical axis values are normalised to 25% volume fraction. Volume fraction values are offset to clarify the data. The secondary axis (red) is plotted in reversed order to represent the undesirable trend of increasing weight and cost.

Understanding the influence of fibre architecture parameters on the TOPSIS score helps to identify materials that are preferred for different design scenarios, and also helps to identify materials that are unlikely to be selected. Whilst this section of the thesis considers the overall influence of each parameter, the following two case studies will discuss the suitability of using selected architectures for real components. The TOPSIS weight for each criterion will be limited to a narrower range of values according to the definition of each case.

5.4.2 Case 1: High stiffness and lightweight

The current case study analyses all weighting permutations of the stiffness criteria $\geq 40\%$ and weight criteria $\geq 40\%$, providing a total of 21 weighting strategies to be analysed. DCFP fibre architectures are ranked according to their frequency of producing a 'top 5' TOPSIS score. It is worth noting that this case study aims to deliver a design with maximised stiffness and minimised weight, which differs from maximised specific stiffness (specific stiffness indicates the ratio between the stiffness and weight, but not necessarily the actual levels of stiffness or weight).

The overall top 5 options for scenario 1 are compared in Figure 5-7, where data are normalised with respect to Option 1 (3k, 50mm DCFP at 40% volume fraction and 4mm thickness). The material properties for Option 1 are provided in Table 5-1. According to Figure 5-7, the top 5 fibre architectures unsurprisingly use 3k and 6k tows because of their high specific stiffness. Results also show a definite tendency for using higher fibre volume fractions (40%) and thicker sections (4mm), as increasing the volume fraction effectively increases the stiffness to weight ratio of the material, as the Young's modulus for carbon fibre is generally 40 times higher than that for epoxy resin, but the density is only 50% higher.

The spare wheel well manufactured from Option 1 in Figure 5-7 gives a total strain energy of 305.1J and a maximum deflection of 0.92mm. By locally varying the areal mass and thickness distribution by structural optimisation, the optimised fibre architecture (presented in Figure 5-9) with the same weight and material cost can achieve a 45.5% reduction in strain energy and 46.6% reduction in maximum deflection compare with the un-optimised model. Specific stiffness of the optimised model is 4 times higher than that of the glass/carbon design, and 2.9 times higher than the continuous carbon option. However, the current model is not acceptable for replacing the continuous fibre designs due to excessive weight and cost (57.4% heavier than the glass/carbon option and 1.8

times higher material cost than the continuous carbon option). This demonstrates the need for imposing limits on the overall cost and weight.

Weight and cost restrictions are implemented for Scenario 2 by imposing limits during the TOPSIS material selection process. Fibre architectures are re-assessed using the weighting strategies in Scenario 1 and the overall top 5 are compared in Figure 5-8.

The top 5 materials are still dominated by 3k and 6k DCFPs, but the weight limit effectively restricts the material thickness to a maximum of 2.8mm. According to Figure 5-8, there is a general trend of decreased TOPSIS score as thickness increases from 2mm to 2.8mm, as the score is affected by the increase in weight more than the increase in stiffness. Therefore, restricting the areal weight moves the top 5 options towards the smallest thickness (2mm). The cost restriction on the other hand, limits the volume fraction to a maximum of 30% for 3k DCFPs, and a maximum of 35% for 6k DCFP. Comparisons between Options 1 and 2 and Options 4 and 5 still suggest that larger volume fractions are preferable.

The spare wheel well manufactured from Option 1 in Figure 5-8 has 1710.32J total strain energy and a maximum deflection of 5.08mm. By optimising the fibre distribution, the stiffness has been improved by 38.5% (to 1059.8J) and the maximum deflection is reduced by 43.9% (to 2.85mm). The optimised fibre architecture is presented in Figure 5-9. The stiffness of the optimised model is 12.8% higher than that of the original glass/carbon design, and offers 9.6% weight saving and 12.4% cost saving, therefore is considered to be a better replacement for the glass/carbon NCF hybrid than a carbon NCF in the current context.

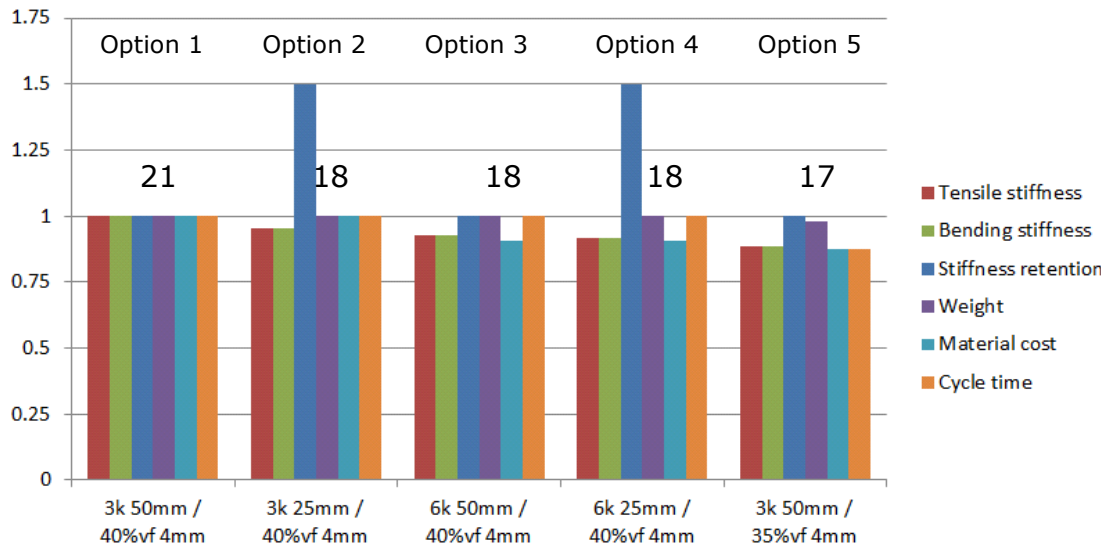


Figure 5-7: Comparison of top five fibre architectures for Scenario 1: high stiffness, lightweight without design limits. Values on the top indicate the number of times each option is ranked in the top five. Vertical axis values are normalised to the best option (3k 50mm / 40%vf 4mm).

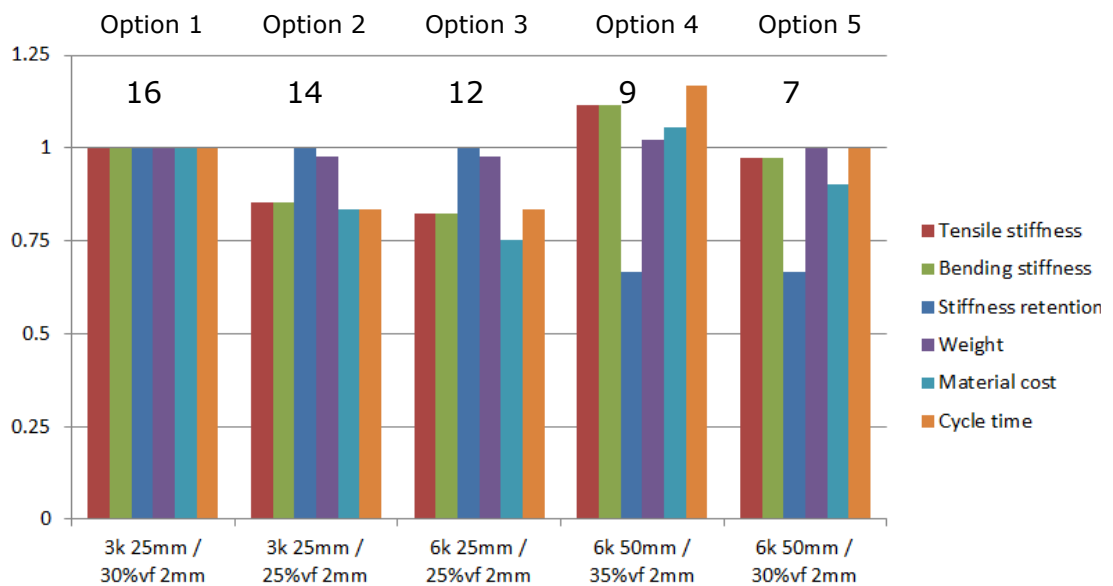


Figure 5-8: Comparison of top five fibre architectures for Scenario 2: high stiffness, lightweight with weight and cost limits. Values on the top indicate the number of permutations that each option is ranked as one of the top five options. Vertical axis values are normalised to the best option (3k 25mm / 30%vf 2mm).

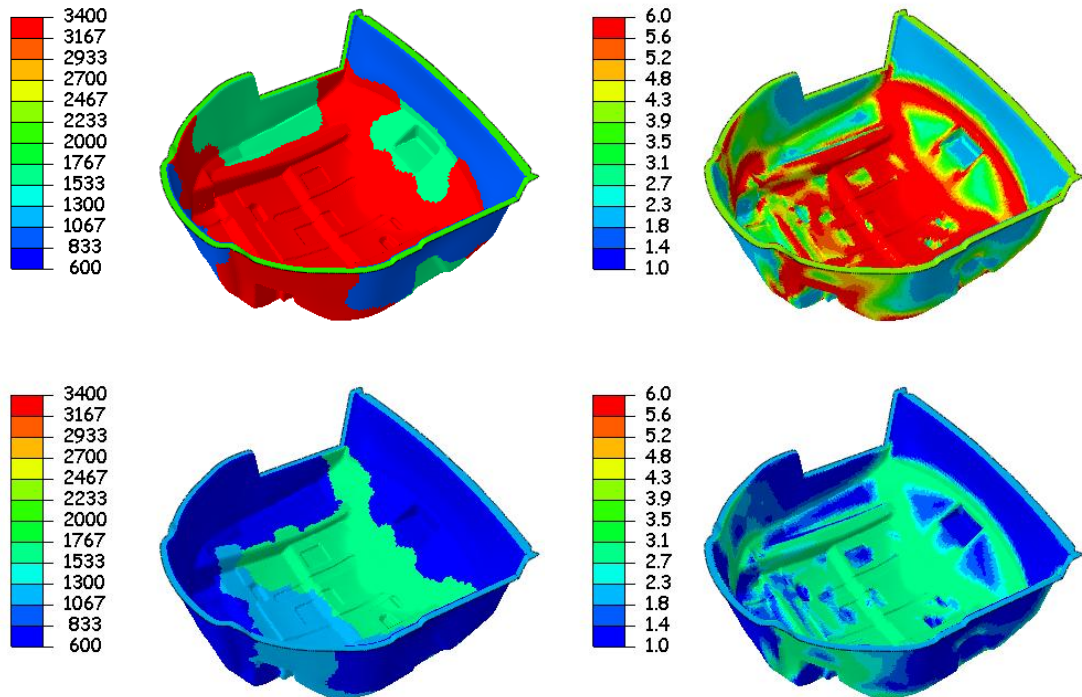


Figure 5-9: Areal mass (left column) and thickness (right column) distribution of the optimised spare wheel well for Case 1: high stiffness and lightweight. (Top row) without weight and cost limit - 3k, 50mm DCFP. (Bottom row) with weight and cost limits - 3k, 25mm DCFP.

5.4.3 Case 2: low cost

This section aims to design a high performance, lightweight part whilst keeping the cost as low as possible. This study summarises all weighting permutations with stiffness, weight and cost all equal to or greater than 30% (i.e. between 30% and 40%), which includes a total of 330 weighting strategies. The 'top 5' fibre architectures are presented in Figure 5-10, where the low cost requirement moves the material choices towards 12k and 24k fibres. The best option appears to be 12k 50mm DCFP with 30% v_f and 4mm thickness, of which the material properties are summarised in Table 5-2. In addition, the best four options are all based on 12k 50mm DCFP with 4mm thickness, with only minor differences in TOPSIS score due to the influence of varying the volume fraction.

The spare wheel well manufactured from Option 1 in Figure 5-10 gives a total strain energy of 507.8J and a maximum deflection of 1.53mm. By

locally varying the areal mass and thickness distribution by structural optimisation, the optimised fibre architecture (presented in Figure 5-12) with the same weight and material cost can achieve a 42.5% reduction in strain energy and 47% reduction in maximum deflection compare with the un-optimised model. Specific stiffness of the optimised model is 1.76 times higher than that of the glass/carbon design, and 38% higher than the continuous carbon option. However, with the same problem as Scenario 1, the current model is 50.8% heavier than the glass/carbon option, therefore cannot be accepted as a replacement design.

Weight and cost limits are imposed in Scenario 4 to prevent an overly-stiffened design, with the top 5 resulting materials presented in Figure 5-11. The top 5 materials are now dominated by 24k DCFP, except Option 4 which is 12k based. Whilst the weight limit restricts the material thickness to a maximum of 2.8mm, all 12k or 24k materials are accepted within the cost limit. Comparisons between Options 2 and 3 and Options 1 and 5 suggest that thinner sections are more preferable for this scenario, which is the same as the observation from Scenario 2.

The spare wheel well manufactured from Option 1 in Figure 5-11 has 1756.7J total strain energy and maximum deflection of 5.22mm. By optimising the fibre distribution, the stiffness has been improved by 33.7% (to 1165.9J) and the maximum deflection is reduced by 29.7% (to 3.67mm). The optimised fibre architecture is presented in Figure 5-12. The stiffness of the optimised model is 6.1% higher than that of the original glass/carbon design, and offers a 26.2% weight saving and 32.7% cost saving. This is a cost efficient solution which can clearly compete against the glass/carbon NCF design.

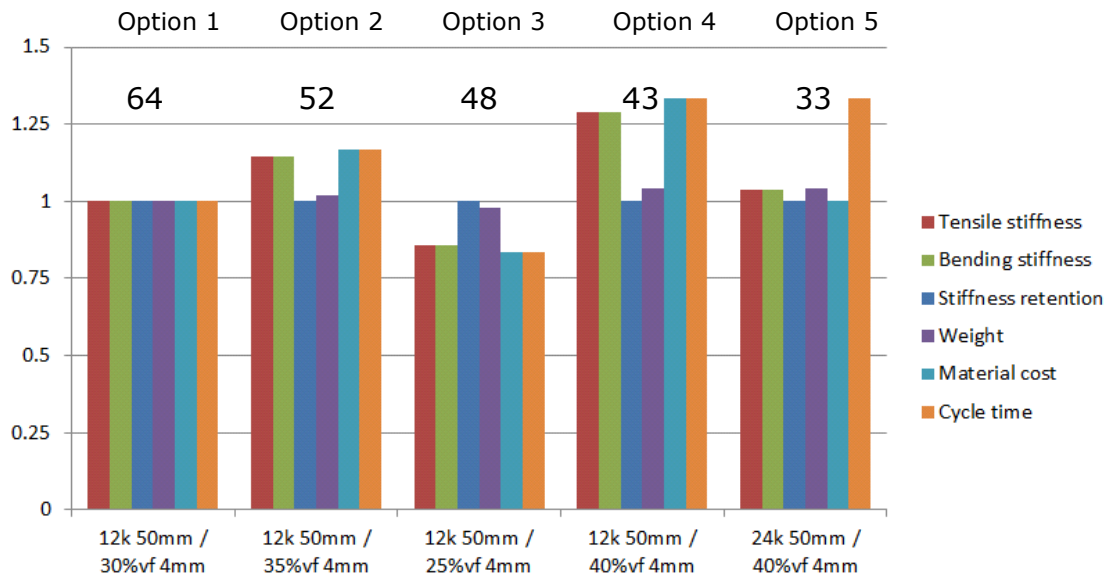


Figure 5-10: Comparison of top five fibre architectures for Scenario 3: high stiffness, lightweight and low cost (without limit). Values at the top indicate the number of times each option is ranked as one of the top five options. Vertical axis values are normalised to the best option (24k 50mm / 30% v_f 4mm).

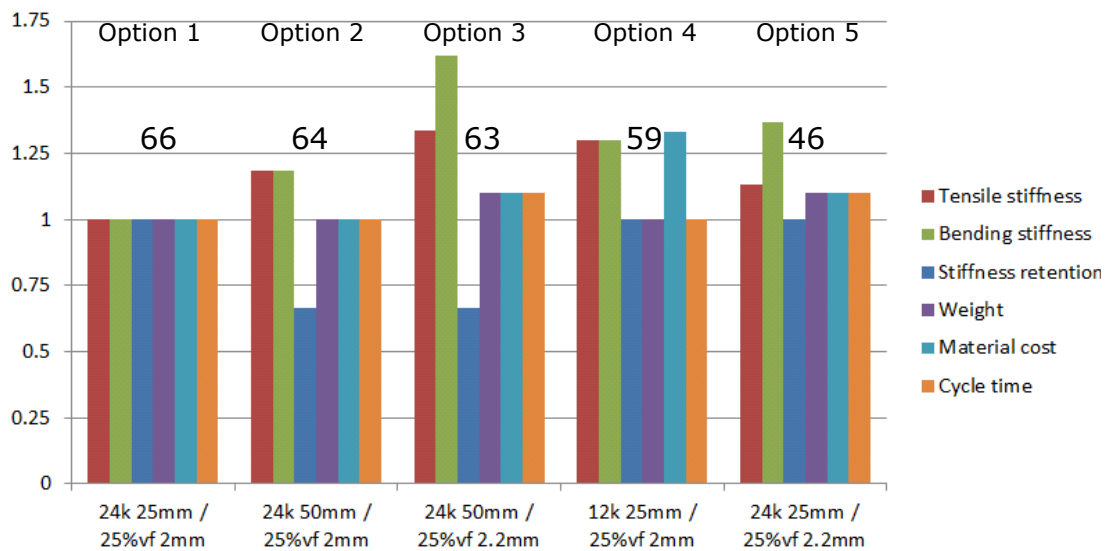


Figure 5-11: Comparison of top five fibre architectures for Scenario 4: high stiffness, lightweight and low cost (3.65kg/m² maximum weight and £54020/m² maximum material cost). Values on the top indicate the number of times that each option is ranked as one of the top five options. Vertical axis values are normalised to the best option (24k 25mm / 25% v_f 2mm).

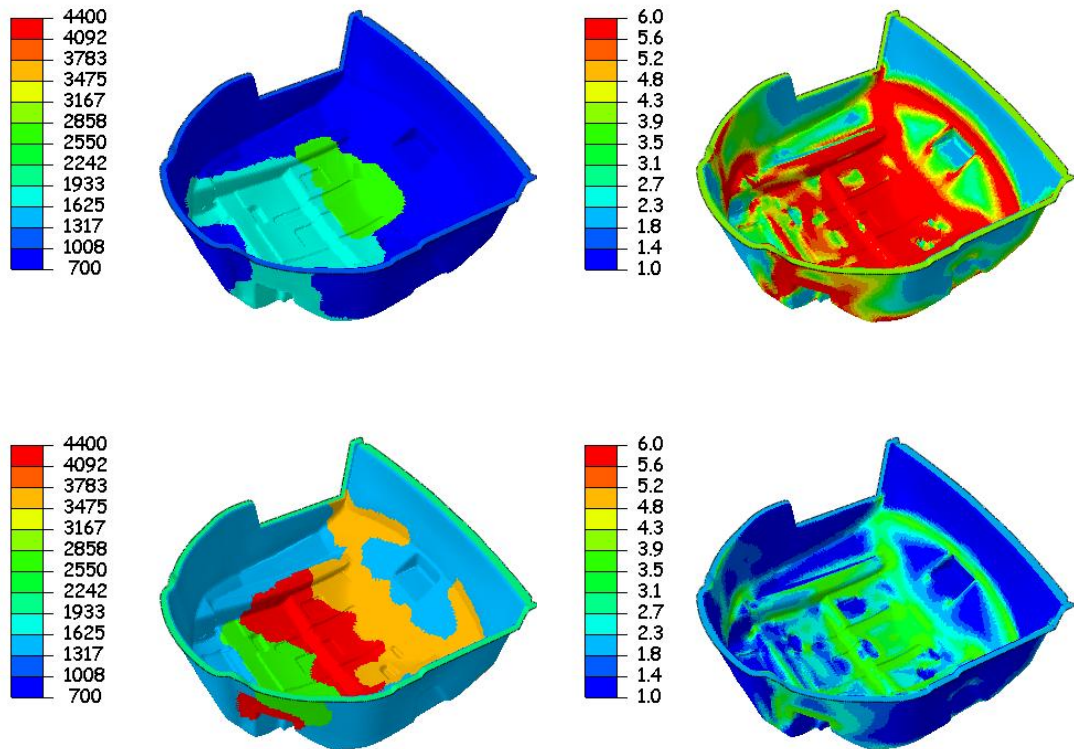


Figure 5-12: Areal mass (left column) and thickness (right column) distributions for Case 2: high specific stiffness and low cost. (Top row) without weight and cost limit - 3k, 50mm DCFP. (Bottom row) with weight and cost limits - 3k, 25mm DCFP.

5.4.4 Discussion of Models

This section discusses the suitability of replacing the glass/carbon spare wheel-well with the proposed carbon fibre options. The optimised continuous carbon and DCFP options derived from Scenarios 2 and 4 are compared in Figure 5-13 in terms of structural stiffness, weight and material cost (where the stiffness is calculated from the inverse of strain energy for each model). Moving towards a continuous all-carbon NCF solution over the glass/carbon NCF hybrid improves the stiffness by 37%, and reduces weight by 17%. Whilst this is an attractive solution, the cost of UD laminates is 1.7 times higher than the glass/carbon option, which currently prevents this from being commercially viable. In comparison, the specific stiffness of DCFP Scenario 2 is just 8% lower than that of the continuous carbon option, but it still exceeds the stiffness of the glass/carbon benchmark, for a material cost which is 12.4% lower than the all-carbon NCF solution. It should be noted that this study only

considers the cost of material in the mould, with no account made for material wastage in the raw material cost. This suggests that there is still potential for higher cost savings when using high performance 3k DCFP over carbon fibre NCF. In addition, the manufacturing cost is expected to be much lower for the DCFP option, according to [24], as it requires less touch labour and the manufacturing cycle time is also much shorter.

Switching to a low cost DCFP solution using 24k fibres results in a 7.2% reduction in specific stiffness compared with the 3k solution. Whilst the overall stiffness of the 24k DCFP solution derived in Scenario 4 is very close to that of the glass/carbon benchmark, 24k DCFP offers a 27% weight reduction and 43% cost saving over the original counterpart, which makes it a more justifiable replacement for the glass/carbon NCF design.

This study has shown that it is possible to produce a structure from optimised DCFP that has stiffness levels approaching a continuous carbon fibre non-crimp fabric, but at cost levels typically associated with lower performance glass fibre materials.

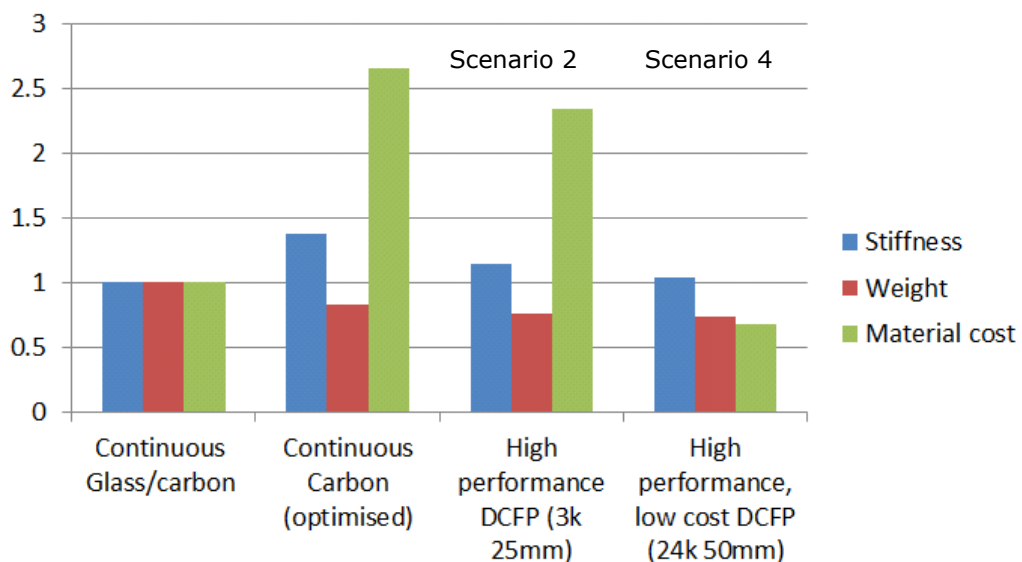


Figure 5-13: Comparison of the carbon fibre models against the original glass/carbon design. Stiffness is compared as the inverse of total strain energy. All values are normalised to the continuous glass/carbon model.

5.5 Conclusions

This chapter assessed the properties of DCFP materials from a structural designers' perspective. By adopting a material selection strategy and the structural optimisation tool, the weight and cost saving potentials for DCFP have been explored, and the flexibility of the fibre architecture has been demonstrated.

The optimisation method has been demonstrated using a spare wheel well model. The component was originally designed with laminated carbon and glass fibre composites. An alternative all-carbon fibre NCF version is proposed as a lightweight replacement for the original design, but the cost of continuous carbon is significantly higher. As a form of compromise, two DCFP options are derived by optimising the fibre architecture based on the most appropriate available option within the material database. The DCFP options aim to have comparable stiffness with the continuous fibre options, therefore weight and cost limits must be imposed during material selection to prevent an overly stiffened design.

The first DCFP design uses high performance 3k fibre to compete with the continuous carbon option, and the other uses 24k fibre to provide a low cost option with compromised specific stiffness. Results suggest that the 3k option can produce performance levels and weight savings at comparable cost to the continuous carbon option, with further benefits of low material wastage and reduced manufacturing costs. The 24k DCFP option is also shown to be a viable option, in terms of high specific stiffness and low cost compared with the textile benchmarks. Therefore, the use of DCFP materials can not only provide direct substitutes for continuous carbon fibre composites in high performance designs, but can also extend the application of composites into new areas where cost has previously been prohibitive.

Chapter 6. Thesis Conclusions

The aim of this chapter is to present the major conclusions established during this work. This thesis is primarily concerned with providing a better understanding of the variability of discontinuous fibre composites, damage tolerance and how these materials can be effectively used for designing highly optimised components for automotive applications. This chapter is split into three main sections outlining findings from material characterisation studies, the development of an optimisation algorithm, and finally suggestions for future work in this field.

6.1 DCFP material properties

6.1.1 Representative volume elements for elastic properties prediction

High levels of heterogeneity can lead to large variations in mechanical performance for discontinuous fibre composites. A greater number of test repeats are often required to achieve representative average properties with sufficient confidence, compared with textile composites. In addition to this, size effects are commonly experienced for this type of material, as material properties can vary with specimen volume. Numerical modelling can be used to reduce the dependency on experimental testing and to provide an insight into the number of repeats needed for different specimen sizes, and the minimum specimen size required to obtain representative properties.

A Representative Volume Element (RVE) is the minimum volume of material for which kinetic macroscopic variables (such as stress) are not dependent on specimen volume. A 2D finite element model has been developed to predict the stress/strain response of discontinuous fibre composites. A series of simplified 2D RVE models have been created and studied in this thesis, in order to determine the relationship between the critical RVE size and fibre length and volume fraction. All models are

subjected to periodic boundary conditions, but average properties are extracted from an inner region offset from the model boundary by a distance equivalent to two fibre lengths. According to Saint-Venant's principle, this offset removes the uncertainty associated with the approximate boundary conditions. A statistical stopping criterion has been adopted to determine the number of realisations required to achieve a representative set of elastic properties for each fibre architecture. The critical RVE side length is shown to be approximately 4 times the fibre length when considering convergence of the tensile and shear stiffnesses for the range of fibre lengths and volume fractions studied.

6.1.2 Damage tolerance

Although DCFP applications have less demanding strength requirements compare with textile composites, notch sensitivity is still of concern for semi-structural applications, where notched features often exist. Understanding the notch sensitivity of discontinuous fibre composites is a particular challenge due to the lack of testing standard and well documented threshold for the onset of notch sensitivity.

Two studies have been completed in this thesis in order to identify a reliable method to determine the onset of notch sensitivity, where the critical threshold is defined as 85% net strength of the un-notched strength of the same specimen size. The first study investigated the influence of using a constant specimen width with increasing hole size, while the second study used a constant hole-to-width ratio for increasing widths. The notched tensile performance of a discontinuous carbon fibre/epoxy DCFP material has been compared against a quasi-isotropic non-crimp fabric of the same fibre volume fraction.

In both studies, DCFP material is found to be notch insensitive. The net strength remained above the threshold of 85% un-notched strength for all specimen types, and gross section failures were observed for smaller hole sizes. In comparison, the NCF material was found by both studies to be notch sensitive.

Fracture models were also adopted to predict the notched strength of specimens, based on the results from the constant width study. Digital Image Correlation (DIC) techniques were applied to verify the suitability of using isotropic failure criteria for both DCFP and NCF materials. Predictions for notched tensile strength were within $\sim 1\%$ of experimental values for both materials.

6.2 Structural optimisation

6.2.1 Stiffness optimisation methodology

A stiffness optimisation method has been developed to locally vary the thickness and areal mass distribution for a DCFP component. The model is based on an optimality criterion approach for concurrently optimising multiple design variables. A segmentation algorithm has been implemented to divide the resulting fibre architecture into several zones of similar areal mass, where the size and shape of each zone is optimised to suit the precision of the DCFP fibre deposition process.

The optimisation algorithm has been demonstrated using a flat rectangular plate with three holes. Results suggest that the current method can effectively improve the stiffness of the component without sacrificing weight-saving potential or adding additional cost over the original DCFP benchmark. The subsequent segmentation model delivers a modified areal mass mapping realistic from the manufacturing perspective of view. Sensitivity analysis of model segmentation suggests that the stiffness reduction resultant from model segmentation is less than 10%, which has little impact on the optimality of the model.

6.2.2 Structural optimisation case study

An automotive spare wheel well has been selected to further demonstrate the benefit of using structural optimisation tool in DCFP design. The production component is manufactured from a combination of glass and carbon fibre non-crimp fabrics. A continuous all-carbon

replacement with manually optimised ply arrangement offers 65% higher specific stiffness but the material cost is also significantly (1.65 times) higher. Two DCFP options have been derived by optimising the fibre architectures based on the most appropriate materials selected from the material database. A TOPSIS technique has been adopted to choose fibre architectures according to predefined weight, stiffness and cost requirements. A DCFP material comprising 3K tows at a length of 25mm has been shown to achieve a comparable specific stiffness to the continuous carbon NCF option at the same material cost level, with the potential for further cost savings from lower wastage and manufacturing costs. A 24k, 50mm DCFP option has also been proposed as a low cost alternative. Whilst the specific stiffness of the 24k model is slightly lower (14% lower than the continuous carbon and 7% lower than the 3k DCFP option), the material cost is even lower than the glass/carbon option. Results from this study have shown that it is possible to produce a structure from optimised DCFP with stiffness levels approaching a continuous carbon fibre non-crimp fabric, but at cost levels typically associated with lower performance glass fibre materials. These aggressive cost and weight savings would not have been possible without the stiffness optimisation algorithm.

6.2.3 Structural optimisation in DCFP design

The spare wheel well case study not only demonstrates the weight and cost saving potential of using DCFP materials, but also the flexibility in material choice and manufacturing strategy. These advantages of DCFP materials cannot be fully exploited previously due to the lack of DCFP structural design tool in, and by using the optimisation method developed in this thesis, DCFP design does not have to be restricted by the metal and textile design rules. Furthermore, thickness areal mass map delivered from the current model can be directly used to determine the geometry of the liquid moulding tool, and the fibre deposition route for preform manufacturing, therefore successfully bridges the gap between the material properties study and the manufacturing process.

6.3 Future work

A damage model for DCFP will be developed based on the current meso-scale RVE model. Strength predictions for discontinuous fibre composites are challenging compared with continuous fibre composites due to the complicated failure mechanism (fibre dominated/matrix dominated) and the localised stress concentration caused by the heterogeneous nature of the material. On the other hand, the failure propagation process differs from that of isotropic and orthotropic material due to the fibre bridging behaviour. An energy based approach is therefore needed to understand the fracture mechanics of this material. The development of a damage model will also enable the notched behaviour of DCFP to be studied without extensive experimental testing, for instance to understand the effects of changing fibre length/tow size.

In terms of the structural optimisation process, further work could include the following:

1. Automated material selection. The current material selection model requires the fibre length and tow size to be pre-selected, where only the fibre areal mass is evaluated by the optimisation. Automated material selection could be implemented by pre-screening suitable fibre length and tow size for the material selection process. The material screening will choose the range of fibres that can satisfy the thickness and modulus distribution from the initial optimisation results.
2. Develop a multi-objective optimisation routine. Current optimisation methods prioritise structural stiffness maximisation. Although the overall weight and cost can be reduced with optimised fibre layout, the level of reduction is determined by the initial guess of the part thickness and modulus. This route for weight and cost saving follows heuristic rules, such that the final design is not fully optimised in terms of weight and cost minimisation. A multi-objective optimisation routine would enable the structure stiffness, overall weight and cost to be optimised at

the same time, according to user specified weightings for each objective.

3. Consider multiple load-cases. The performance of real automotive components is usually assessed with multiple criteria, for instance structural stiffness which relates to the ride and handling performance, impact resistance which relates to the crash performance, and the natural frequency which relates to the NVH performance. The idea is similar with multi-objective optimisation where the load cases can be weighted prior to the optimisation process. However, multiple load-cases optimisation is more difficult than multi-objective optimisation from a stress analysis point of view, as different load cases normally require different problem formulations to be considered.
4. Integration with process simulation. The current optimisation method assumes idealised fibre coverage, and hence idealised material properties. In practice, the quality of fibre coverage may vary depending on the tow size and fibre length. The tool geometry is also an important factor, for instance inclined or vertical surfaces are less likely to have uniform fibre distribution. Further developments can be made by considering the inter-preform fibre areal mass variation in the optimisation model, which offers more reliable prediction of the structural performance.

Appendices

Appendix A. List of publications

Journal Publications

1. **'Notched behaviour of discontinuous carbon fibre composites: Comparison with quasi-isotropic non-crimp fabric'**, C Qian, L T Harper, T A Turner, N A Warrior, Composites Part A: Applied Science and Manufacturing, Volume 42, Issue 3, March 2011, Pages 293-302
2. **'Representative Volume Elements for Discontinuous Carbon Fibre Composites. Part 1: Boundary Conditions Composites Science and Technology'**, L T Harper, C Qian, T A Turner, S Li, N A Warrior, Composites Science and Technology, Volume 72, Issue 2, Pages 225-234
3. **'Representative Volume Elements for Discontinuous Carbon Fibre Composites. Part 2: Determining the critical size Composites Science and Technology'**, L T Harper, C Qian, T A Turner, S Li, N A Warrior, Composites Science and Technology, Volume 72, Issue 2, Pages 204-210
4. **'Establishing Size Effects in Discontinuous Fibre Composites Using 2D Finite Element Analysis'**, C Qian, L T Harper, T A Turner, S Li, N A Warrior, Computational Materials Science, Volume 64, November 2012, Pages 106-111
5. **'Finite Element Modelling of the Flexural Performance of Resorbable Phosphate Glass Fibre Reinforced PLA Composite Bone Plates'**, L T Harper, I Ahmed, R M Felfel and C Qian, Journal of the Mechanical Behavior of Biomedical Materials, Volume 15 (2012), Pages 13-23
6. **'Structural Optimisation of Random Discontinuous Fibre Composites: Part 1 – Methodology'**, C C Qian, L T Harper, T A Turner, N A Warrior, Composites Part A: Applied Science and Manufacturing, Under review
7. **'Structural Optimisation of Random Discontinuous Fibre Composites: Part 2 - Case study'**, C C Qian, L T Harper, T A Turner, N A Warrior, Composites Part A: Applied Science and Manufacturing, Under review

Conference Proceedings

1. **'Determination of the size of representative volume elements for discontinuous fibre composites'**, C Qian, L T Harper, T A Turner, S Li, N A Warrior, 18th International Conference on Composite Materials, Jeju Island, South Korea, August 2011.
2. **'Determination of the size of representative volume elements for discontinuous fibre composites'**, C Qian, L T Harper, T A Turner, S Li, N A Warrior, 21st International Workshop on Computational Mechanics of Materials, University of Limerick, Ireland, August 2011.
3. **'Structural optimisation of 3D components manufactured by the Directed Carbon Fibre Preforming Process'**, C Qian, L T Harper, T A Turner, N A Warrior, 15th European Conference on Composite Materials (ECCM15), Venice, Italy, June 2012.
4. **'Structural Optimisation of Discontinuous Fiber Composites'**, C Qian, L T Harper, T A Turner, N A Warrior, 19th International Conference on Composite Materials (ICCM 19), Montreal, Canada, August 2013.

Appendix B. Additional studies for meso-scale RVE modelling

B.1. Comparison of embedded element technique vs. free mesh technique

A comparison of elastic constants is made to understand the effect of using the embedded element technique versus a more conventional unstructured meshing approach. The *TIE command is used to constrain the fibres to the matrix at coincident nodes in the unstructured meshed model, assuming perfect interfacial bonding.

The beam elements are of a constant 0.2mm length in both models. The edge length of the matrix elements in the embedded model are also 0.2mm for a rigorous comparison.

Figure B-1 shows that the stress fields and the displaced shapes are identical for the two meshing approaches for three different load cases; in-plane tension in the 1 and 2 directions and in-plane shear. Table B-1 shows that there is less than 1% error between the two approaches when comparing the in-plane moduli and Poisson's ratios. This error can be partially attributed to mesh density, which will be discussed further in Appendices B.2. These low errors are considered to be acceptable in the current context, since this approach eliminates problems with mesh density and distorted elements around fibre crossover points.

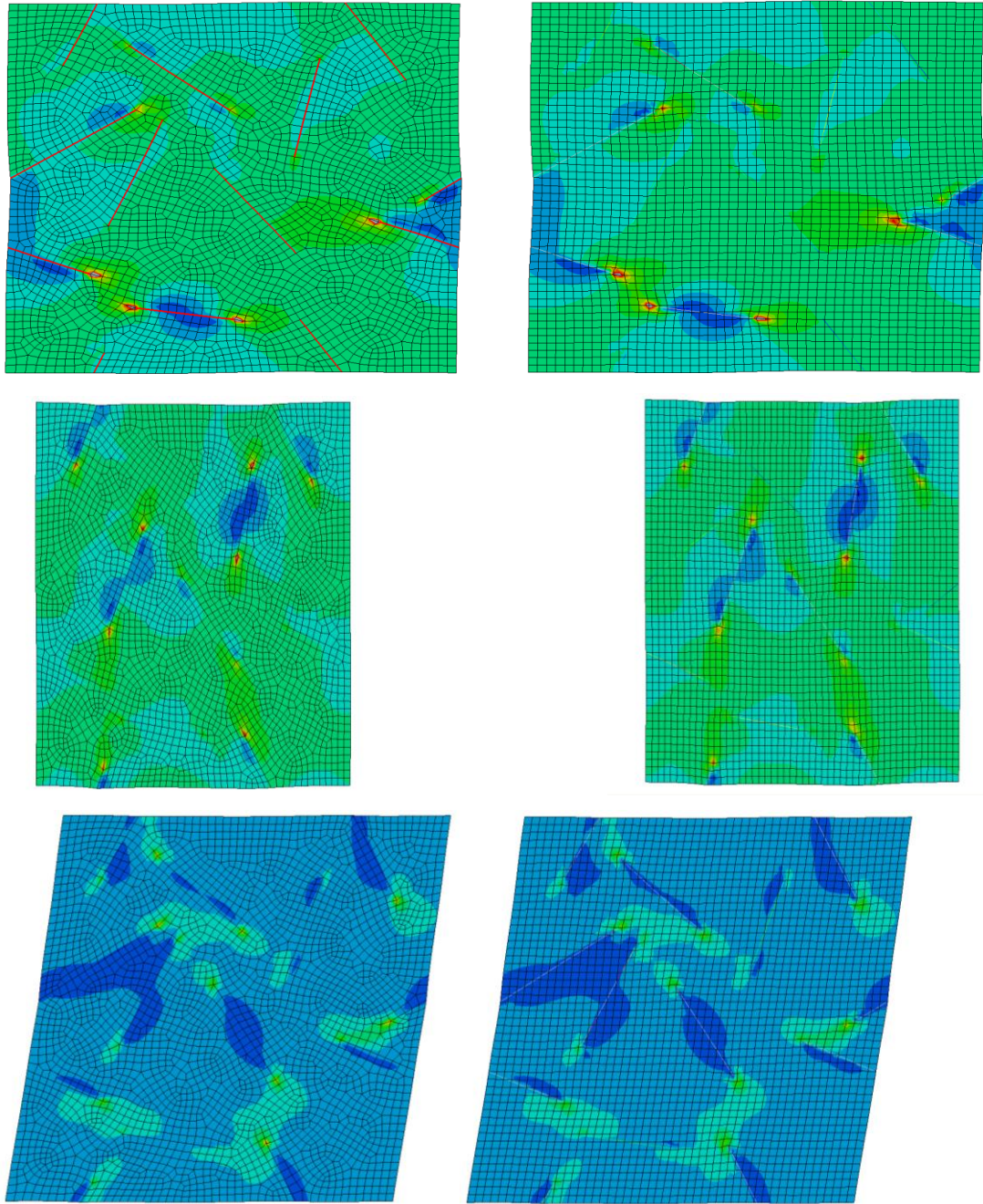


Figure B-1: Von Mises stress comparison between a model using an unstructured mesh with tie constraints (left) compared with structured embedded elements (right). From top to bottom; Tensile 1, Tensile 2 & Shear 1-2 loading. (Fibres are highlighted in red in the top left image and all images are scaled to the same peak stress). Deformation factor is 15 in all cases.

Table B-1: Error between free mesh method and embedded element method for three load cases presented in Figure B-1.

	Embedded Mesh	Free Mesh	Error (%)
E₁₁ (MPa)	3651.2	3632.6	0.512
v₁₂	0.400	0.400	0.131
E₂₂ (MPa)	3537.6	3521.2	0.465
v₂₁	0.388	0.387	0.085
G₁₂ (MPa)	1426.3	1413.1	0.936

B.2. Mesh density analysis

The sensitivity of the stress field to the density of the finite element mesh has been studied using the embedded element technique. A 1:1 ratio for resin element edge length to fibre element length was maintained for all models, ranging from 2mm down to 0.0125mm. The same random seed was specified in the RVE generator to produce identical fibre architectures on repeat runs of the model. A 20mm×20mm model was created for each scenario and periodic boundary conditions were applied.

Figure B-2 shows that the average RVE stress takes longer to converge for higher fibre volume fractions. A greater number of embedded beam elements share the same host elements at higher volume fractions; therefore the mesh needs to be finer to account for the increased number of bundle ends and crossover points. (This is also true for coupons of increasing thickness because of the planar 2D architecture created by the RSA model). The error for the average RVE stress between an element length of 0.05mm and 0.0125mm is less than 1% in all cases: 0.27% for 10% v_f , 0.58% for 30% v_f and 0.84% for 50% v_f .

The local stress distribution along the length of an arbitrary fibre is included in Figure B-3 for the 30% fibre volume fraction case. The same trend is observed at this local scale as for the global average. The stress values along the fibre are within $\sim 0.5\%$ when comparing 0.05mm elements with the 0.0125mm case. An element length of 0.05mm has been used for all subsequent models.

Given the finite lengths of the fibres involved, a degree of discontinuity in material properties is expected at the fibre ends. Stress concentrations are reflected in the FE results around the fibre tips, which are as expected in practice. It is beyond the scope of the present thesis to prove whether there exists a mathematical stress singularity at a fibre tip. However, if the conclusions of [134] could be extended, one might expect that the singularity would emerge only if the stiffness of the fibre vanished, i.e. creating a virtual crack, or approached infinity, i.e. fibres

being rigid. Otherwise regular stress fields might be expected (although a stress concentration is inevitable), the degree of which would depend on the disparity between the stiffnesses of the fibre and the matrix.

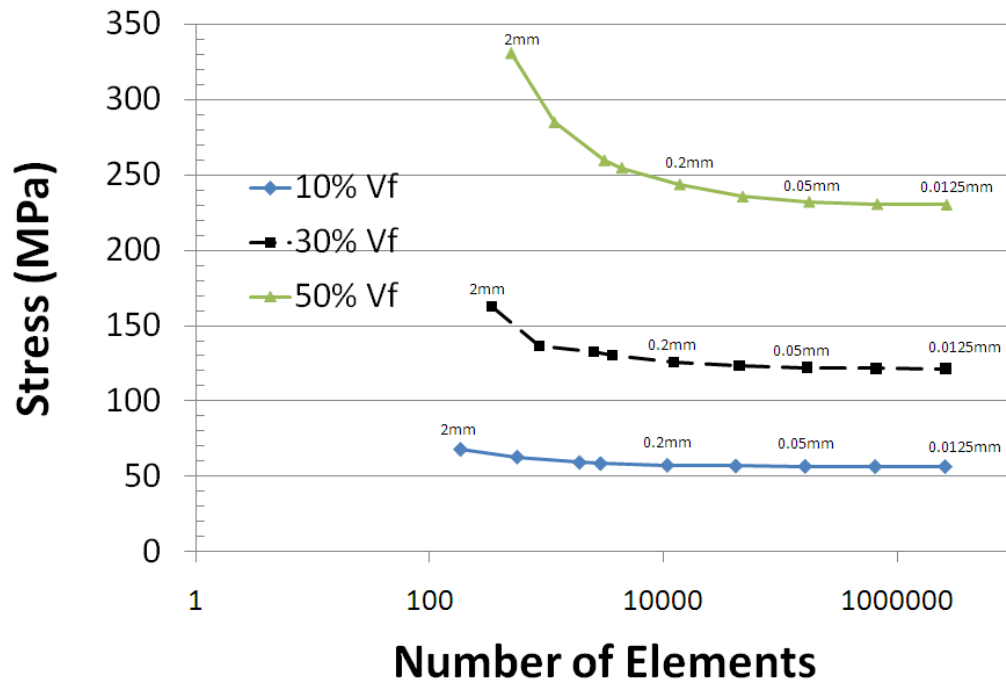


Figure B-2: Effect of mesh density for three different fibre volume fractions. Numbers inset represent the resin element edge length (which is equal to beam element length)

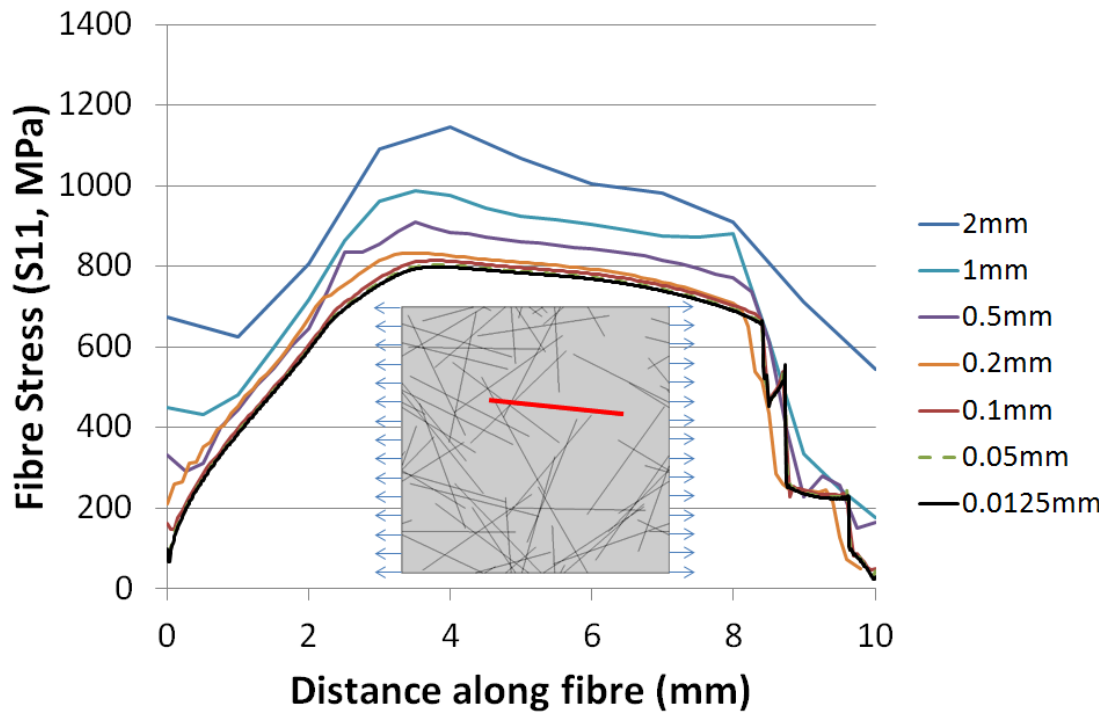


Figure B-3: Effect of mesh density on the local stress distribution (S11) along the length of an arbitrary fibre. Legend refers to element edge length.

B.3. Homogeneous approach vs. heterogeneous approach

Two modelling schemes have been investigated, exploiting Saint-Venant's principle to establish the critical decay length of the local incorrectness of the periodic boundary conditions [54]. Both schemes consist of embedded inner cells. For the first approach, fibres are distributed over both the RVE boundary and the model boundary (see Figure 2-2), which is denoted as the *heterogeneous approach*. For the second approach, fibres are only dispersed over the inner RVE boundary (Figure B-4), which is commonly known as an embedded cell approach. The outer frame consists of a homogeneous material, which is identified here as the *homogeneous approach*. The homogeneous approach is of interest because it is simpler to implement and potentially could reduce CPU time and may result in smaller models with a shorter decay length.

A selection of models used to evaluate the heterogeneous approach has been reanalysed using the homogeneous approach. The challenge using the homogeneous approach is selecting appropriate material properties for the outer region. For this study they have been obtained from the converged values from the heterogeneous model and are presented in Table B-2. Figure B-6 shows comparisons between the heterogeneous model and the homogeneous model for a 10mm fibre length at 10% v_f . In all cases the homogeneous model converges much quicker than the heterogeneous model, at approximately $d/L \approx 0.5$ (see error values Table B-2). This equates to a 90% reduction in the total number of degrees of freedom for the 10mm fibre length case, compared with the corresponding heterogeneous model. However, there is an error of up to 13% between the converged values from the two models (E_1 – 3.0% error, E_2 – 12.9% error, G_{12} – 9.2% error). This error is independent of fibre volume fraction, but dependent on the fibre length and is generally lower for shorter fibres, as shown by Table B-4. The homogeneous model provides a very good approximation for the in-plane stiffnesses for an RVE containing 2.5mm long fibres at 10% v_f (E_1 – 0.005% error, E_2 – 0.006% error, G_{12} – 0.289% error).

Figure B-5 shows a comparison of stress contours extracted from the inner RVE boundary of both modelling approaches. The images are for the transverse loading case (y-direction) and are taken from the data presented in Figure B-6 at $d/L=5$. Both models share similar internal features, such as stress concentrations at the bundle ends, but it is clear that there are additional stress perturbations at the RVE boundary for the homogeneous model. Fibres are cropped at the inner boundary for the homogeneous model, introducing an artificial fibre end, causing a stress concentration in the matrix material. The displaced shape of the homogeneous model is also affected by the local discontinuities, particularly along the top and bottom boundaries. The error between the two models for the longitudinal stiffness (E_1 in Figure B-6) is much smaller because of the distribution and orientation of fibres. The stress distributions seen in contour plots for this load case are similar because fewer fibres cross the left and right boundaries compared with the top and bottom and fewer fibres are orientated in the loading x-direction.

Whilst the homogeneous model converges at shorter decay lengths compared with the heterogeneous model, accuracy is dominated by the boundary effects around the perimeter of the RVE. Convergence of the heterogeneous model is clearly influenced by the heterogeneity of the surrounding material, but even so, it is considered to be a more reliable approximation because it eradicates the artificial stress concentrations that are present in the homogeneous model.

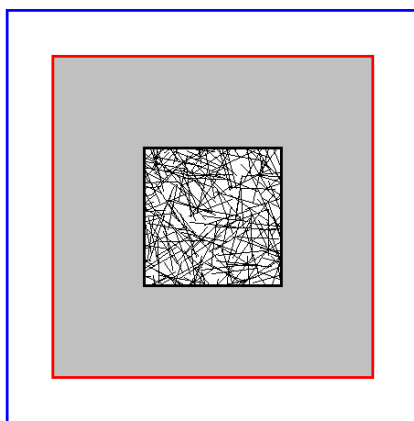


Figure B-4: Schematic of random sequential adsorption model (trimmed state) for heterogeneous approach.

Table B-2: Error values used to establish convergence of decay length for both heterogeneous and homogeneous approaches. ('d' is decay length and 'L' is fibre length).

Model type	Fibre length (mm)	v_f (%)	Architecture	RVE size (mm × mm)	Dep from Isot at $d/L = 2$	Stiffness values at $d/L = 2$			Error for $d/L = 2$ & $d/L = 5$		
						E_1 (MPa)	E_2 (MPa)	G_{12} (MPa)	E_1 (%)	E_2 (%)	G_{12} (%)
Hetero	2.5	30	Random	20 × 20	0.05	4603.3	4837.4	1687.1	-0.017	-0.080	2.027
Hetero	5	30	Random	20 × 20	0.146	6193.2	7474.1	2500.2	-0.401	0.215	-0.408
Hetero	10	30	Random	20 × 20	0.406	7542.1	10195.1	3672.6	-0.292	1.775	1.516
Hetero	2.5	10	Random	20 × 20	0	3704.4	3788.4	1343.1	-0.060	0.187	1.452
Hetero	2.5	30	Random	20 × 20	0.05	4603.3	4837.4	1687.1	-0.017	-0.080	2.027
Hetero	2.5	50	Random	20 × 20	0.113	6170.1	5510.6	2341.1	658	-0.144	0.797
Hetero	10	10	Random	20 × 20	0.223	4527.4	5576.4	1881.4	-0.911	0.415	-0.962
Hetero	10	30	Random	20 × 20	0.406	7542.1	10195.1	3672.6	-0.292	1.775	1.516
Hetero	10	50	Random	20 × 20	0.052	23466.8	23785.3	7822.8	-0.063	0.703	0.651
Hetero	10	30	Aligned	20 × 20	2.225	39409.3	3835.6	1492.5	-0.213	0.169	-1.462
Hetero	10	30	Random	20 × 20	0.406	7542.1	10195.1	3672.6	-0.292	1.775	1.516
Hetero	10	30	Random	20 × 20	0.406	7542.1	10195.1	3672.6	-0.292	1.775	1.516
Hetero	10	30	Random	40 × 40	0.056	11602.9	12302.5	4189.9	1592	0.705	1.189
					Dep from Isot at $d/L = 0.5$	Stiffness values at $d/L = 0.5$			Error for $d/L = 0.5$ & $d/L = 5$		
Homo	2.5	10	Random	20 × 20	0.008	3697.5	3726.9	1343.5	-0.005	0.006	0.289
Homo	2.5	50	Random	20 × 20	0.103	5952.9	5367.6	2256.2	423	0.531	1.359
Homo	10	10	Random	20 × 20	0.106	4390.7	4858.8	1708.7	546	0.088	1.535
Homo	10	30	Random	40 × 40	0.071	10710.5	11314.8	4226.1	126	1.012	0.746

Table B-3: Material properties used for the homogeneous regions.

Model type	Fibre Length (mm)	v_f (%)	Architecture	RVE size (mm x mm)	E_1 (MPa)	E_2 (MPa)	v_{12}	G_{12} (MPa)
Homo	2.5	10	Random	20 x 20	3699	3742	0.375	1360
Homo	2.5	50	Random	20 x 20	6187	5495	0.372	2352
Homo	10	10	Random	20 x 20	4487	5600	0.328	1863
Homo	10	30	Random	40 x 40	11679	12339	0.342	4192

Table B-4: Percentage error values between the heterogeneous and homogeneous approaches. Stiffness values were taken from the point of convergence ($d/l=2$ for heterogenous and $d/l=0.5$ for homogeneous).

Fibre Length (mm)	v_f (%)	Architecture	RVE size (mm x mm)	Error (%) between hetero & homo		
				E_1	E_2	G_{12}
2.5	10	Random	20 x 20	0.19	0.17	-0.03
2.5	50	Random	20 x 20	-3.52	-2.6	-3.62
10	10	Random	20 x 20	-3.02	-12.87	-9.18
10	30	Random	40 x 40	-11.83	-9.69	0.98

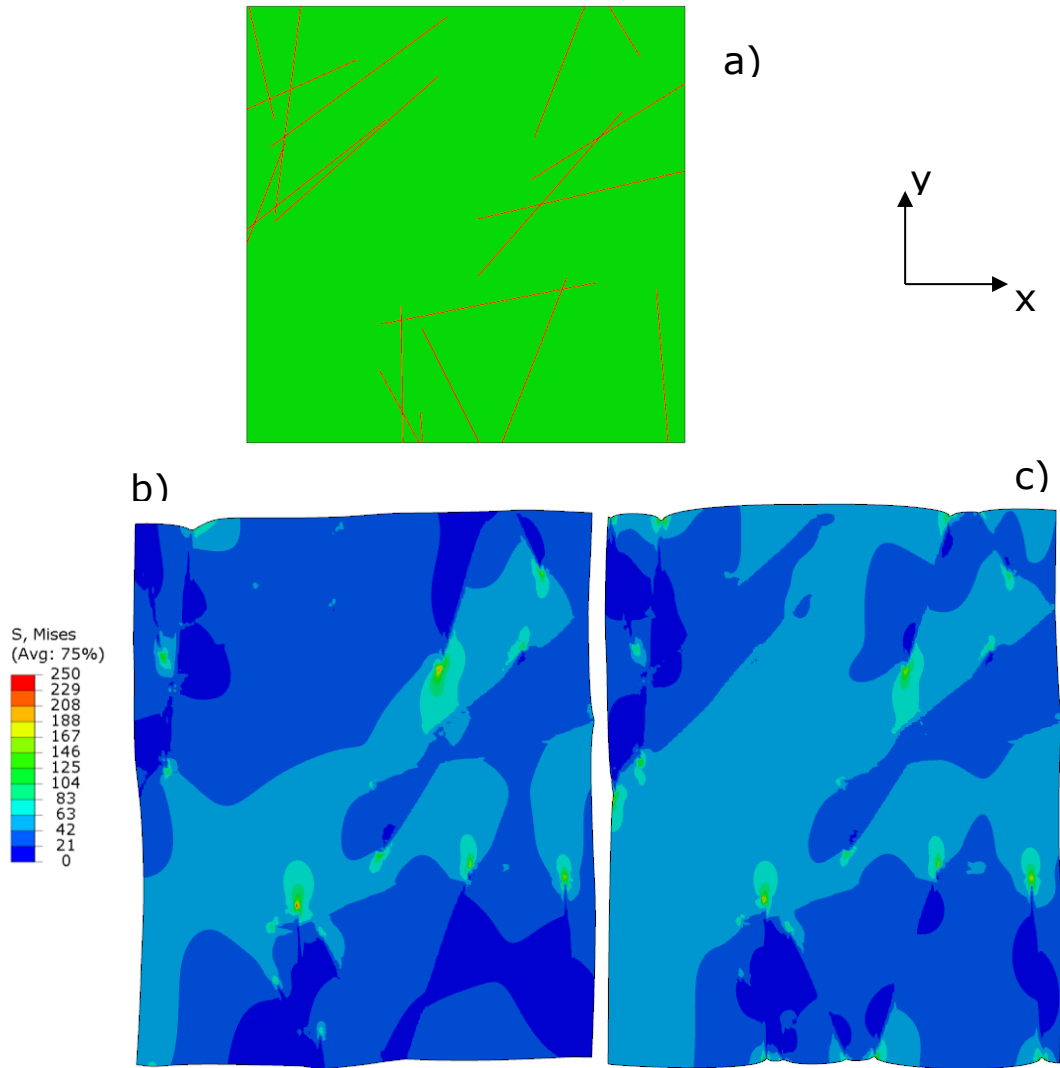


Figure B-5: Comparison of Von Mises stress contour plots for an RVE containing 10mm long fibres at 10% vf. a) Undeformed shape showing the fibre distribution, b) deformed shape from heterogeneous model, c) deformed shape from homogeneous model. Loading was in the y-direction and the deformation scale factor is 15. All stresses are scaled between 0 and 250MPa.

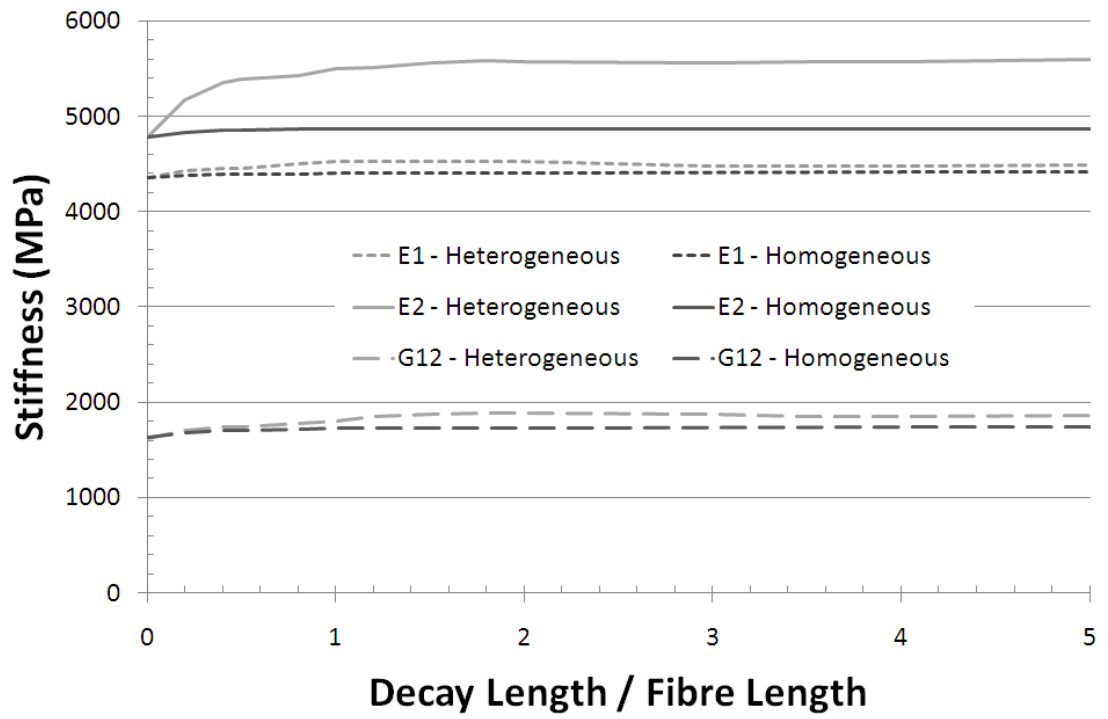


Figure B-6: Decay length study for two different embedded cell approaches. 10mm fibre length, 10% v_f .

B.4. Summary of results

Table B-5: Average results for E_1 . Standard deviation presented in parentheses. The total number of realisations is shown, and the required calculated number for 5% relative error is also shown.

Architecture (fibre length, v_f)	RVE edge length (mm)	Actual number of realisations	Average degrees of freedom per model	E_1 (MPa)	Realisations for ϵ rel = 5%
5 mm, 50%	5	315	131,274	14,398 (6386)	315
5 mm, 50%	10	139	188,678	14,421 (3727)	107
5 mm, 50%	15	89	256,528	13,834 (2263)	43
5 mm, 50%	20	74	334,695	13,576 (1720)	26
5 mm, 50%	30	59	522,376	13,393 (930)	8
5 mm, 50%	40	24	751,646	13,721 (632)	3
5 mm, 50%	50	26	1,022,613	13,392 (597)	3
2.5 mm, 30%	2.5	79	30,501	4745 (968)	67
2.5 mm, 30%	5	35	40,883	4721 (596)	25
2.5 mm, 30%	7.5	35	58,292	4673 (499)	18
2.5 mm, 30%	10	26	72,361	4683 (220)	4
2.5 mm, 30%	20	12	162,149	4687 (151)	2
2.5 mm, 30%	50	10	645,773	4713 (51)	1
2.5 mm, 30%	80	2	1,451,087	4725 (47)	1
5 mm, 30%	5	270	116,625	9449 (3879)	270
5 mm, 30%	10	75	167,744	8295 (1658)	64
5 mm, 30%	15	35	228,058	7968 (823)	17
5 mm, 30%	20	35	297,537	7880 (743)	14
5 mm, 30%	30	35	464,281	7882 (495)	6
5 mm, 30%	40	35	668,111	7847 (350)	3
5 mm, 30%	50	28	908,619	7862 (270)	2
10 mm, 30%	10	211	463,480	12,671 (4599)	211
10 mm, 30%	20	61	666,698	12,169 (2170)	51
10 mm, 30%	30	57	906,909	12,173 (1492)	24
10 mm, 30%	40	25	1,184,158	12,227 (1168)	15
10 mm, 30%	50	25	1,498,145	12,062 (1267)	18
10 mm, 30%	60	14	1,849,119	12,025 (370)	2
10 mm, 30%	80	13	2,661,479	12,213 (301)	1

Appendix C. Experimental Methodology

C.1. Manufacture of specimens

Discontinuous fibre plaques were manufactured by a combination of DCFP and resin transfer moulding. Full details of the process and apparatus design are presented in [23] and [135]. Laboratory scale 2D preforms (600mm×400mm) were produced by depositing 30mm long fibres and binder from the chopper head, mounted 300mm above the tool surface. The robot was programmed along repeated linear paths, each offset by 50mm, starting in an east/west direction followed by a north/south layer, at 0.8m/s robot speed (1.6kg/hr). Carbon fibre was supplied by Toho Tenax GmbH, in the form of 3K HTA tows with 5631 polyurethane sizing. 6%wt Reichhold Pretex 110 thermoset powder binder was added during processing. The effective density of the preform was approximately $1.73 \times 10^3 \text{ kg/m}^3$, after taking into consideration the addition of the binder. Preforms were compacted at $2 \times 10^4 \text{ Pa}$ and cured at 150°C for 6 minutes to stabilise the structure.

Quasi-isotropic non-crimp fabric (NCF) plaques were made for comparison with a $0^\circ/+45^\circ/-45^\circ/90^\circ$ ply arrangement. Preforms were manufactured using Sigmalex 450gsm/PW-BUD/STS5631/24K/0900mm carbon fabric and 6%wt Reichhold Pretex 110 binder.

The DCFP/NCF preforms were transferred into a closed tool and injected with Gurit Prime 20Lv liquid resin, using vacuum assisted resin transfer moulding. The resin was preheated to 80°C and the tool temperature was 100°C. Parts were cured for 60 minutes in the mould tool and post-cured freestanding for 2 hours at 80°C in a fan assisted oven. Four plaques (designated A, B, C and D) were produced for each material. The target areal mass for all preforms was 1800gsm, yielding a ~40% volume fraction in a 2.6mm mould cavity. Volume fraction values are presented for all plaques in Table C-1.

Table C-1: Summary of fibre volume fractions for each plaque

Plaque	DCFP (%)	NCF (%)
A	42.2	40.3
B	43.5	39.1
C	43.1	37.3
D	42.0	37.2

C.2. Specimen Preparation

Specimens were divided into two categories and cut randomly for each material. Plaques A & B were used to investigate the effect of maintaining a constant specimen width for increasing hole diameters. Plaques C & D were used to investigate the effect of maintaining a constant hole to width ratio. Notched tensile specimens were straight sided and cut to 250mm long (including holes) using an abrasive water-jet cutter. Aluminium tabs were bonded to both ends of each specimen to prevent premature failure in the jaw area of the testing machine.

C.3. Testing procedure

Specimens were tested on an Instron 5581 universal testing machine according to BS2782: Method 326F: 1997. An extension rate of 1mm/min was used in conjunction with a sampling rate of 1Hz. Thickness and width values for stress calculations were determined by averaging values measured at five positions along the gauge length. Average tensile strain was measured using an Instron 2630-100 clip-on extensometer, with a 50mm gauge length, and 0.00254mm resolution. A Limes Vic3D Digital Image Correlation (DIC) system was also used to provide full-field strain plots in the area of interest. Tensile modulus values were evaluated in the strain range of 0.001 to 0.003 for the un-notched samples only. Modulus and UTS values were normalised to the target volume fraction of 40%, based on the actual thickness of each individual specimen.

Specimen surfaces were speckle coated with laser-printed white water-slide decal paper. The speckle pattern was optimised for post-processing to provide a uniform array of speckles, in terms of both size and spatial

distribution. Images of a 120×120mm were recorded by a stereovision system in Limes VicSnap, with cameras positioned 1.5m away from the specimen (see Table C-2 for calibration values). The system consisted of two 5.0 Megapixel CCD cameras fitted with Pentax C37500 lenses (f=75mm, 1:2.8 D), with a local displacement resolution of 0.24µm for the current set up. Specimens were illuminated by a pair of 6400K white lights during testing. Images were processed using Limes Vic3D software to calculate the full 3D displacement field. The analysis area was divided into 21×21 pixels subsets using a 3 pixels step size, such that one correlation was performed for every three pixels.

Table C-2: Calibration parameters for Vic3D stereovision system

Parameter	Camera 1	Camera 2	Camera 1→2 transformation	
Centre x (pixels)	1226	1226	Alpha (deg)	-0.18
Centre y (pixels)	1026	1026	Beta (deg)	15.59
Focal lenth x (pixels)	2415.7	24031.	Gamma (deg)	-0.22
Focal length y (pixels)	24105.7	24031.1	Tx (mm)	-276.16
Skew	-16.8357	-18.9384	Ty ()	-2.88
Kappa 1	0.553472	-0.24902	Tz (mm)	19.57
Kappa 2 & 3	0	0	Baseline (mm)	276.86

Table C-3: Experimental results for un-notched specimens. All values normalised to 40% v_f .

Material	Width (mm)	Modulus (GPa)	Mod COV (%)	UTS (MPa)	UTS COV (%)	# Samples
NCF	12.5	28.51	2.97	334.84	7.29	10
NCF	25	30.87	6.90	388.48	10.10	5
NCF	37.5	30.70	5.92	389.34	6.05	7
NCF	50	33.34	5.60	387.18	3.74	5
DCFP	12.5	31.59	13.59	207.06	27.44	11
DCFP	25	28.25	16.75	187.75	27.21	5
DCFP	37.5	31.65	19.36	245.90	18.37	10
DCFP	50	33.68	15.67	202.22	29.36	5

Table C-4: Notched gross (G) and net (N) strength for constant width study specimens. All values normalised to 40% v_f .

Material D (mm)	G UTS (MPa)	G UTS COV (%)	# Gross Fails	N UTS (MPa)	N UTS COV (%)	# Net Fails
NCF 0	389.34	6.05	7	389.34	6.05	0
NCF 3	340.03	4.84	0	368.94	4.83	6
NCF 5	278.60	4.36	0	320.95	4.37	6
NCF 7	237.81	13.54	0	291.53	13.54	6
NCF 9	222.38	11.49	0	292.54	11.40	6
NCF 14	187.53	10.28	0	299.83	10.40	5
DCFP 0	245.90	18.37	10	245.90	18.37	0
DCFP 3	192.77	24.75	6	209.50	24.74	0
DCFP 5	175.24	28.06	4	202.65	28.05	2
DCFP 7	173.54	18.08	3	213.64	18.07	3
DCFP 9	171.04	18.44	1	225.46	18.46	5
DCFP 14	151.79	11.17	0	242.77	11.16	6

Table C-5: Notched gross (G) and net (N) strength for constant ratio study specimens. All values normalised to 40% v_f . All specimens failed at the hole.

Material	W (mm)	D (mm)	G UTS (MPa)	G UTS COV (%)	N UTS (MPa)	N UTS COV (%)	# Samples
NCF	12.5	4.7	212.44	3.92	341.54	3.96	5
NCF	25	9.4	197.55	10.59	314.49	10.47	5
NCF	37.5	14	187.53	10.28	299.83	10.40	5
NCF	50	18.75	180.02	8.26	288.11	8.28	5
DCFP	12.5	4.7	206.01	20.69	333.55	20.94	5
DCFP	25	9.4	125.50	21.74	201.57	21.83	5
DCFP	37.5	14	158.02	11.17	252.63	11.16	5
DCFP	50	18.75	131.72	13.23	210.77	13.17	5

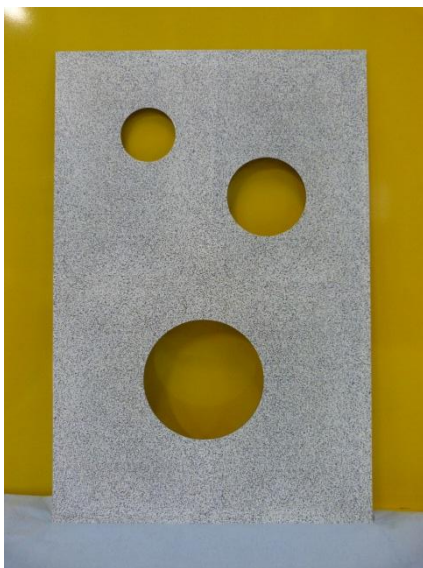
Table C-6: Comparison of predicted notched strength (relative error). Unit for strength is MPa(%).

Material	D (mm)	Test	d_0 (mm)	PSC	PWG	Kim
NCF	5	278.60	1.69	288.60 (3.59)	270.47 (-2.92)	270.50 (-2.91)
NCF	7	237.81	1.58	253.15 (6.45)	246.73 (3.75)	246.65 (3.72)
NCF	9	222.38	1.85	223.86 (0.67)	226.03 (1.64)	225.89 (1.58)
NCF	14	187.53	2.41	172.24 (-8.15)	183.67 (-2.06)	183.79 (-1.99)
DCFP	7	182.61	2.84	199.56 (9.28)	181.82 (-0.44)	181.79 (-0.45)
DCFP	9	175.32	3.50	181.97 (3.79)	176.53 (0.69)	176.57 (0.72)
DCFP	14	158.02	5.56	141.39 (-10.52)	157.62 (-0.25)	157.61 (-0.26)

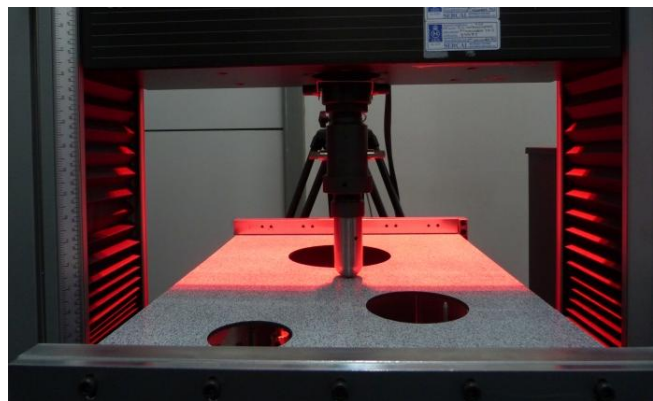
Appendix D. Demonstrator part for stiffness optimisation methodology

D.1. Model description

A 400×600mm rectangular plate with three large arbitrary circular holes (Figure D-1a) has been chosen to validate the boundary conditions used by the DCFP optimisation algorithm. Comparisons of the deflection under a point load (Figure D-1b) are made between a 4mm thick DCFP plate with uniform fibre architecture and a 2mm thick steel plate. The DCFP plate consists of 30mm long 3K tows at fibre volume fraction of 40%. The plate is simply supported along the two 400mm sides and the point load is applied at the geometric centre.



(a)



(b)

Figure D-1: Plate with three arbitrary holes: (a) geometry of the plate. (b) load configuration.

D.2. Finite element modelling

The CAD geometry of the plate is defined as a 3D conventional shell and exported into ABAQUS/CAE for mesh generation and analysis. The

geometry of the conventional shell represents the mid-surface of the plate, where the material properties and section thickness can be defined using the shell section definition. Quadratic elements (STR165) are adopted for this study, but the optimisation algorithm is capable of handling linear or non-linear conventional shell elements of any shape.

The model is subjected to a static load case using appropriate boundary conditions and is analysed in ABAQUS/Standard. The point load is applied as an equivalent pressure of 0.764MPa over a circular region of $\varnothing 10\text{mm}$, to reduce the stress singularity caused by applying a concentrated force and to match experimental methods. Isotropic material properties are adopted for all material options, where composites properties are defined by the effective linear-elastic stress-strain relationship. For the mild steel and un-optimised benchmark models, the corresponding shell section definition is assigned globally to the entire model, whereas for the optimised DCFP model, a *DISTRIBUTION TABLE is used to specify the shell thickness and the effective composites properties for each element. The material properties for the benchmark models have been obtained experimentally from tensile testing of straight sided samples, where the Young's modulus and Poisson's ratio values have been measured using digital image correlation.

Table D-1 summarises the material properties for the benchmark models and the optimised DCFP model. E_0 , t_0 denote the Young's moduli and section thicknesses of the benchmark models. A 3K tow size and 30mm fibre length have been selected for the DCFP fibre architecture, with a 30% v_f and 4mm section thickness for the un-optimised case.

Table D-1: Material properties for the structural optimisation model. Benchmark values for DCFP are taken from 3K 30mm fibre length at 30% v_f .

	E_0 (GPa)	E_{min} (GPa)	E_{max} (GPa)	Nu	t_0 (mm)	t_{min} (mm)	t_{max} (mm)	Density (Kg/m ³)
Mild steel	200	-	-	0.3	2.1	-	-	7850
DCFP	27.1	15	45	0.3	4	2	6	1230

D.3. Model validation

The indentation test was performed on an Instron 5581 universal testing machine. An extension rate of 1mm/min was used in conjunction with a sampling rate of 1Hz. The test was terminated at a peak load of 60N. Four RDP D5 400AG Linear Variable Differential Transformers (LVDTs) were placed below the plate to track the displacements of the plate at four different locations, as indicated in Figure 4-2. A Dantec Dynamics Digital Image Correlation (DIC) system was used to provide full-field displacements measure of the plate. The system consisted of 4 off 5 Megapixel CCD cameras with 28mm lenses. Due to the space limitations of the current testing setup, only half of the plate could be taken at a time, hence the same test was repeated once in order to obtain the displacement plot of the other half. The DIC calibration parameters of the test can be found in Table D-2. The surface of the plate was speckle coated with laser-printed white water-slide decal paper (see Figure D-1a). The speckle pattern used was the same as the one used in section C.2, but printed at 50% larger scale due to the larger size of the plate. The analysis area was divided into 30×30 pixels subsets using a 10 pixels step size, such that one correlation was performed for every ten pixels.

Table D-2: Calibration parameters for Dantec Dynamics DIC system

Intrinsic Parameters camera_pos_1:	
Focal length {x; y}:	{5109.1 ± 0.8; 5108.3 ± 0.8}
Principal point {x; y}:	{1205.0 ± 0.8; 1047.4 ± 0.4}
Radial distortion {r2; r4}:	{-0.2187 ± 0.0002; 0.413 ± 0.003}
Tangential distortion {tx, ty}:	{0.000105 ± 0.000009; 0.00031 ± 0.00002}

Extrinsic Parameters camera_pos_1:	
Rotation vector {x; y; z}:	{2.93498 ± 0.00017; 0.00123 ± 0.00011; 0.4117 ± 0.0003}
Translation vector: {x; y; z}:	{-47.53 ± 0.14; 56.71 ± 0.08; 925.07 ± 0.16}

Intrinsic Parameters camera_pos_2:	
Focal length {x; y}:	{5095.8 ± 0.7; 5094.9 ± 0.8}
Principal point {x; y}:	{1230.9 ± 0.9; 1035.5 ± 0.5}
Radial distortion {r2; r4}:	{-0.2086 ± 0.0003; 0.257 ± 0.005}
Tangential distortion {tx, ty}:	{-9e-005 ± 1e-005; 0.00069 ± 0.00003}

Extrinsic Parameters camera_pos_2:	
Rotation vector {x; y; z}:	{2.91634 ± 0.00018; 0.09018 ± 0.00011; -0.5696 ± 0.0003}
Translation vector: {x; y; z}:	{-47.35 ± 0.16; 57.48 ± 0.08; 940.05 ± 0.16}

Appendix E. Spare wheel well results

E.1. TOPSIS methodology

TOPSIS analysis requires a normalised decision matrix to be constructed for the current problem. Assume there are n optional spare wheel well designs and three criteria to compare the options: strain energy (performance), weight and cost. The un-normalised decision matrix can be written as:

	<i>Strain Energy</i>	<i>Weight</i>	<i>Cost</i>	
<i>Option 1</i>	$U1$	$M1$	$C1$	
<i>Option 2</i>	$U2$	$M2$	$C2$	
\vdots	\vdots	\vdots	\vdots	
<i>Option n</i>	Un	Mn	Cn	Equation E-1

The normalised data are calculated as:

$$u_i = w_u \times (U_i / \sum_{i=1}^n U_i^2) \quad \text{Equation E-2}$$

$$m_i = w_m \times (M_i / \sum_{i=1}^n M_i^2) \quad \text{Equation E-3}$$

$$c_i = w_c \times (C_i / \sum_{i=1}^n C_i^2) \quad \text{Equation E-4}$$

where w_u , w_m and w_c are associated weights of performance, weight and cost.

Two artificial solutions are hypothesised: the ideal solution contains the best attributes for all three criteria, and the negative solution contains the worst attributes, i.e.

$$A^* = \{u^*, m^*, c^*\} = \{\min(u_i), \min(m_i), \min(c_i) \text{ for } i = 1, 2, \dots, n\} \quad \text{Equation E-5}$$

for the ideal solution, and

$$A' = \{u', m', c'\} = \{\max(u_i), \max(m_i), \max(c_i) \text{ for } i = 1, 2, \dots, n\} \quad \text{Equation E-6}$$

for the negative ideal solution.

TOPSIS searches for the option which is the closest to the ideal solution and farthest from the negative ideal solution. For each option i , the separation from the ideal solution is:

$$S_i^* = \sqrt{(u_i - u^*)^2 + (m_i - m^*)^2 + (c_i - c^*)^2} \quad \text{Equation E-7}$$

and the separation from the negative ideal solution is:

$$S_i' = \sqrt{(u_i - u')^2 + (m_i - m')^2 + (c_i - c')^2} \quad \text{Equation E-8}$$

The final score indicates the relative closeness to the ideal solution A^* , which can be calculated as:

$$C_i^* = S_i' / (S_i^* + S_i') \quad \text{Equation E-9}$$

and the best option is the one whose C_i^* is the closest to 1.

E.2. Material database

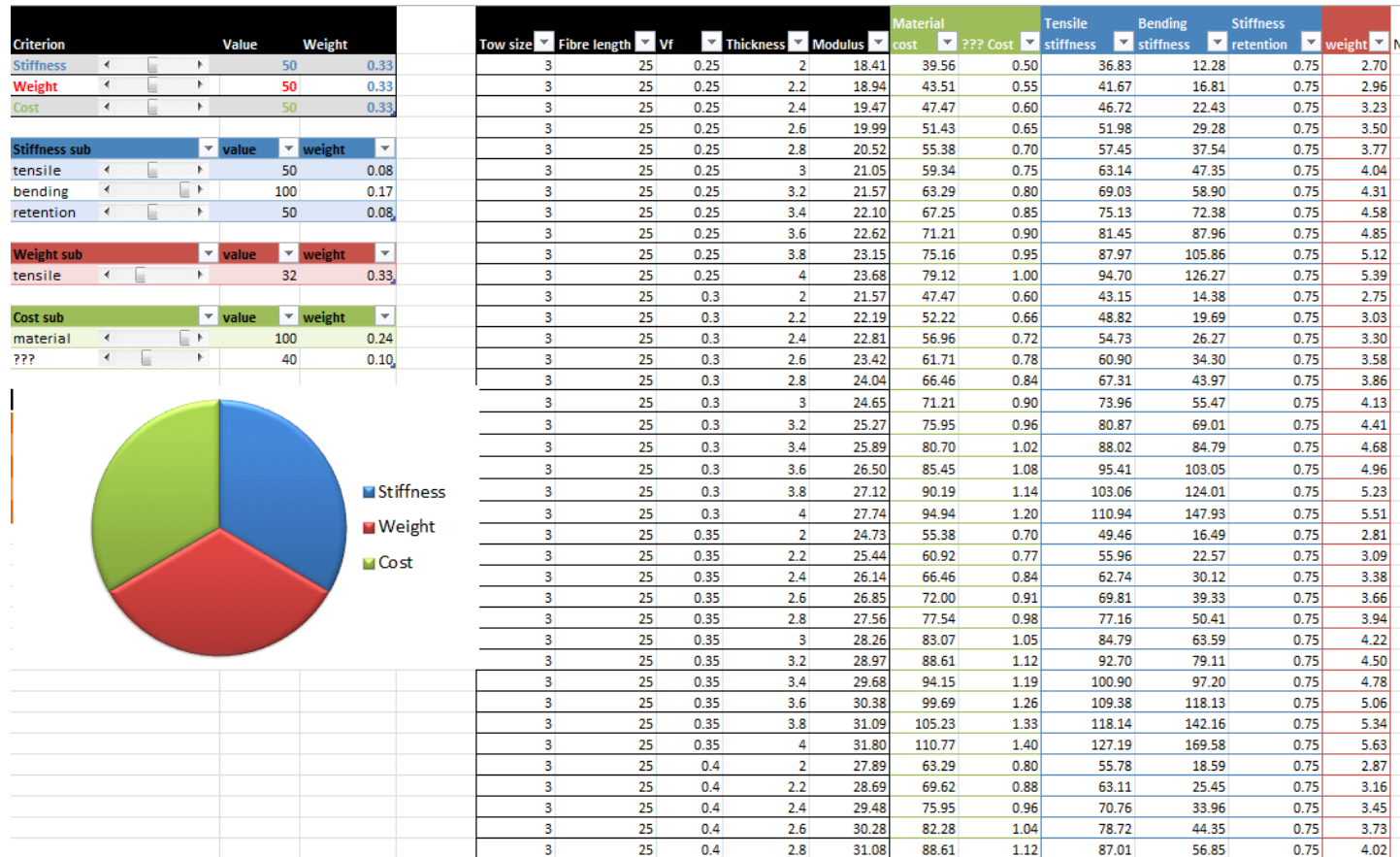


Figure E-1: Material selection model for spare wheel well model.

References

1. Yancey, R. *Aerospace vs. Automotive – Perspectives on Composites Usage and Requirements*. in *Transportation Weight Loss Diet Conference 2013*. 2013. New Messe Stuttgart, Germany.
2. Harper, L.T., *Discontinuous carbon fibre composites for automotive applications*, in *PhD Thesis 2006*, The University of Nottingham: Nottingham.
3. Brooks, R., K. Anthony, and Z. Carl, *Composites in Automotive Applications: Design*, in *Comprehensive Composite Materials 2000*, Pergamon: Oxford. p. 341-363.
4. Bishop, G., S. Halliwell, and A. Mafeld, *The UK Carbon Fibre Composites Industry: Final Public Report*, 2009.
5. Davis, B.A., *Compression Molding 2003*: Hanser Publishers.
6. Bruderick, M. *Applications of Carbon Fiber SMC for the Dodge Viper*.
7. Driver, C. *The Best of Both Worlds: Mercedes-Benz SLR McLaren Production in Woking*. 2004 20 May, 2004.
8. NetComposites, *McLaren Mercedes Benefits from Menzolit's Advanced CF-SMC*. 2005.
9. *Corvette sports a carbon composite bonnet*. Reinforced Plastics, 2003. **47**(7): p. 4.
10. Austin, M. *The Next Frontier in Carbon Fiber: Forged Composite*. 2011.
11. *Boeing 787 features composite window frames*. Reinforced Plastics, March 2007. **51**(3): p. 4.
12. Luchoo, R., et al., *Net shape spray deposition for compression moulding of discontinuous fibre composites for high performance applications* Plastics, Rubber and Composites, 2010. **39**: p. 216-231.
13. Croizat, H. and B. Boursier. *New possibilities with HexMC, a high performance molding compound*. in *Sixth International Seminar on Experimental Techniques and Design in Composite Materials*. 2003. Vicenza, Italy.
14. Turner, T.A., et al., *Energy Absorption Performance of Meso-Scale Discontinuous Carbon Fibre Composites*. International Journal of Vehicle Structures and Systems - Special Issue on Structural Impact & Crashworthiness, 2011. **3**(2).
15. Muralikannan, R. and R. Velmurugan, *Energy absorption characteristics of annealed steel tubes of various cross sections in static and dynamic loading*. Latin American Journal of Solids and Structures, 2010. **6**(4): p. 385-412.
16. Bouchet, J., E. Jacquelin, and P. Hamelin, *Static and dynamic behavior of combined composite aluminium tube for automotive*

- applications*. Composites Science and Technology, 2000. **60**(10): p. 1891-1900.
17. Warrior, N.A., et al. *Affordable Lightweight Body Structures (ALBOS)*. in *JSAE Annual Congress*. 2004. Pacifico, Yokohama.
 18. Harper, L.T., et al., *Fiber Alignment in Directed Carbon Fiber Preforms - A Feasibility Study*. Journal of Composite Materials, 2009. **43**(57): p. 57-74.
 19. Chavka, N.G., J.S. Dahl, and E.D. Kleven. *F3P fiber preforming for the Aston Martin Vanquish*. in *SAMPE Europe International Conference*. 2001. Paris.
 20. Chavka, N.G. and J.S. Dahl. *P4: Glass fiber preforming technology for automotive applications*. in *44th International SAMPE Symposium*. 1999. Long Beach, CA.
 21. Wakeman, M.D., G. Francois, and J.-A.E. Manson. *Cost Modeling of Thermoplastic P4 Process Technology*. in *Progress Report1 for the Automotive Composites Consortium*. 2006. Ecole Polytechnique Fédérale de Lausanne.
 22. Black, S., *High-Volume Preforming for Automotive Application*, in *Composites Technology*2008.
 23. Harper, L.T., et al. *Automated preform manufacture for affordable lightweight body structures*. in *26th International SAMPE Europe Conference*. 2005. Paris.
 24. Turner, T.A., et al., *Low cost carbon-fibre based automotive body panel systems - a performance and manufacturing cost comparison*. Journal of Automobile Engineering - Proceedings of the Institution of Mechanical Engineers Part D, 2008. **222**(1): p. 53-64.
 25. Patel, C., T.A. Turner, and N.A. Warrior, *Advances in Discontinuous Composites*, in *SAMPE Europe 32nd International Technical Conference & Forum*2011: Paris.
 26. Harper, L.T., et al. *Coverage and mechanical properties of spray-processed random carbon fibre composites*. in *ICCM 15*. 2005. Durban, South Africa.
 27. Liakus, J., et al., *Processing-microstructure-property predictions for short fiber reinforced composite structures based on a spray deposition process*. Composite Structures, 2003. **61**(4): p. 363-374.
 28. Chen, H.C., et al., *Development of automated chopper gun trajectory planning for spray forming*. Industrial Robot, 2004. **31**(3): p. 297-307.
 29. Wisnom, M.R., *Size effects in the testing of fibre-composite materials*. Composites Science and Technology, 1999. **59**: p. 1937-1957.
 30. Peng, B. and H.D. Espinosa. *Fracture size effect in ultrananocrystalline diamond - weibull theory applicability*. in 2004

- ASME International Mechanical Engineering Congress. 2004. California.
31. Bullock, R.E., *Strength ratios of composite materials in flexure and in tension*. 1974: p. 200-205.
 32. Hwang, T.-K., C.-S. Hong, and C.-C. Kim, *Size effect on the fiber strength of composite pressure vessels*. *Composite Structures*, 2003. **59**: p. 489-498.
 33. Holmberg, J.A., *Application of Weibull Theory to random-fibre composites*. *Composites Science and Technology*, 1995. **54**: p. 75-85.
 34. Marissen, R. and J. Linsen, *Variability of the flexural strength of sheet moulding compounds*. *Composites Science and Technology*, 1999. **59**: p. 2093-2100.
 35. Lindhagen, J.E. and L.A. Berglund, *Notch sensitivity and damage mechanisms of glass mat reinforced polypropylene*. *Polymer Composites*, 1997. **18**(1): p. 40-47.
 36. Lindhagen, J.E. and L.A. Berglund, *Application of bridging-law concepts to short-fibre composites. Part 2: Notch sensitivity*. *Composites Science and Technology*, 2000. **60**: p. 885-893.
 37. Lindhagen, J.E., N. Jekabsons, and L.A. Berglund, *Application of bridging-law concepts to short-fibre composites. Part 4: FEM analysis of notched tensile specimens*. *Composites Science and Technology*, 2000. **60**: p. 2895-2901.
 38. Shibata, S., Y. Cao, and I. Fukumoto, *Flexural modulus of the unidirectional and random composites made from biodegradable resin and bamboo and kenaf fibres*. *Composites Part A: Applied Science and Manufacturing*, 2008. **39**(4): p. 640-646.
 39. Asgari, M. and M. Masoomi, *Tensile and flexural properties of polypropylene/short poly(ethylene terephthalate) fibre composites compatibilized with glycidyl methacrylate and maleic anhydride*. *Journal of Thermoplastic Composite Materials*, 2013.
 40. Wang, S.S. and E.S.-M. Chim, *Fatigue Damage and Degradation in Random Short-Fiber SMC Composite*. *Journal of Composite Materials*, 1983. **17**(2): p. 114-134.
 41. Caprino, G., A. D'Amore, and F. Facciolo, *Fatigue Sensitivity of Random Glass Fibre Reinforced Plastics*. *Journal of Composite Materials*, 1998. **32**(12): p. 1203-1220.
 42. Boisse, P., B. Zouari, and A. Gasser, *A mesoscopic approach for the simulation of woven fibre composite forming*. *Composites Science and Technology*, 2005. **65**(3-4): p. 429-436.
 43. Ladevèze, P. *Validation de modèle et théorie des méconnaissances*. in *Institut FARMAN Séminaire "Incertitudes"*. 2009.
 44. *CFK-Spezialist mit Luftfahrt-Knowhow*, in *Industrieanzeiger* 2013. p. 39.

45. Svanberg, K., *The method of moving asymptotes—a new method for structural optimization*. International Journal for Numerical Methods in Engineering, 1987. **24**(2): p. 359-373.
46. Venkayya, V.B., *Optimality criteria: A basis for multidisciplinary design optimization*. Computational Mechanics, 1989. **5**(1): p. 1-21.
47. Jakiela, M.J., et al., *Continuum structural topology design with genetic algorithms*. Computer Methods in Applied Mechanics and Engineering, 2000. **186**(2-4): p. 339-356.
48. Lam, Y.C., D. Manickarajah, and A. Bertolini, *Performance characteristics of resizing algorithms for thickness optimization of plate structures*. Finite Elements in Analysis and Design, 2000. **34**(2): p. 159-174.
49. Gitman, I.M., H. Askes, and L.J. Sluys, *Representative volume: Existence and size determination*. Engineering Fracture Mechanics, 2007. **74**(16): p. 2518-2534.
50. Kirupanantham, G., *Characterisation of discontinuous carbon fibre preforms for automotive applications in Mechanical Engineering*2013, University of Nottingham.
51. Bond, M., *Multi-scale modelling of discontinuous carbon fibre reinforced composites*, in *Mechanical Engineering*2012, University of Nottingham.
52. Li, S., *General unit cells for micromechanical analyses of unidirectional composites*. Composites: Part A, 2000. **32**: p. 815-826.
53. LI, S., *Boundary conditions for unit cells from periodic microstructures and their implications*. Composites Science Technology, 2008. **68**: p. 1962-1974.
54. Wongsto, A. and S. Li, *Micromechanical FE analysis of UD fibre-reinforced composites with fibres distributed at random over the transverse cross-section*. Composites Part A: Applied Science and Manufacturing, 2005. **36**(9): p. 1246-1266.
55. Trias, D., et al., *Determination of the critical size of a statistical representative volume element (SRVE) for carbon reinforced polymers*. Acta Materialia, 2006. **54**(13): p. 3471-3484.
56. Pan, Y., L. Iorga, and A.A. Pelegri, *Numerical generation of a random chopped fiber composite RVE and its elastic properties*. Composites Science and Technology, 2008. **68**(13): p. 2792-2798.
57. Harper, L.T., et al., *Characterisation of random carbon fibre composites from a directed fibre preforming process: Analysis of microstructural parameters*. Composites Part A: Applied Science and Manufacturing, 2006. **37**(11): p. 2136-2147.
58. Eshelby, J.D., *The determination of the elastic field of an ellipsoidal inclusion, and related problems*. Proceedings of the Royal Society of London, 1957. **A241**: p. 376-396.

59. Mori, T. and K. Tanaka, *Average stress in matrix and elastic energy of materials with misfitting inclusions*. Acta Metallurgica, 1973. **21**: p. 571-574.
60. Christensen, R.M. and F.M. Waals, *Effective stiffness of randomly oriented fibre composites*. Journal of Composite Materials, 1972. **6**: p. 518-532.
61. Cox, H.L., *The elasticity and strength of paper and other fibrous materials*. British Journal of Applied Physics, 1952. **3**: p. 72-79.
62. Advani, S.G. and C.L. Tucker III, *The use of tensors to describe and predict fiber orientation in short fiber composites*. Journal of Rheology, 1987. **31**(8): p. 751-784.
63. Halpin, J.C. and N.J. Pagano, *The laminate approximation for randomly oriented fibre composites*. Journal of Composite Materials, 1969. **3**: p. 720-724.
64. Halpin, J.C., K. Jerine, and J.M. Whitney, *The laminate analogy for 2 and 3 dimensional composite materials*. Journal of Composite Materials, 1971. **5**: p. 36.
65. Ionita, A. and Y.J. Weitsman, *On the mechanical response of randomly oriented reinforced chopped fibre composites: Data and model*. Composites Science and Technology, 2006. **66**(14): p. 2566-2579.
66. Böhm, H.J., A. Eckschlager, and W. Han, *Multi-inclusion unit cell models for metal matrix composites with randomly oriented discontinuous reinforcements*. Computational Materials Science, 2002. **25**(1-2): p. 42-53.
67. Mishnaevsky, L.L., *Three-dimensional numerical testing of microstructures of particle reinforced composites*. Acta Materialia, 2004. **52**(14): p. 4177-4188.
68. Kari, S., H. Berger, and U. Gabbert, *Numerical evaluation of effective material properties of randomly distributed short cylindrical fibre composites*. Computational Materials Science, 2007. **39**(1): p. 198-204.
69. Duschlbauer, D., H.J. Bohm, and H.E. Pettermann, *Computational Simulation of Composites Reinforced by Planar Random Fibers: Homogenization and Localization by Unit Cell and Mean Field Approaches*. Journal of Composite Materials, 2006. **40**(24): p. 2217-2234.
70. Gusev, A.A., *Representative volume element size for elastic composites: A numerical study*. Journal of the Mechanics and Physics of Solids, 1997. **45**(9): p. 1449-1459.
71. Eason, T. and O. Ochoa, *Modeling residual stresses and damage initiation in discontinuous random fiber SRIM composites*. Computer Aided Design in Composite Material Technology, 1996. **5**: p. 123-132.

72. Eason, T. and O. Ochoa, *Material behaviour of Structural Reaction Injection Molded composites under thermomechanical loading*. Journal of Composite Materials, 2000. **34**(5): p. 411-432.
73. Kari, S., *Micromechanical Modelling and Numerical Homogenization of Fibre and Particle Reinforced Composites*, in *Institute of Mechanics Department 2005*, Otto-von-Guericke University Magdeburg: Magdeburg.
74. Evans, K.E. and A.G. Gibson, *Prediction of the maximum packing fraction achievable in randomly*. Composites Science and Technology, 1986. **25**: p. 149-162.
75. Pan, Y., L. Iorga, and A.A. Pelegri, *Analysis of 3D random chopped fiber reinforced composites using FEM and random sequential adsorption*. Computational Materials Science, 2008. **43**(3): p. 450-461.
76. Iorga, L., Y. Pan, and A.A. Pelegri, *Numerical characterisation of material elastic properties for random fiber composites*. Journal of Mechanics of Materials and Structures, 2008. **3**(7): p. 1279-1298.
77. Pan, N., *Analytical characterization of the anisotropy and local heterogeneity of short fiber composites: Fiber fraction as a variable*. Journal of Composite Materials, 1994. **28**(16): p. 1500-1531.
78. Gusev, A., et al., *Orientation Averaging for Stiffness and Thermal Expansion of Short Fiber Composites*. Advanced Engineering Materials, 2002. **4**(12): p. 931-933.
79. Nakamura, S. and R.S. Lakes, *Finite element analysis of Saint-Venant end effects in micropolar elastic solids*. Engineering Computations, 1995. **12**(6): p. 571-587.
80. Trias, D., et al., *Random models versus periodic models for fibre reinforced composites*. Computational Materials Science, 2006. **38**(2): p. 316-324.
81. Bohm, H.J., *A short introduction to basic aspects of continuum micromechanics*, 2006.
82. Monaghan, J. and D. Brazil, *Modeling the sub-surface damage associated with the machining of a particle reinforced MMC*. Computational Materials Science, 1997. **9**(1-2): p. 99-107.
83. Haoran, C., Y. Quangsang, and F.W. Williams, *A self-consistent finite element approach to the inclusion problem*. Computational Materials Science, 1994. **2**(2): p. 301-307.
84. Sautter, M., et al., *Finite element modelling of a transverse-loaded fibre composite effects of section size and net density*. Computational Materials Science, 1993. **1**(3): p. 225-233.
85. Hill, R., *Elastic properties of reinforced solids: some theoretical principles*. Journal of the Mechanics and Physics of Solids, 1963. **11**: p. 357.

86. Hashin, Z., *Analysis of composite materials - a survey*. Journal of Applied Mechanics, 1983. **50**: p. 481-505.
87. Drugan, W. and J. Willis, *A micromechanical-based non local constitutive equation and estimates of representative volume element size for elastic composites*. Journal of Mechanics Physics and Solids, 1996. **44**(4): p. 497-524.
88. Terada, K., et al., *Simulation of the multi-scale convergence in computational homogenization approaches*. International Journal of Solids and Structures, 2000. **37**(16): p. 2285-2311.
89. Ostoja-Starzewski, M., P.Y. Sheng, and I. Jasiuk, *Damage patterns and constitutive response of random matrix-inclusion composites*. Engineering Fracture Mechanics. **58**(5-6): p. 581-606.
90. Houdaigui, F.E., et al. *On the size of the representative volume element for isotropic elastic polycrystalline copper*. in *IUTAM Symposium on Mechanical Behavior and Micro-Mechanics of Nanostructured Materials*. 2005. Beijing, China: Springer.
91. Weibull, W., *A statistical theory of strength of materials*. Ingeniorsvetenskapsakademien Handlingar, 1939. **151**: p. 1-29.
92. Pelissou, C., et al., *Determination of the size of the representative volume element for random quasi-brittle composites*. International Journal of Solids and Structures, 2009. **46**(14-15): p. 2842-2855.
93. Kanit, T., et al., *Determination of the size of the representative volume element for random composites: statistical and numerical approach*. International Journal of Solids and Structures, 2003. **40**: p. 3647-3679.
94. Rondeau, R., S.R. Reeve, and G. Bond. *The effect of tows and filament groups on the properties of discontinuous fiber composites*. in *44th International SAMPE Symposium & Exhibition*. 1999. Long Beach, CA, USA.
95. Feraboli, P., et al., *Modulus measurement for prepreg-based discontinuous carbon fibre/epoxy systems*. Journal of Composite Materials, 2009. **43**(19): p. 1947-1965.
96. Feraboli, P., et al., *Defect and damage analysis of advanced discontinuous carbon/epoxy composite materials*. Composites Part A: Applied Science and Manufacturing, 2010. **41**(7): p. 888-901.
97. Sproull, B. and W.M. Newman, *Principles of Interactive Computer Graphics*. International Edition ed1973: McGraw-Hill.
98. Kaw, A.K., *Macromechanical Analysis of a Lamina*, in *Mechanics of Composite Materials, Second Edition*2005, CRC Press: London. p. 61-202.
99. Gohorianu, G., et al. *Composite bolted joints behaviour: Effects of hole machining defects*. in *Joining Plastics*. 2006. National Physics Laboratory, London.

100. Lu, B.L. and S. Torquato, *LOCAL VOLUME FRACTION FLUCTUATIONS IN HETEROGENEOUS MEDIA*. Journal of Chemical Physics, 1990. **93**(5): p. 3452-3459.
101. Hitchen, S.A., et al., *The effect of fibre length on fracture toughness and notched strength of short carbon fibre/epoxy composites*. Composites, 1994. **25**(6).
102. Mallick, P.K., *Effects of hole stress concentration and its mitigation on the tensile strength of sheet moulding compound (SMC-R50) composites*. Composites, 1988. **19**(4): p. 283-287.
103. Agarwal, B.D. and G.S. Giare, *Crack growth resistance of short fibre composites: 1 - Influence of fibre concentration, specimen thickness and width*. Fibre Science and Technology, 1981. **15**: p. 283-298.
104. Toll, S. and C.-G. Aronsson, *Notched Strength of Long- and Short-Fibre Reinforced Polyamide*. Composites Science and Technology, 1992. **45**: p. 43-54.
105. Feraboli, P., et al., *Notched behavior of prepreg-based discontinuous carbon fiber/epoxy systems*. Composites Part A: Applied Science and Manufacturing, 2009. **40**(3): p. 289-299.
106. Kim, J.K., D.S. Kim, and N. Takeda, *Notched Strength and Fracture Criterion in Fabric Composite Plates Containing a Circular Hole*. Journal of Composite Materials, 1995. **29**: p. 982-998.
107. Sabeel Ahmed, K., S. Vijayarangan, and A.C.B. Naidu, *Elastic properties, notched strength and fracture criterion in untreated woven jute-glass fabric reinforced polyester hybrid composites*. Materials and Design, 2007. **28**: p. 2287-2294.
108. Whitney, J.M. and R.J. Nuismer, *Stress fracture criteria for laminated composites containing stress concentrations*. Journal of Composite Materials, 1974. **8**: p. 253-265.
109. Konish Jr, H.J. and J.M. Whitney, *Approximate stress in an orthotropic plate containing a circular hole*. Journal of Composite Materials, 1975. **9**: p. 157-166.
110. Tan, S.C., *Finite-Width Correction Factors for Anisotropic Plate Containing a Central Opening* Journal of Composite Materials, 1988. **22**(11): p. 1080-1097.
111. Pipes, R.B., R.C. Wetherhold, and J.W. Gillespie Jr., *NOTCHED STRENGTH OF COMPOSITE MATERIALS*. Journal of Composite Materials, 1979. **13**(2): p. 148-160.
112. Pipes, R.B., R.C. Wetherhold, and J.W. Gillespie Jr., *MACROSCOPIC FRACTURE OF FIBROUS COMPOSITES*. Materials Science and Engineering, 1980. **45**(3): p. 247-253.
113. Rao, A.S., Y. Krishna, and B.N. Rao, *Comparison of fracture models to assess the notched strength of composite/solid propellant tensile specimens*. Materials Science and Engineering A, 2004. **385**(1-2): p. 429-439.

114. Potti, P.K.G., B.N. Rao, and V.K. Srivastava, *Tensile fracture strength of boron/aluminum laminates with holes and slits*. Materials Science and Engineering A, 2001. **301**(2): p. 244-252.
115. de Azevedo Soriano, E. and S.F.M.d. Almeida, *Notch sensitivity of carbon/epoxy fabric laminates*. Composites Science and Technology, 1999. **59**(8): p. 1143-1151.
116. Govindan, P.K., B.N. Rao, and V.K. Srivastava, *Notched tensile strength for and long- and short-fibre reinforced polyamide*. Theoretical and Applied Fracture Mechanics, 2000. **33**: p. 145-152.
117. Piggott, M.R., *Mesostructures and their mechanics in fibre composites*. Advanced Composite Materials, 1996. **6**: p. 75-81.
118. Yang, R.J. and C.H. Chuang, *Optimal topology design using linear programming*. Computers & Structures, 1994. **52**(2): p. 265-275.
119. Feury, C. and M. Geradin, *Optimality criteria and mathematical programming in structural weight optimization*. Computers & Structures, 1978. **8**(1): p. 7-17.
120. Hwang, C.-L., Y.-J. Lai, and T.-Y. Liu, *A new approach for multiple objective decision making*. Computers & Operations Research, 1993. **20**(8): p. 889-899.
121. Harper, L.T., et al., *Representative volume elements for discontinuous carbon fibre composites – Part 1: Boundary conditions*. Composites Science and Technology, 2012. **72**(2): p. 225-234.
122. Harper, L.T., et al., *Representative volume elements for discontinuous carbon fibre composites – Part 2: Determining the critical size*. Composites Science and Technology, 2012. **72**(2): p. 204-210.
123. Patnaik, S.N., J.D. Guptill, and L. Berke, *Merits and limitations of optimality criteria method for structural optimization*. International Journal for Numerical Methods in Engineering, 1995. **38**(18): p. 3087-3120.
124. Otsu, N., *A Threshold Selection Method from Gray-Level Histograms*. Systems, Man and Cybernetics, IEEE Transactions on, 1979. **9**(1): p. 62-66.
125. Liao, P.-S., T.-S. Chen, and P.-C. Chung, *A Fast Algorithm for Multilevel Thresholding*. Journal of Information Science and Engineering, 2001. **17**: p. 713-727.
126. Huang, D.-Y. and C.-H. Wang, *Optimal multi-level thresholding using a two-stage Otsu optimization approach*. Pattern Recognition Letters, 2009. **30**(3): p. 275-284.
127. Figueira, J., S. Greco, and M. Ehrgott, *Multiple criteria decision analysis: state of the art surveys*. Vol. 78. 2005: Springer.
128. Fishburn, P.C., *Letter to the Editor—Additive Utilities with Incomplete Product Sets: Application to Priorities and Assignments*. Operations Research, 1967. **15**(3): p. 537-542.

129. Miller, D.W. and M.K. Starr, *Executive decisions and operations research* 1969: Prentice-Hall.
130. Yoon, K., *A reconciliation among discrete compromise solutions*. Journal of the Operational Research Society, 1987: p. 277-286.
131. Hwang, C.-L., Y.-J. Lai, and T.-Y. Liu, *A new approach for multiple objective decision making*. Computers & operations research, 1993. **20**(8): p. 889-899.
132. *Easy Composites Woven Glass* 2013; Available from: <http://www.easycomposites.co.uk/products/woven-glass-fabric/woven-glass-fabric-22-twill-300g.aspx>.
133. *Easy Composites Woven Carbon*. 2013; Available from: <http://www.easycomposites.co.uk/products/carbon-fibre-cloth-fabric/heavyweight-carbon-fibre-cloth-22-twill-650gsm-12k-1m.aspx>.
134. Zou, Z. and S. Li, *Stresses in an infinite medium with two similar circular cylindrical inclusions*. Acta Mechanica, 2002. **156**: p. 93-108.
135. Harper, L.T., et al., *Characterisation of random carbon fibre composites from a directed fibre preforming process: The effect of tow filamentisation* Composites Part A: Applied Science and Manufacturing, 2007. **38**(3): p. 755-770